POLITECNICO DI MILANO

Scuola di Ingegneria dei Processi Industriali

Corso di Laurea Specialistica in Ingegneria dei Materiali

METHODS FOR SATURATION ASSESSMENT IN THE LHC NEG-COATED BEAM PIPES

Tesi di Laurea Specialistica di:

Tommaso PORCELLI

matricola n. 751936

Relatore: Prof. Marco BEGHI

Correlatore: Dott. Giuseppe BREGLIOZZI

Anno accademico 2011/2012

"Illud in his quoque te rebus cognoscere avemus,

corpora cum deorsum rectum per inane feruntur

ponderibus propriis, incerto tempore ferme

incertisque locis spatio depellere paulum,

tantum quod momen mutatum dicere possis.

Quod nisi declinare solerent, omnia deorsum

imbris uti guttae caderent per inane profundum

nec foret offensus natus nec plaga creata

principiis; ita nihil umquam natura creasset."

(Titus Lucretius Carus, "De rerum Natura", liber II, vv. 216-224)[1]

---

[1] "In these affairs we wish thee also well aware of this: the atoms, as their own weight bears them down plumb through the void, at scarce determined times, in scarce determined places, from their course decline a little – call it, so to speak, mere changed trend. For were it not their wont thuswise to swerve, down would they fall, each one, like drops of rain, through the unbottomed void; and then collisions ne'er could be nor blows among the primal elements; and thus Nature would never have created aught."
(Titus Lucretius Carus, "On the Nature of Things", book II, vv. 216-224; translation by William Ellery Leonard)

ABSTRACT

This Master's degree thesis work was carried out at the *European Organization for Nuclear Research* (CERN) in the *LHC Beam Vacuum* section of the *Vacuum, Surfaces and Coatings* group (VSC–LBV).

The aim of this research is to study the pumping properties of non-evaporable getters and their saturation behaviour. This work will focus on the saturation of these materials and useful criteria will be assessed for the evaluation and prediction of future technical interventions for vacuum systems exploiting this technology. The measurements will be compared with simulations based on Test-Particle Monte-Carlo method and on multi-gas model.

The main results of this work were also presented at the *International Particle Accelerators Conference 2012*, which took place in New Orleans in May 2012.

Non-evaporable getters (NEG) are a class of metal alloys which nowadays is employed in several technological applications requiring the maintenance of stable high or ultra-high vacuum conditions in a system.

These materials ensure the pumping of residual gases in vacuum systems thanks to the formation of stable chemical bonds between gas molecules and their metallic surface, even at room temperature. In order to ensure this adsorption mechanism, a getter should have a superficial active layer with free adsorption sites able to bind gas molecules. As the chemisorption progresses, the number of free sites decreases, until the surface becomes completely saturated and its pumping properties disappear, thus requiring to be reactivated by thermal diffusion of the surface oxide layer containing the adsorbed molecules into the bulk.

Among the several technological fields in which NEG alloys are commonly employed, one of the most exciting and recent applications of these materials concerns the research in the field of particle physics and the use of NEG on the internal surfaces of vacuum systems for synchrotrons and high-energy accelerators.

In particular, vacuum beam pipes coated with TiZrV NEG alloy are extensively used at CERN in order to keep and maintain the required ultra-high vacuum conditions (with pressures in the range of 10^{-10} *mbar*) in several vacuum sectors of the *Large Hadron Collider* (LHC), which are at room temperature during operations with proton beams.

Molecular desorption due to dynamic effects is stimulated during protons operation at high intensity. This phenomenon produces an important gas load from the vacuum chambers' walls, which could lead to a partial or total saturation of the NEG coating, thus compromising its capability of maintaining the requested vacuum conditions.

To keep the designed vacuum performances and to schedule technical interventions for NEG reactivation, it is necessary to take into account all these aspects and to regularly evaluate the saturation level of NEG coatings.

Hence, experimental studies were conducted in the framework of this thesis work in order to identify the best method to assess the saturation level of the LHC's NEG coated beam pipes.

Chapter 1 briefly describes CERN, the LHC and its vacuum sectors where NEG coatings are employed.

Chapter 2 instead gives basic notions about the principles of vacuum science and technology, whereas Chapters 3 and 4 concern, respectively, pumping systems and vacuum pressure gauges used for the purposes of this work.

Chapter 5 introduces NEG materials, focusing on their pumping characteristics and on the factors influencing their behaviour and their performances. Chapter 6 illustrates the theoretical principles of the employed simulation programs and Chapter 7 describes the experimental systems in which saturation tests were performed.

These measurements, whose results are presented and analysed in Chapter 8, were conducted in two different vacuum systems, namely a *2 m* long NEG coated vacuum chamber and a *28 m* long NEG coated pilot sector, which reproduces the configuration of the room temperature vacuum sectors in the LHC. Monte-Carlo and multi-gas simulations of the same saturation process will be also presented.

Finally, Chapter 9 reports the results of two practical applications of these evaluation techniques that were conducted directly in the room temperature vacuum sectors of the LHC and in the NEG coated beam pipes of the *Compact Muon Solenoid* (CMS), which is one of the two largest particle-physics detectors located along the perimeter of the LHC.

ABSTRACT

Questo lavoro di tesi è stato svolto al CERN di Ginevra all'interno della sezione *LHC Beam Vacuum* del gruppo *Vacuum, Surfaces and Coatings*.

Scopo di tale ricerca è lo studio delle proprietà di pompaggio dei *non-evaporable getter* (NEG) e del loro meccanismo di adsorbimento. Questo lavoro si concentrerà sulla saturazione di tali materiali e stabilirà dei criteri utili per la valutazione e la previsione di futuri interventi tecnici per sistemi a vuoto che sfruttano questa tecnologia. Le misure effettuate saranno confrontate con analoghe simulazioni basate sul metodo Monte Carlo e sul modello multi-gas.

I principali risultati di questa ricerca, inoltre, sono stati presentati all'*International Particle Accelerators Conference 2012*, che si è tenuta a New Orleans nel maggio 2012.

I *non-evaporable getter* (NEG) sono una classe di leghe metalliche che, oggigiorno, è impiegata in svariate applicazioni tecnologiche che richiedano il mantenimento di condizioni stabili di alto od ultra alto vuoto in un sistema.

Questi materiali assicurano il pompaggio dei gas residui in sistemi a vuoto grazie alla formazione di legami chimici stabili tra la loro superficie metallica e le molecole gassose, anche a temperatura ambiente. Per rendere possibile questo meccanismo di adsorbimento, un *getter* deve avere un *layer* superficiale attivo, con siti di adsorbimento liberi capaci di legare le molecole di gas. Al progredire dell'adsorbimento chimico, il numero di siti liberi diminuisce, finché la superficie non diventa completamente satura e le sue proprietà di pompaggio non scompaiono, rendendo necessaria una sua riattivazione che avviene tramite diffusione termica, all'interno del materiale, dello strato di ossido superficiale contenente le molecole adsorbite.

Tra i numerosi campi in cui le leghe NEG sono comunemente impiegate, una delle più interessanti e recenti applicazioni di questi materiali riguarda la ricerca nel campo della fisica particellare e l'utilizzo dei NEG sulle superfici interne di sistemi a vuoto per sincrotroni ed acceleratori ad alta energia.

In particolare, camere a vuoto rivestite con una lega NEG TiZrV sono ampiamente utilizzate al CERN per raggiungere e mantenere le necessarie condizioni di ultra alto vuoto (con

pressioni dell'ordine di 10^{-10} *mbar*) in svariati settori del *Large Hadron Collider* (LHC) che sono mantenuti a temperatura ambiente durante le operazioni con fasci di protoni.

Durante le operazioni con protoni ad alta energia, il desorbimento molecolare dalle superfici interne dell'acceleratore è stimolato da cosiddetti effetti dinamici. Questi fenomeni producono un carico di gas residui non trascurabile, che può portare ad una parziale o totale saturazione del rivestimento NEG, compromettendone così la capacità di mantenere i livelli di pressione richiesti.

Per assicurare le condizioni di vuoto necessarie e per programmare interventi tecnici volti alla riattivazione del NEG, è necessario prendere in considerazione questi aspetti e valutare con regolarità il livello di saturazione dei rivestimenti NEG.

Nell'ambito di questo lavoro di tesi, pertanto, sono stati svolti degli studi sperimentali in laboratorio, volti all'individuazione del metodo migliore per la valutazione del livello di saturazione dei rivestimenti NEG all'interno di LHC.

Il primo capitolo descrive brevemente il CERN, LHC ed i suoi settori in cui i rivestimenti NEG sono utilizzati.

Il secondo capitolo, invece, fornisce le nozioni fondamentali relative alla scienza e tecnologia del vuoto, mentre il terzo ed il quarto capitolo si occupano, rispettivamente, dei sistemi di pompaggio e degli strumenti di misura di pressione utilizzati per gli scopi di questa ricerca.

Il quinto capitolo presenta i materiali NEG, soffermandosi in particolare sulle loro caratteristiche di pompaggio e sui fattori che ne influenzano il comportamento e l'efficienza.

Il sesto capitolo illustra i principi teorici alla base dei programmi di simulazione utilizzati, mentre il settimo descrive i sistemi sperimentali su cui sono stati effettuati i test di saturazione.

Tali misure, i cui risultati sono presentati ed analizzati nell'ottavo capitolo, sono state compiute in due diversi sistemi a vuoto, entrambi rivestiti di NEG, cioè una camera lunga *2 m* ed un sistema di *28 m* analogo ai settori a temperatura ambiente di LHC. Saranno presentate, inoltre, alcune simulazioni Monte Carlo e multi-gas dello stesso processo di saturazione.

Il nono capitolo, infine, mostra i risultati di due applicazioni pratiche di queste tecniche di valutazione, condotte direttamente nei settori a vuoto a temperatura ambiente di LHC e nelle camere a vuoto rivestite di NEG del *Compact Muon Solenoid* (CMS), che è uno dei due maggiori esperimenti di fisica particellare posti lungo il perimetro dell'acceleratore.

TABLE OF CONTENTS

LIST OF FIGURES

LIST OF TABLES

1. CERN AND THE LHC

1.1 THE EUROPEAN LABORATORY FOR PARTICLE PHYSICS

In 1952 eleven European countries decided to found a scientific council, the *European Council for Nuclear Research* (*Conseil Européen pour la Recherche Nucléaire,* CERN); the aim was to restore European scientific research to its former pre-war glory and to unite European scientists by creating a pan-European atomic physics laboratory, allowing them to afford the increasing costs of nuclear physics facilities.

This decision fulfilled the efforts of the French physicist Louis de Broglie, who had first officially proposed the creation of a European Laboratory at the *European Cultural Conference* in Lausanne in December 1949. A further push in this direction had come at the fifth *UNESCO General Conference*, held in Florence in June 1950, where the American Nobel laureate Isidor Rabi had tabled a resolution aiming "to assist and encourage the formation of regional research laboratories in order to increase international scientific collaboration…".

The foundation of this provisional council prepared the establishment of an international laboratory, namely the *European Organization for Nuclear Research* (*Organisation Européenne pour la Recherche Nucléaire*), which officially came into being on the 29th September 1954. The provisional council was dissolved but the acronym CERN remained to indicate both the newly-constituted organisation and its research laboratory.

The laboratory operated by CERN is also commonly referred to as the *European Laboratory for Particle Physics* (*Laboratoire européen pour la physique des particules*), which better describes its research field.

In October 1952, the Suisse city of Geneva had been chosen as the site of this future laboratory, whose twelve founding members were: Belgium, Denmark, France, the Federal Republic of Germany, Greece, Italy, the Netherlands, Norway, Sweden, Switzerland, the United Kingdom and Yugoslavia. The latter left CERN in 1961, but ten other countries joined the organisation in the following years (in chronological order: Austria, Spain, Portugal, Finland, Poland, Hungary, the Czech Republic, Slovakia and Bulgaria), leading to the current total of twenty member states.

Nowadays there are also two candidates for accession (Romania and Serbia), one associate member (Israel) and some observers (India, Japan, Russia, Turkey, the United States, the European Communities and UNESCO).

Figure 1 – Third session of the provisional CERN council in Amsterdam on the 4th October 1952. At this session, Geneva was chosen as the site for the future laboratory (courtesy CERN).

The first CERN's accelerator, built in 1957, was the *600 MeV* Synchrocyclotron (SC), providing beams for the first particle and nuclear physics experiments. In the following years, several accelerators were built, progressively leading to the creation of a unique structure of interlinked machines that provided a large range of particle beams.

The researches conducted at CERN over the last six decades lead to an incredible number of discoveries, radically transforming our knowledge in the field of particle physics and determining a huge number of fundamental technological advances.

Among the others, it is worth to mention the Nobel Prize in physics to Carlo Rubbia and Simon Van der Meer in 1984 and the invention of the World Wide Web by Tim Berners-Lee in 1989.

1.2 THE LARGE HADRON COLLIDER

The *Large Hadron Collider* (LHC) is today the world's largest particle accelerator; it is operated by CERN and it is located in a tunnel at about *100 m* underground beneath the border between Switzerland and France, in Geneva area.

This tunnel formerly housed the Large Electron-Positron Collider (LEP), which ran from 1989 to 2000 and was then dismantled and replaced by the LHC.

The LHC, with a diameter of *26.66 km*, is the latest CERN's accelerator and one of the most complex machines ever built. It will allow to revolutionise our understanding of the universe and of its fundamental laws.

The Large Hadron Collider Project was approved by CERN Council in December 1994. The LHC started operation in September 2008 and gradually increased beam energies in the following months. It will be able to accelerate particles at the highest scheduled energy in 2014, after a long technical shutdown that will start at the end of 2012.

Table 1 summarises some of the most relevant LHC's beam parameters.

Table 1 – List of relevant LHC beam parameters. Peak luminosity is considered in IP1 and IP5, i.e. the intersection points of the two beam lines in correspondence of ATLAS and CMS, respectively [1].

	Injection	Collision
Proton energy [GeV]	450	7000
Number of particles per bunch	$1.15 \cdot 10^{11}$	
Number of bunches	2808	
Bunch spacing [ns]	25	
Circulating beam current [A]	0.584	
Stored energy per beam [MJ]	23.3	362
Peak luminosity [cm^{-2}·s^{-1}]	–	$1.0 \cdot 10^{34}$

At full power, the LHC will be able to accelerate two hadron (either protons or lead ions) beams travelling in opposite directions into two parallel beam pipes up to a maximum energy of *7 TeV* per each beam, corresponding to *14 TeV* in the centre-of-mass. By colliding the two beams at these very high energies, physicists recreate the conditions just after the Big Bang and analyse the particles created in the collisions thanks to a number of detectors located along the LHC's perimeter in correspondence of the intersection points of the two beam

pipes. The four main detectors are ATLAS (*A Toroidal LHC ApparatuS*), CMS (*Compact Muon Solenoid*), ALICE (*A Large Ion Collider Experiment*) and LHCb (*Large Hadron Collider beauty*). They are located in four huge underground caverns along the LHC's ring. Two other much smaller detectors, TOTEM (*TOTal Elastic and diffractive cross section Measurement*) and LHCf (*Large Hadron Collider forward*), are positioned near the CMS and ATLAS detectors, respectively.
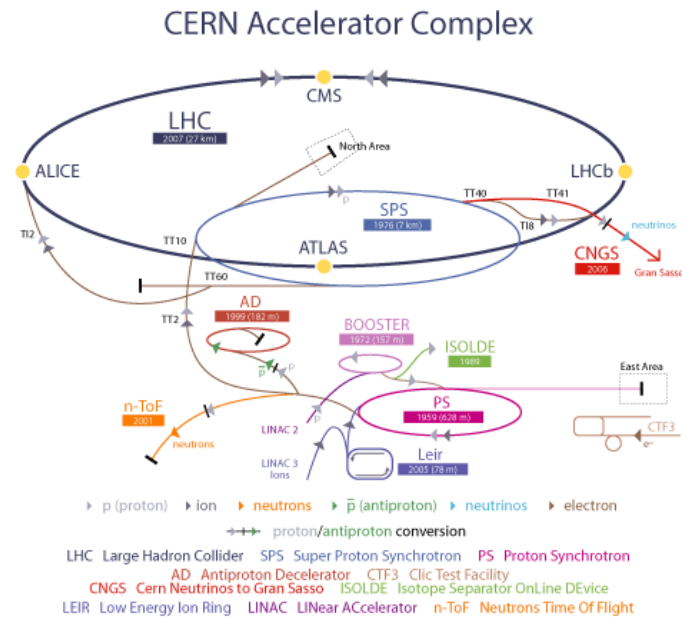
Figure 2 – CERN accelerator complex (courtesy CERN).

The LHC is the latest ring of the accelerator complex that has been built at CERN through the years (Figure 2). This complex is a succession of particle accelerators that can reach increasingly higher energies.

Protons are obtained by removing electrons from hydrogen atoms. The linear accelerator LINAC 2 generates *50 MeV* protons and feeds the *Proton Synchrotron Booster* (PSB), accelerating to *1.4 GeV*. The PSB feeds in turn the *Proton Synchrotron* (PS), which boosts the energy up to *26 GeV* before transferring the beam to the *Super Proton Synchrotron* (SPS), which accelerates it to *450 GeV* and finally transfers it to the LHC.

Lead ions for the LHC instead start form a source of vaporised lead and enter LINAC 3 before being collected and accelerated in the Low Energy Ion Ring (LEIR). They then follow the same route to maximum acceleration as protons.

The two beams are guided around the accelerator ring by a strong magnetic field (about *8 T*), achieved using superconducting electromagnets. These are built from coils of special NbTi cables that operate in a superconducting state, efficiently conducting electricity without

4

resistance or loss of energy. This requires cooling down the magnets to a maximum temperature of *1.9 K* by immersing the superconducting magnets in a pressurised bath of superfluid helium at about *0.13 MPa*. For this reason, the accelerator is connected to a distribution system of liquid helium.

Thousands of magnets of different varieties and sizes are used to direct the beams around the accelerator: these include 1232 dipole magnets of *15 m* length which are used to bend the beams and 392 quadrupole magnets, each *5-7 m* long, to focus the beams.

Once they have been accelerated to *7 TeV*, the two particle beams travel inside the LHC with a speed almost equal to light speed, giving thousands of collisions that progressively degrade the beam luminosity *L*, which is measured in *[cm⁻²·s⁻¹]* and is defined as the ratio between the number of events per second N_{event} generated in the LHC collisions and the cross-section σ_{event} for the event under study:

$$L = \frac{N_{event}}{\sigma_{event}}$$

In the LHC, a maximum peak luminosity of *10³⁴ cm⁻²·s⁻¹* is reached for proton beams in correspondence of the two high-luminosity experiments, namely ATLAS and CMS. Loss of luminosity can be caused by diffusion of the beam via beam-beam and beam-gas interactions. Appropriate vacuum conditions must thus be kept and maintained inside the beam pipes during operations, in order to avoid a reduction of the beam lifetime and luminosity and an increase of the background noise in the LHC's experiments.

Table 2 – Nuclear scattering cross-sections at *7 TeV* for different gases and the corresponding gas densities and equivalent pressures at *5 K* for a *100 h* lifetime [1].

Gas	Nuclear scattering cross section [cm²]	Gas density [m⁻³] for *100 h* lifetime	Pressure [mbar] at *5 K*, for *100 h* lifetime
H_2	$9.5 \cdot 10^{-26}$	$9.81 \cdot 10^{14}$	$6.71 \cdot 10^{-10}$
He	$1.26 \cdot 10^{-25}$	$7.41 \cdot 10^{14}$	$5.11 \cdot 10^{-10}$
CH_4	$5.66 \cdot 10^{-25}$	$1.61 \cdot 10^{14}$	$1.11 \cdot 10^{-10}$
H_2O	$5.65 \cdot 10^{-25}$	$1.61 \cdot 10^{14}$	$1.11 \cdot 10^{-10}$
CO	$8.54 \cdot 10^{-25}$	$1.11 \cdot 10^{14}$	$7.51 \cdot 10^{-11}$
CO_2	$1.32 \cdot 10^{-24}$	$7.00 \cdot 10^{13}$	$4.91 \cdot 10^{-11}$

The vacuum lifetime is dominated by the nuclear scattering of protons on the residual gas. Table 2 reports the cross-section at *7 TeV* for such interactions for different gases, as well as the gas densities and pressures at *5 K* compatible with the requested lifetime.

The LHC has the peculiarity of having not one but three different vacuum systems [1]:

- *42 km* of UHV beam vacuum for cryomagnets;
- *48 km* of insulation vacuum for helium distribution lines and the magnet cryostats;
- *6 km* of UHV beam vacuum at room temperature.

Vacuum levels are very different: the room temperature pressure of the insulation vacuum before cool-down does not have to be lower than 10^{-1} *mbar*, while at cryogenic temperatures, in the absence of any significant leak, the pressure stabilises around 10^{-6} *mbar*.

The requirements for the beam vacuum area at room temperature are much more stringent, due to the requested beam lifetime and background to the experiments: pressure must be in the range between 10^{-10} *mbar* and 10^{-11} *mbar*.

All three vacuum systems are subdivided into sectors by vacuum barriers for the insulation vacuum and by sector valves for the beam vacuum.

1.3 THE LHC'S LONG STRAIGHT SECTIONS

Eight Long Straight Sections (LSS) divide the LHC's ring into eight sectors and serve as experimental and utility insertions (Figure 3).
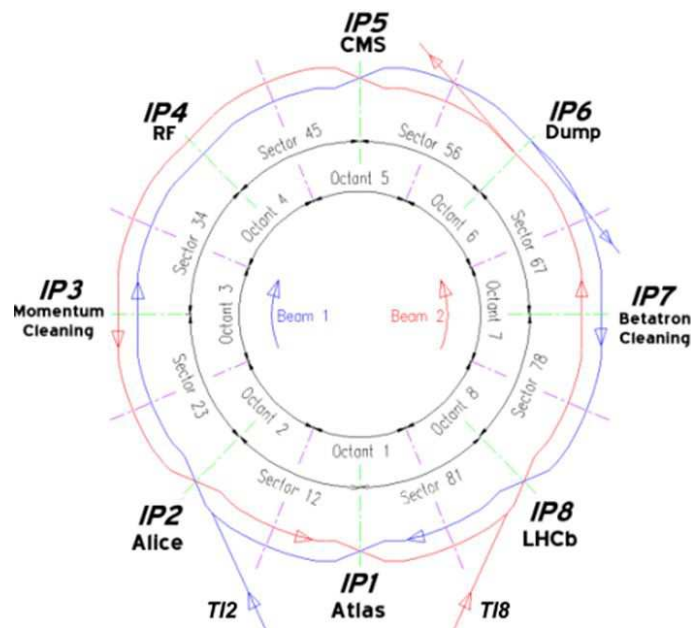
Figure 3 – Schematic view of the LHC, showing the location of the eight Long Straight Sections.

Each LSS has a length of about *450 m* per beam pipe. Four LSS are located in correspondence of the caverns where the main experimental detectors operates along the LHC perimeter (ATLAS in LSS1, CMS in LSS5, Alice in LSS2, LHCb in LSS8) and where the two beams can undergo collisions.

The other four LSS contain respectively the two collimation systems for cleaning the proton beams (LSS3 and LSS7), the radiofrequency cavities for accelerating protons (LSS4) and the beam ejection system (LSS6). LSS8 and LSS2 also house the beam injection system [2].
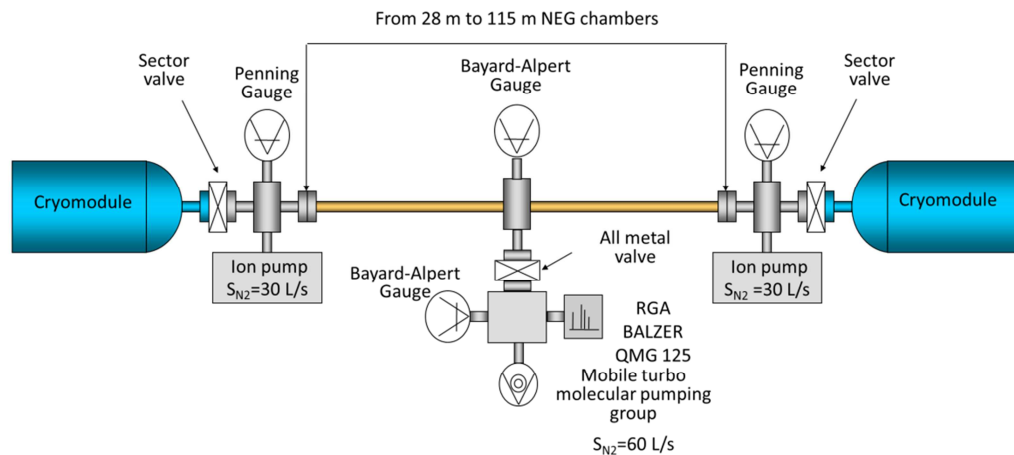
Figure 4 – Schematic view of one typical sector of the LHC's Long Straight Sections.

The LSS are mainly constituted by vacuum beam pipes at room temperature, alternated with stand-alone cryostats (Figure 4). The room temperature parts include beam instrumentation, accelerating cavities, experiments, collimation equipment, injection and ejection kickers and some dipole and quadrupole magnets. In these regions, the vacuum systems for the two beams sometimes merge, not only in the four experimental insertions, but also in some special equipment like the injection kickers and some beam stoppers.

The LSS vacuum chambers are made of several materials: bare or copper plated stainless steel, oxygen-free (OFC) and oxygen-free electronic grade (OFE) copper, aluminium, beryllium, copper plated mu-metal (a mainly nickel-iron alloy with high magnetic permeability). OFC refers to a group of special copper alloys ensuring a high electrical conductivity and a small release of oxygen inside the vacuum chambers. OFE copper, in particular, is characterised by only *0.0005%* oxygen content.

In addition, these vacuum chambers have disparate lengths (ranging from *20 cm* to *7 m*), diameters (between *30 mm* and *450 mm*) and geometries (cylindrical and conical symmetry, circular or elliptical cross-section).

However the baseline for the room temperature beam vacuum system is to use *7 m* long OFC copper chambers, with an inner diameter of *80 mm*, a wall thickness of *2 mm* and fitted with standard DN100 Conflat™ flanges. All these chambers are connected by means of stainless steel bellows equipped with RF copper screens in order to reduce the longitudinal impedance seen by the beam. The chambers are internally coated with a TiZrV non-evaporable getter (NEG) coating, which after having been vacuum activated provides distributed pumping and low outgassing to maintain a low residual gas pressure, as will be extensively explained in Chapter 5. Bakeout and NEG vacuum activation must be performed in order to ensure the required pressure conditions.

Reliable residual gas composition and pressure measurements in the *10^{-11} mbar* range are required in the room temperature part of the beam vacuum system, in order to efficiently check the background conditions for the adjacent experiments and to have early detection of leaks or saturation of the NEG coating. Each one of the sector valves which isolate the sectors at cryogenic temperature from those at room temperature is equipped with bellows and houses a sputter-ion pump. The maximum distance between two sputter-ion pumps is fixed at about *28 m*, to avoid ion-induced pressure instabilities [3]. One Pirani gauge per sector monitors the pressure evolution during the initial pump down from atmospheric pressure. Moreover, every sector is equipped with two cold-cathode ionisation gauges, installed next to the sector valves. Hot cathode ionisation gauges, either permanently installed on the central bellow of the sector or available on mobile diagnostic stations, allow pressure measurements below *10^{-10} mbar*. In the centre of each vacuum sector are installed the pumping ports housing the all-metal roughing valves, necessary for the initial pump-down and for the pumping during the bakeout of each sector. Finally, residual gas analysers mounted on mobile stations allow to characterise the residual gas composition after bakeout and NEG vacuum activation.

2. PRINCIPLES OF VACUUM TECHNOLOGY

Vacuum, from the Latin word *vacuum* meaning void, literally denotes the absence of matter. Although it is impossible to create a *perfect vacuum*, this word is commonly used to refer to a *partial vacuum*, i.e. to a region in which pressure is lower than that of the surrounding atmosphere.

The atmospheric pressure on Earth is not constant but depends on the altitude above sea level *h* according to the following equation:

$$P_{ATM} = P_0 \cdot exp\left(-\frac{g\rho_0 h}{P_0}\right)$$

where $P_0=1$ *atm* is the atmospheric pressure at sea level, $g=9.81$ *m/s²* is gravity acceleration on Earth and $\rho_0=1.293$ *kg/m³* is air density at sea level at *0 °C*; therefore it is not possible to define an upper pressure limit for vacuum.

The aim of vacuum technology is to achieve and to keep inside a vessel or a system a pressure that is lower than the actual ambient pressure.

According with the pressure in a vessel, it is possible to distinguish between different vacuum ranges:

- low vacuum (*~10^3 - 1 mbar*);
- medium vacuum (*1 - 10^{-3} mbar*);
- high vacuum (*10^{-3} - 10^{-7} mbar*);
- ultra-high vacuum (*10^{-7} - 10^{-12}*), usually indicated by the abbreviation UHV.

In this chapter, some fundamental concepts concerning vacuum and its technological aspects will be introduced and discussed [4] [5] [6].

2.1 PRESSURE

Pressure is defined as the force per unit area applied in a direction perpendicular to a surface:

$$P = \frac{F}{A}$$

The unit of pressure in the International System is the pascal (Pa); *1 Pa* is equal to a force of *1 N* exerted on a surface of *1 m²*.

Other useful units to measure pressure are reported in Table 3; in this thesis work pressure values will be always expressed in *[mbar]*, which is the unit commonly used in vacuum technology.

Table 3 – Conversion table for units of pressure.

	Pa	atm	bar	mbar	Torr
Pa	1	$9.87 \cdot 10^{-6}$	10^{-5}	10^{-2}	$7.5 \cdot 10^{-3}$
atm	101325	1	1.013	1013	760
bar	10^{5}	0.987	1	10^{3}	750
mbar	10^{2}	$9.87 \cdot 10^{-4}$	10^{-3}	1	0.75
Torr	$1.33 \cdot 10^{2}$	$1.32 \cdot 10^{-3}$	$1.33 \cdot 10^{-3}$	1.33	1

2.2 IDEAL GAS LAW

A gas is considered ideal if its behaviour obeys the *ideal gas law*:

$$PV = nRT$$

where *P* is pressure, *V* is the gas volume, *n* the number of gas moles, *T* the temperature and *R=8.314 J·mol⁻¹·K⁻¹* is the gas constant.

A gas being at atmospheric pressure or below generally behaves ideally as a first approximation; thus this equation can be easily used to describe the state of a gas as a function of pressure, volume and temperature.

$N_A = 6.022 \cdot 10^{23}$ is the Avogadro number, i.e. the number of atoms, molecules or particles contained in *1 mole*; as *n* is equal to the ratio between *N* (number of gas molecules) and N_A, the ideal gas law can be expressed also in this way:

$$PV = Nk_BT$$

10

where $k_B = 1.38 \cdot 10^{-23}$ *J/K* is Boltzmann constant.

Finally, the dependence of pressure on particle number density can be easily found:

$$P = n_D k_B T$$

where $n_D = N/V$ is particle number density.

2.3 GAS MIXTURES AND PARTIAL PRESSURES

According to Dalton's partial pressures law, the total pressure *P* due to a mixture of two different gases A and B contained in a volume *V* is equal to:

$$P = P_A + P_B$$

For a mixture made up of several components, the total pressure is given by:

$$P = \sum_i P_i = \sum_i n_i \cdot \frac{RT}{V}$$

The molar fraction x_i of a component is given by the ratio between its number of moles n_i and the total amount of moles *n* contained in the volume:

$$x_i = {n_i}/{n}$$

Thus the partial pressures law can be written also in terms of molar fractions and the pressure due to a gas is equal to its molar fraction multiplied by the total pressure in the system:

$$P_i = x_i \cdot n \cdot \frac{RT}{V} = x_i \cdot P.$$

This means that if a gas is made up of different types of gases, each of these gases will exert a pressure that is proportional to its concentration.

2.4 KINETIC THEORY OF GASES

The kinetic theory of gases introduces a model which is useful to describe the behaviour of ideal gases. This model assumes that, if *N* molecules of mass *m* are contained in a volume *V*, each of them has a different velocity $\bar{c}$ (which is a vector defined by three components c_x, c_y and c_z) ranging from *0* to ∞.

Particles are seen as point masses; if two particles are separated by a distance $r<R$ a repulsion is exerted between them and they behave like perfectly elastic spheres of radius $R/2$. The impact causes a change in both velocity value and direction for each particle.

Thus particles do not have a constant velocity and they do not move in specific directions, because they undergo frequent collisions; it is possible to demonstrate that this non-uniform velocity distribution for molecules contained in a vessel is well described by Maxwell-Boltzmann distribution.

According to this model, pressure measured inside a vessel is nothing else but the result of elastic collisions of gas particles against the container walls.

The rules of statistical thermodynamics allow defining different velocities for this distribution [7]; in particular the most probable velocity is defined as follows:

$$c_{mp} = \left(\frac{2RT}{M}\right)^{1/2}$$

Another useful quantity for vacuum calculations is the mean x-component of velocity:

$$\frac{\bar{c}}{4} = \left(\frac{RT}{2\pi M}\right)^{\frac{1}{2}}.$$

Both this quantities are expressed in *m/s*.

It is possible to define also another useful quantity, i.e. the flux or flow rate per unit area, which is given by:

$$J_N = \frac{n_D \bar{c}}{4}$$

where n_D is particle number density.

2.4.1   Mean free path

The mean free path is the average distance that a gas molecule is able to cover between two successive collisions with other molecules contained in a vessel.

The number of collisions that a single particle makes per second is:

$$z = \sqrt{2}\bar{c}n_D\sigma$$

where $\sqrt{2}\bar{c}$ is the average relative speed of the particle, n_D is the particle number density and $\sigma=\pi d^2$ is the collisions cross-section for a single gas, with d representing the diameter of the particle. If a mixture of two gases is considered instead, d is equal to the sum of the radii of the colliding particles r_1+r_2.

It follows that the mean free path is given by:

$$\bar{l} = \frac{\bar{c}}{z} = \frac{1}{\sqrt{2} n_D \pi d^2} = \frac{k_B T}{\sqrt{2} P \pi d^2}.$$

It is thus a function of the gas state in the vessel, i.e. a function of temperature, pressure and molecular diameter.

For air at room temperature and atmospheric pressure, the mean free path is equal to *70 nm*, while at *10^{-6} mbar* it becomes *50 m*.

2.5 DIFFUSION AND FICK'S LAWS

Diffusion is a transport process driven by a concentration gradient which implies mass transfer; this phenomenon is described by two partial differential equations, commonly known as Fick's laws.

The first law is given by the following equation:

$$J_x = -D \frac{\partial C}{\partial x}$$

where *C* is the concentration of the diffusing species and *D*, expressed in *[m^2/s]*, is the diffusion coefficient (or diffusivity) of a gas given by:

$$D(T) = D_0 \cdot e^{-E_0/RT}$$

where D_0 is a constant and E_0 is the activation energy for diffusion of that gas.

Fick's first law is valid only under steady state conditions (i.e. concentration is not time-dependent) and states that the flux along a given direction *x* goes from high concentration to low concentration regions, with a magnitude which is proportional to the concentration gradient in the same direction; the generalised equation for three dimensional systems, taking *D* as a constant, is the following:

$$J = -D \cdot \nabla C.$$

Fick's second law describes the variations of concentration with time:

$$\frac{\partial C}{\partial t} = D \frac{\partial^2 C}{\partial x^2}$$

Similarly to the previous case, it is possible to write an equation valid also for more dimensions:

$$\frac{\partial C}{\partial t} = D\nabla^2 C.$$

Finally, the diffusion length during time t at temperature T is given by:

$$L = \sqrt{D(T) \cdot t}$$

2.6 TYPES OF FLOW

Gas pressure affects the behaviour of gas flow. Knudsen number is a dimensionless quantity describing the type of flow in a system and it is defined as the ratio between the mean free path of molecules and a characteristic dimension of the vacuum component, e.g. its diameter:

$$Kn = \frac{\bar{l}}{d}$$

As pressure changes, it is possible to define three different types of flow in a vacuum system:

- *continuous* (or *viscous*) *flow* in the low vacuum field (*Kn<0.01*);
- *Knudsen flow* in the medium vacuum range (*0.01<Kn<0.5*);
- *molecular flow* in the high and ultra-high vacuum ranges (*Kn>0.5*).

Viscous flow can be in turn laminar or turbulent; the distinction between these two types of flow is made by another dimensionless number, i.e. Reynolds number:

$$Re = \rho \frac{vd}{\mu}$$

where ρ is gas density, μ is viscosity, v is flow velocity and d is the diameter of the component; for circular tubes, flow is laminar if *Re<2300* and becomes turbulent for *Re>4000*. Continuous flow occurs when intermolecular collisions are more frequent than molecule-wall collisions. Knudsen flow instead is a transitional flow that occurs for example when pumping down vacuum chambers; in this case, both collision types have an influence on the flow. Finally, in ultra-high vacuum (*P<10^-7 mbar*) molecular flow occurs and $\bar{l} \gg d$, i.e. the mean free path is much larger than the component dimensions; in this case, it is very difficult for a molecule to have interactions with other molecules.

In spite of this, even under UHV conditions it is not possible to talk about a perfect void (Table 4). At *P=10^-12 mbar* and *T=25 °C*, there will still be around *2.5·10^4 molecules/cm^3*.

	Pressure [mbar]	Mean free path	Molecules/cm^3
Rotary vane pump	$1 - 10^{-3}$	100 µm – 10 cm	$10^{16} - 10^{13}$
Incandescent light bulb	$0.1 - 0.01$	1 mm – 1 cm	$10^{15} - 10^{14}$
Thermos bottle	$10^{-2} - 10^{-4}$	1 cm – 1 m	$10^{14} - 10^{12}$
Vacuum tube	$10^{-9} - 10^{-11}$	100 km – 10^3 km	$10^7 - 10^5$

2.7 GAS FLOW

Gas flow rate in vacuum technology is usually expressed as PV-flow rate (or PV-throughput):

$$Q_{P\dot{V}} = P\dot{V} = P\frac{\mathrm{d}V}{\mathrm{d}t}.$$

Pumping speed is defined as the volume flow rate of gas that a vacuum pump is able to displace:

$$S = \frac{dV}{dt}$$

The typical units for pumping speed are *[l·s^{-1}]*.

The pumping speed of a given pump is equal to the ratio between the flux of pumped gas and the pressure of the same gas at the aperture of the pump itself.
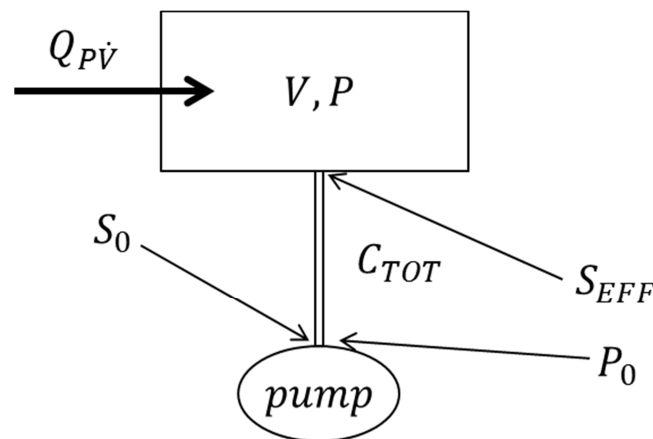
Figure 5 – Schematic diagram of a basic vacuum system.

Therefore by multiplying the volume flow rate by the inlet pressure of a pump it is possible to calculate its PV-throughput, whose units are *[mbar·l·s^{-1}]*:

$$Q_{P\dot{V}} = S \cdot P.$$

According to the system described in Figure 5, S_0 refers to the pumping speed measured at the inlet of the pump, while the effective pumping speed S_{EFF} takes into account the resistance to the gas flow of pipes and valves before the pump; this means that $S_{EFF}<S_0$.

The relationship between S_{EFF} and S_0 is given by:

$$\frac{1}{S_{EFF}} = \frac{1}{S_0} + \frac{1}{C_{TOT}}$$

where C_{TOT} is the total conductance of all the pipes and valves between the system and the pump.

The conductance of a given component is defined as the inverse of flow resistance, by analogy with electric circuits; it is given by the ratio between the gas flow rate and the pressure difference across the component:

$$C_{TOT} = \frac{Q_{P\dot{V}}}{\Delta P} = \frac{Q_{P\dot{V}}}{P - P_0}$$

This means that if a gas flow crosses a component, there will be a pressure drop proportional to its conductance, which is a function of the component's shape, of temperature and of the type of gas.

The units of conductance are $[l \cdot s^{-1}]$, as for pumping speed.

In order to characterise the properties of a vacuum system or a pipe, the concept of transmission (Tr) has to be introduced; it can be defined as the ratio between the amount of particles entering in a vacuum component and the amount coming out from it, i.e. the inverse of transmission probability. Backscattering instead refers to particles that go back to the direction they came from, due to diffuse reflection on the walls of the vacuum component.

According to the ideal gas law ($PV=nRT$), the transmission of a vacuum chamber can be also defined as the ratio between the pressures at the entrance and at the end, respectively.

2.7.1 Series and parallel connection of conductances

If several conductances are connected one to the other, it is possible to calculate a total conductance, again by analogy with the same calculation for electric circuits (Figure 6).

For a series connection of i conductances, the following relationship is valid:

$$\frac{1}{C_{TOT}} = \sum_i \frac{1}{C_i}$$

For parallel connections instead:

$$C_{TOT} = \sum_i C_i$$
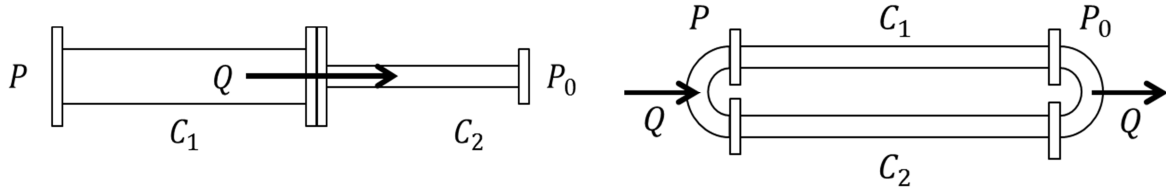
Figure 6 – Series (left) and parallel (right) connection of conductances.

2.7.2 Conductance of an aperture

If molecular flow conditions are established (*Kn>0.5*), the mean free path of particles is bigger than the smallest dimension of the flow channel; this leads to the assumption that, for a thin-walled orifice, the transmission can be assumed equal to one, because the wholeness of the injected particles will flow through the aperture without collisions with its walls and thus without being backscattered.

Therefore the conductance of an aperture can be calculated as follows:

$$C_{AP} = \frac{\bar{c}}{4} \cdot A$$

where *A* (expressed in *cm^2*) is the cross-section of the aperture and $\bar{c}/4$ is the mean x-component of velocity for a Maxwell-Boltzmann distribution of particles and is derived from:

$$\frac{\bar{c}}{4} = \sqrt{RT/2\pi M}$$

This is also numerically equal to the maximum area-related pumping speed of an ideal pump for a gas at temperature *T*. Therefore for a molecular flow of air (*M≈29 g/mol*) at 20 °C it is possible to find the following expression:

$$C_{AP,AIR,20\,°C} = 11.6 \cdot A$$

with *C* expressed in *[L/s]* and *A* in *[cm^2]*. The same equation remains valid for a different gas *x* at different temperature by multiplying for an appropriate factor:

$$C_{AP,X,T} = C_{AP,AIR,20\,°C} \cdot \sqrt{\frac{M_{AIR} \cdot T}{293.15 \cdot M_X}}$$

If temperature is assumed to remain constant, the relationship between the conductance of air and of a gas *x* becomes:

17

$$\frac{C_X}{C_{AIR}} = \sqrt{\frac{M_{AIR}}{M_X}}$$

2.7.3 Conductance of a pipe with constant cross-section

For the calculation of the conductance of a tube (i.e. an aperture with a non-negligible wall thickness), although molecular flow still occurs, transmission must be assumed different from one; the conductance of a tube can be regarded as the conductance of the pipe entrance C_{AP} multiplied by a factor representing the probability Pr that the molecules entering the system will be transmitted through it:

$$C_{PIPE} = C_{AP} \cdot Pr$$

This probability can be seen as proportional to the ratio between a "transmitting area" and an "obstructing area", which is in turn proportional to the total surface area of the tube; this leads to the following expression:

$$Pr = \frac{A_{TR}}{A_{TR} + lh}$$

where, l being the length and h the perimeter of the pipe cross-section, lh is the total area of the pipe walls.

Some correction factors have to be introduced in order to take into account that A_{TR} is generally larger than the real cross-section A and that the obstructing area is smaller than the actual wall area lh; these considerations lead to the following formula:

$$C_{PIPE} = C_{AP} \left(1 + \frac{3}{16} \cdot \frac{lh}{A}\right)^{-1}.$$

For a pipe with a circular cross-section ($A=\pi r^2$ and $h=2\pi r$) it is possible to obtain:

$$C_{PIPE} = C_{AP} \cdot \left(1 + \frac{3}{8} \cdot \frac{l}{r}\right)^{-1} \cdot \beta^{-1}$$

where β is a correction factor depending on the ratio l/r; for long tubes ($l \gg r$) a simplified expression is introduced:

$$C_{LONG\ PIPE} \cong \frac{\pi \bar{c} d^3}{12l}.$$

Finally for air at *20 °C* it is possible to assume that:

$$C_{LONG\ PIPE} = 12.1 \frac{d^3}{l}.$$

C is always expressed in *[L/s]*, while *d* and *l* are in *[cm]*. Again, the conductance of a gas *x* at room temperature can be obtained from:

$$\frac{C_X}{C_{AIR}} = \sqrt{\frac{M_{AIR}}{M_X}}$$

2.8 GAS SOURCES IN VACUUM SYSTEMS AND PARTICLE ACCELERATORS

Several gas sources are usually present in every vacuum system (Figure 7): leaks, outgassing from the chamber walls, permeation are among these sources that cannot be completely eliminated [5] [6]. In order to size the pumping systems needed to maintain the required vacuum degree, the gas loads from these different sources have therefore to be known.
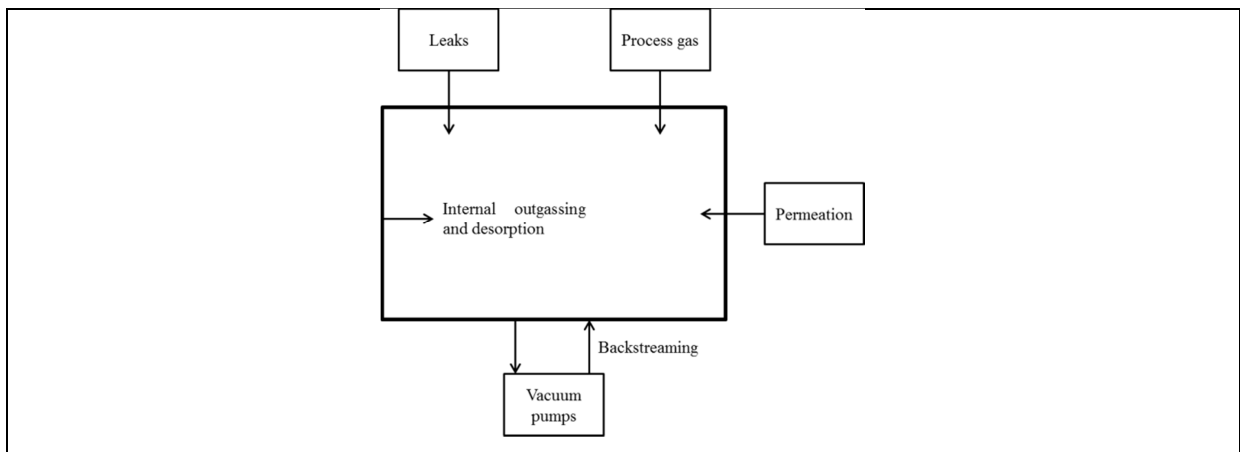
Figure 7 – Gas sources in vacuum systems.

Leaks are undesired flow paths in the boundary of a vacuum system that allow fluids to enter in it; they can generate from defects of fabrication (weldings, careless handling of components, etc.) or from cracking due to an applied strain. The presence of leaks has to be avoided because they introduce inside the vacuum systems external gases and vapours, normally air, thus compromising the required vacuum conditions.

Permeation is related to the possibility for a gas molecule to be adsorbed on the high-pressure side of a material, to diffuse through it and to be finally desorbed on the low-pressure side, i.e. inside the vacuum system. All materials exhibit a certain permeability for gases, which

depends on the type of gas and the type of material and strongly increases with temperature. At room temperature, permeation through metals is negligible and these materials can be considered as impermeable to air even at high temperatures; the highest permeability for a gas through metals is of course observed with H_2, due to the small dimensions of its molecule and to the fact that it undergoes dissociation when it is adsorbed.

Concerning polymers used for seals, this phenomenon has to be taken into account in systems where pressures below *10^{-7} mbar* have to be achieved and its extent strongly depends on the nature of the polymer.

Finally, any material that has been exposed to air or to a certain gas will adsorb this gas on its surface. Once installed in a vacuum system where vacuum or UHV conditions are established, the internal walls of every of its components will tend to desorb the previously adsorbed gas and outgassing occurs, thus requiring the presence of appropriate pumping systems. The outgassing is time-dependent: it decreases with pumping time and it strongly depends on the type of material: polymers generally show higher outgassing rates than metals and ceramics. It can be considered a thermal outgassing, which is enhanced as the temperature increases.
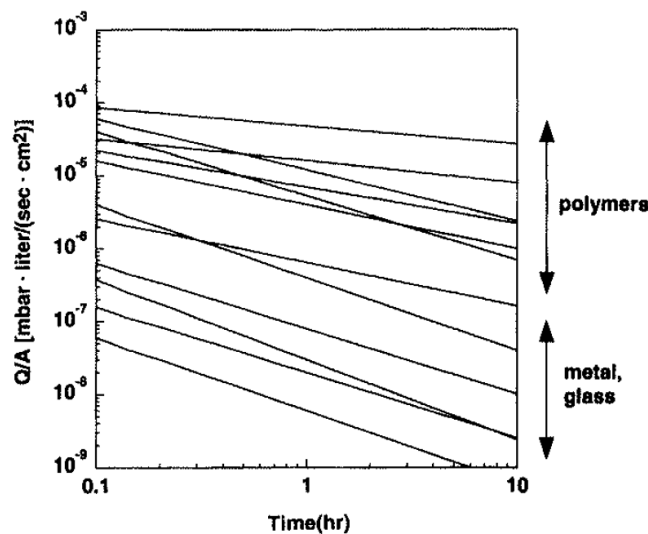
Figure 8 – Time-dependence of the outgassing flow rate for different materials [6].

At constant temperature, the time-dependence of the outgassing flow rate is the following:

$$\dot{Q}_{OUT} = \frac{a_{1h}A}{(t/1h)^\alpha}$$

20

where $\dot{Q}_{OUT}$ is the gas throughput, A is the outgassing area, a_{1h} is the specific outgassing rate after *1 h* of pumping and α is the exponent of decay, i.e. the negative slope of the outgassing log/log curve of $\dot{Q}_{OUT}/A$ versus time (Figure 8).

2.8.1 Bakeout of vacuum systems

Vacuum systems for UHV applications are entirely made of metallic components. For this reason, permeation can be neglected and, if no leaks are present, the only possible gas source in UHV systems is constituted by thermal outgassing and desorption from the inner walls of vacuum components.

After having been exposed to the atmosphere, a metal surface is covered by a homogeneous oxide layer, by a mix of hydroxide and hydrocarbons and, above all, by water molecules.

At atmospheric pressure, due to its polar nature, water is strongly bonded the metallic surface thanks to electrostatic interactions. In vacuum conditions however, water desorption dominates the degassing of metals, according to the above-mentioned outgassing equation; the degassing of other gases, namely CO and H_2, corresponds to less than *10%* of the total desorbed gas quantity [8].

In order to mitigate these effects and to accelerate water desorption, vacuum systems for UHV applications should undergo a bakeout before starting operations.

A bakeout consists in an artificially accelerated water outgassing that is obtained by heating a vacuum system to an appropriate temperature. This heating process significantly increases desorption and diffusion rates, causing the release from the inner surfaces of the system of a large amount of volatile compounds, which are subsequently removed by the installed pumping systems.

The desorption frequency ν for molecules from a surface corresponds to the probability of desorption per adsorbed species per unit time and it is given by:

$$\nu = \nu_0 \cdot e^{-\left(E/k_B T\right)}$$

where E is the binding energy between a molecule and the surface, i.e. activation energy necessary for the desorption of a molecule. This frequency thus depends on the nature of the gas-surface interaction and on temperature. The value of E is a function of the type of attractive forces involved: adsorption processes due to weak interactions like Van der Waals forces are called physisorption processes, while those involving stronger covalent, ionic or metallic bonds are referred to as chemisorption processes.

The mean sojourn time τ of a molecule on a surface is the reciprocal of the frequency and therefore corresponds to:

$$\tau = \frac{1}{\nu} = \tau_0 \cdot e^{\left(E/k_B T\right)}$$

The mean sojourn time is directly proportional to the binding energy and inversely proportional to the temperature: for the same binding energy, an increased temperature results in a shorter mean sojourn time (Figure 9). This explains why desorption of molecules from a surface is enhanced if temperature is increased by heating the vacuum system's components.
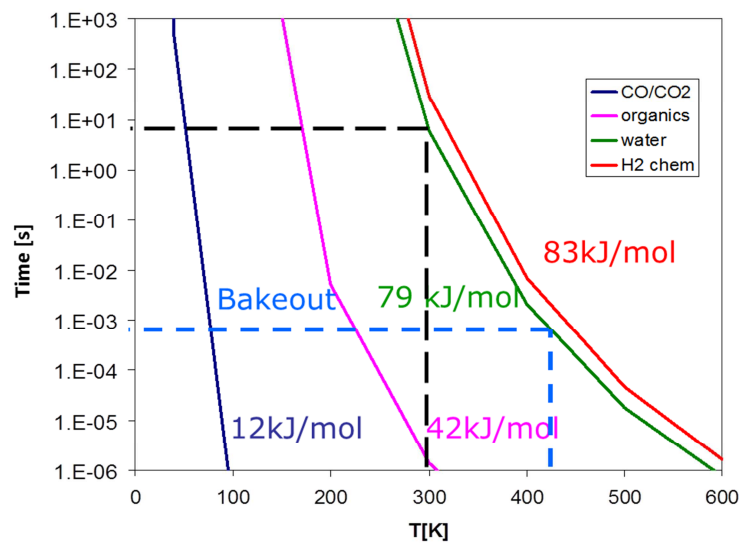
Figure 9 – Mean sojourn time as a function of temperature for different gases-surface interactions involving different binding energies.

Bakeout procedures thus are based on the fact that desorption rate exponentially depends on temperature. Typically, the system is pumped into the range where the residual pressure is dominated by desorption processes. The temperature is then raised, either by external heaters or by a high-intensity source within the vacuum chamber. After a certain period of hours, the system is cooled down to room temperature.

During a bakeout of a vacuum system, pressure drastically increases of several orders of magnitude, due to the enhanced desorption from the inner metallic surfaces (Figure 10).

Once the bakeout is over and all the water has been desorbed and pumped, the degassing of a vacuum system becomes dominated by hydrogen, which does not come from the surface but rather from the bulk of the metallic components, where this gas is usually included during metallurgic processes. In addition to H_2, the other main residual gases generally present in a vacuum system after a bakeout are CO, CO_2 and hydrocarbons (in particular CH_4).
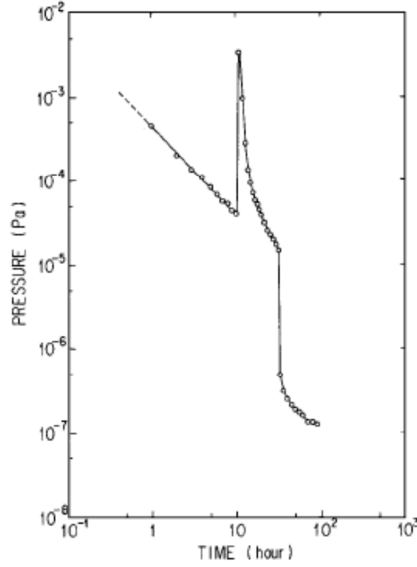
Figure 10 – Typical pressure profile during the bakeout of a vacuum system [9].

2.8.2 Beam-induced desorption in the LHC

During beam operations in high-energy particle accelerators as the LHC, the gas density inside the storage ring is dominated by dynamic effects due to ion, photon and electron induced gas desorption from the beam vacuum chamber walls [10].

These phenomena can lead to an undesired increase of pressure, causing a reduction of the beam lifetime and luminosity and an increase of the background noise in the LHC's experiments. Static vacuum conditions instead refer to the already mentioned situations when no beam is circulating.

Ion induced desorption occurs when the circulating proton beam ionises the residual gas inside the storage ring; the so-created positive ions are repelled with high kinetic energy (up to several *keV*) by the positive charge of the beam and they impinge on the vacuum chamber walls, stimulating the desorption of tightly bounded gas molecules. The desorbed gas can be in turn subsequently ionised, thus giving rise to a pressure runaway if the provided pumping speed is not sufficient.

A formula describes the pressure increase P_i as a function of the circulating beam current:

$$P_i = \frac{P_0}{1 - \eta_i I / (\eta_i I)_{critic}}$$

where P_0 is the initial pressure value, I is the beam current and η_i is the net ion desorption yield. The critical value reported in the equation determines an upper stability limit for pressure and it is given by:

$$(\eta_i I)_{critic} = \frac{e}{\sigma} S_{distr}$$

where e is the electron's charge, σ is the ionisation cross-section of the residual gas molecules for high-energy protons and S_{distr} is the distributed effective pumping speed in the system.

The critical current inside a given LHC vacuum sector depends on its pumping configuration, i.e. on the number, nature and position of the installed pumping systems: the less the pumping is efficient, the lower will be the critical current for vacuum instability.

Photon-stimulated desorption instead is a consequence of the structural characteristics of the LHC and all the synchrotron light accelerators: when a charged particle is accelerated longitudinally or transversally, it produces a radiation. Due to the centripetal acceleration in the bending magnets that constitute 48 km of the LHC vacuum chambers, the beams emit a synchrotron radiation (SR) flux of about 10^{17} $photons \cdot s^{-1} \cdot m^{-1}$ at nominal conditions. This radiation hits the vacuum chamber walls and causes gas desorption, resulting in a pressure increase P_{ph} that is proportional to the photon flux Γ_{ph} and to the photon desorption yield η_{ph} and inversely proportional to the pumping speed S:

$$P_{ph} \approx \frac{\eta_{ph} \cdot \Gamma_{ph}}{S}$$

The LHC is the first particle accelerator producing a significant quantity of synchrotron radiation (SR): at $7\ TeV$ per beam the photon flux is about three times larger than it was for the previously operating LEP. On the other hand, due to the fact that the LHC accelerates protons instead of electrons, the dissipated power by SR is much lower [11].

Finally, photoemission and ionisation of the residual gas inside the vacuum chambers produce a large amount of primary electrons, which move under the action of beam field forces and of their charge. These electrons could create a quasi-stationary electron cloud (EC) and they can strike the beam pipe walls, causing again gas desorption and pressure increase [12]. The effects of this phenomenon are enhanced in the experimental vacuum beam pipes, where magnetic field is non-uniform, the geometry of the chambers may vary and the two beams travel in the same vacuum beam pipe in opposite directions.

The pressure increase P_e due to the electron cloud, in analogy with the equation for SR, depends on the electron desorption yield η_e, the pumping speed S and the electron flux Γ_e:

$$P_e \approx \frac{\eta_e \cdot \Gamma_e}{S}$$

Figure 11 shows the typical effects of EC and SR during the injection of a proton beam in the LHC. The red line indicates the beam coming from the SPS accelerator, which is injected in *12* steps with energy equal to *450 GeV*. When the injection is over, the beam is progressively accelerated to the maximum energy (in this case, *4 TeV*). P_1 shows the effects of the beam on a gauge located in one of the LSS: soon after the beam injection, the gauge records a pressure peak which is due to EC. P_2 instead corresponds to pressure measured by a gauge located just at the end of one of the arcs: in this case, the pressure increase appearing when the maximum energy is reached is due to the SR flux hitting the walls of the beam pipe at the exit of the bending arc.
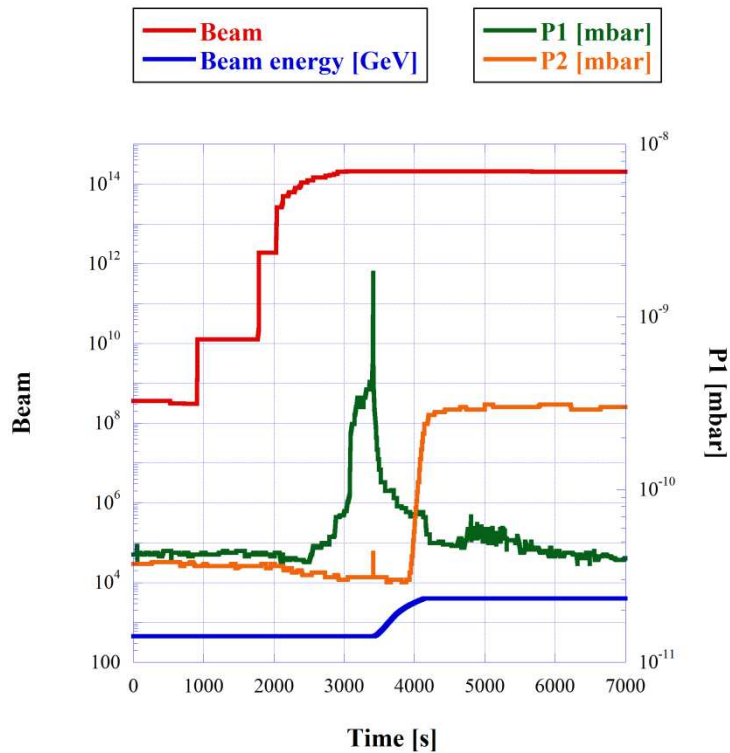
Figure 11 – Pressure variations due to EC and SR during a typical proton beam injection in the LHC.

3. PUMPS AND PUMPING SYSTEMS

Depending on the degree of vacuum which is needed, different types of vacuum pumps are available in order to create and to maintain the required conditions.

As a matter of fact, each of these pumping systems is able to work properly only in a well-defined pressure range, while outside it its performances drastically drop.

In some situations a combination of different pumps is required in order to ensure efficient performances. This is the case for example of pumps operating in the HV/UHV range: continuous operation of backing pumps, which work directly to the atmosphere and reduce pressure to an intermediate value, is needed.

The type of pump or combination of pumps chosen for an application depends on the gas load to be handled and on the base pressure to be achieved in a given time.

It is possible to divide vacuum pumps into two different groups, according to their working principle [4] [5]:

- gas-displacement vacuum pumps (also known as gas-transfer pumps);
- gas-binding vacuum pumps.

Gas-displacement pumps can be in turn classified in two groups: positive displacement pumps (displacing gas from sealed areas to the atmosphere or to a downstream pump stage) and kinetic pumps (displacing gas by accelerating it in the pumping direction).

Gas-binding pumps instead either bind the gas to an active substrate (gettering) or condense it at a suitable temperature.

3.1 GAS-DISPLACEMENT VACUUM PUMPS

The functioning principle of gas-displacement vacuum pumps is based on the mechanical removal of gas molecules through positive displacement (primary pumps) or momentum transfer (turbomolecular pumps).

3.1.1 Primary pumps

These pumping systems are employed in order to achieve pressures in the rough-medium range and to back high and ultra-high vacuum pumps.

Oil-sealed rotary pumps, dry pumps and piston pumps are among the most used primary pumping systems for the achievement of the above-mentioned goals.

3.1.2 Turbomolecular pumps

Turbomolecular pumps (TMP) belong to the family of kinetic (momentum transfer) vacuum pumps. They are extensively employed in systems where high or ultra-high vacuum conditions are required.

A multi-stage, turbine-like rotor with bladed disks rotates in a housing; inverted bladed stator discs having similar geometries are interposed between the rotor discs. The rotor is driven at very high rotational speeds, so that the peripheral speed of the blades is similar to the thermal velocity of the pumped gas molecules.

Molecules collide with the blades and blade speed is added to their thermal speed; in order to ensure a good functioning of the pump, molecular flow conditions are required inside the component. If this were not true, the speed component transferred by the blades would be lost due to collisions with other molecules; the mean free path thus must be larger than the spacing between two blades. Pumped gas is compressed along the rotor-stator assembly which is made of several stages, everyone of them corresponding to the combination of a rotor and stator disc; a downstream backing pump provides further compression to atmospheric pressure. Pumping speed of a turbomolecular pump begins to decrease when the inlet pressure is around 10^{-2}-10^{-3} mbar due to the transition from molecular to Knudsen or laminar flow; however, acceptable rotational speeds can be maintained for a few minutes even up to *1 mbar*, allowing to handle relatively high inlet pressures.

The compression ratio k of a TMP, giving an indication of its functioning, is defined as the maximum ratio between discharge pressure P_2 and inlet pressure P_1:

$$k = \frac{P_2}{P_1}$$

Pumping speed for light gases is lower compared to that for N_2, because the pumping probability is lower; however the inlet aperture has an increased conductance for lighter gases, giving rise to a pumping speed for H_2 and He which is reasonably close (*0.8-0.9*) to that for N_2.

3.2 GAS-BINDING VACUUM PUMPS

Unlike gas-displacement vacuum pumps that can be used without limitation, gas-binding pumps have a limited gas absorption capacity and must be regenerated after having operated for a certain period.

The absorption of gas can be obtained thanks to an active substrate (sputter-ion pumps and getter pumps) or by condensation of gas molecules at a suitable temperature.

Cryopumps apply this latter mechanism and are widely employed in the arcs of the LHC, where temperature is kept by means of superfluid helium at *1.9 K*, in order to ensure the superconducting properties of the magnets. However cryopumps have not been employed for the purposes of this thesis work and therefore they will not be described in detail.

Sputter-ion pumps and getter pumps can be employed only in the ultra-high vacuum pressure range, otherwise their absorption capacity would be instantaneously exhausted.

3.2.1 Sputter-ion pumps

The pumping mechanism of sputter-ion pumps (SIP) is based on sorption processes initiated by gas ions formed in a Penning discharge (see Paragraph 4.1.2) maintained by a strong homogeneous magnetic field (*0.1÷0.2 T*). Ions impinge on parallel cathode plates made of a getter material such as Ti and sputter the getter, which adheres to nearby surfaces within the pump and adsorbs reactive gases. Gas ions with sufficient energy can also implant themselves directly within the cathode: this latter pumping mechanism is effective for all types of gases, including noble gases. The pumping speed of a SIP depends on the type of gas and the pressure. A prolonged use of these devices at pressures higher than the high vacuum range has to be avoided because it can cause cathode heating and degassing.

3.2.2 Getter pumps

Evaporable getter pumps are based on chemisorption of reactive gases on the surface of a getter film. They are obtained by vacuum sublimation and deposition of a fresh getter film on a metallic surface. When one or more monolayers have been formed, the sorption speed drops rapidly and a new adsorbing surface must be formed by further evaporation.

Titanium sublimation pumps, consisting in a stainless steel body containing the evaporation source and a screen collector for the evaporated material, are among these kinds of devices.

Non-evaporable getter pumps instead, which constitute the main topic of this thesis work, deserve a separate chapter and will be thoroughly described afterwards.

4. VACUUM PRESSURE MEASUREMENTS

4.1 TOTAL PRESSURE MEASUREMENTS

Different methods for pressure measurement are nowadays available, but none of them covers the entire pressure range that is possible to find inside a vacuum system: it is therefore necessary to use different sensors (Figure 12).

The choice has to be done according to the vacuum degree that has to be detected and to the required sensitivity; moreover, gas composition (inert or corrosive) and environmental conditions (e.g. radioactivity) are important criteria that must be considered.

As already said, pressure is directly related to the particle number density in a system; according to this, total pressure measurements can be of two types:

- – direct pressure measurements;
- – indirect pressure measurements.

In the case of direct methods, pressure is measured in accordance with its definition: the result of the measurement is the shift of a known surface *A* on which a pressure *P*, proportional to the deflection, is exerted.

Manometers are devices typically used for direct pressure measurements. Other methods involve the deformation of a sensitive element, e.g. a diaphragm, due to an applied force: the resulting deflection can be for example estimated mechanically (diaphragm vacuum gauges) or electrically (piezo-diaphragm vacuum gauges) [4] [5].

This process does not depend on the nature of the analysed gas or gas mixture; at low pressure (less than *1 mbar*) however, the exerted forces are negligible, thus the performance of direct measurements becomes very difficult or even impossible due to the infinitesimal masses involved. In this situation, which is common concerning to applications in high and ultra-high vacuum, indirect methods are required.

Indirect measurements monitor either particle number density or a gas property which depends on it, taking into account that pressure is proportional to particle number density at constant temperature. These methods depend on the gas type because the physical properties

which are measured (e.g. thermal transfer and ionisation capacity) are functions of both pressure and molecular weight.

It is thence common, in the case of gas dependent methods, to refer the measured pressures to a nitrogen equivalent value, which can be calculated by calibrating the gauge.

In the next paragraphs, some examples of devices for indirect pressure measurements will be presented and their functioning principles described.
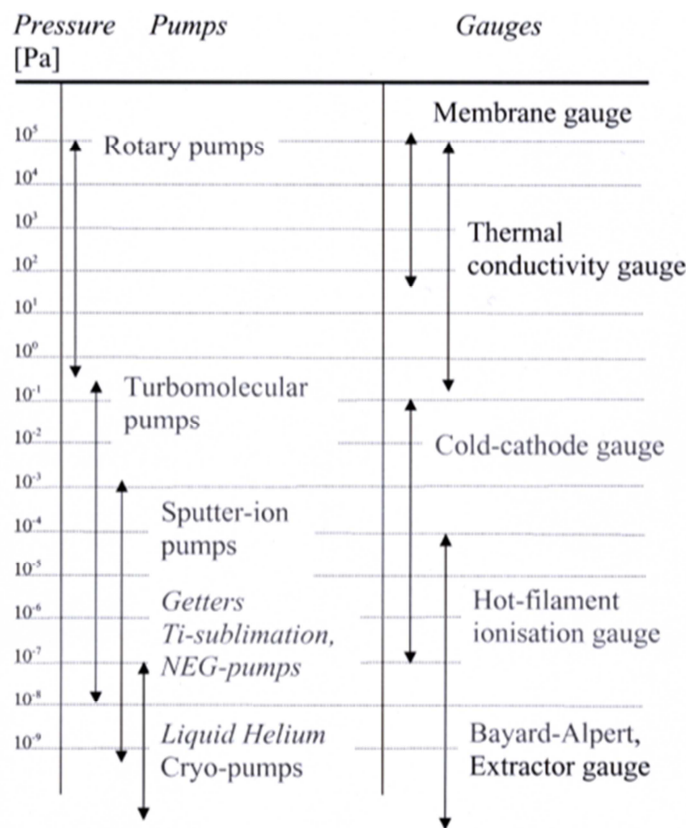
Figure 12 – Operating pressure ranges of different vacuum gauges and vacuum pumping systems.

4.1.1   Thermal conductivity vacuum gauges

This type of gauges, also known as Pirani gauges, is focused on the measurement of the thermal conductivity of gases, which in molecular flow conditions is proportional to particle number density and thus to pressure.

A Pirani gauge is made of a tube containing a tungsten wire, which is electrically heated to a temperature between *110 °C* and *130 °C*; the corresponding applied electrical power is equal to:

$$\dot{Q}_{elec} = V \cdot I$$

Heat dissipation can occur according to three different mechanisms:

30

- heat transfer to the tube's wall by means of the gas surrounding the wire;
- heat loss through the wire ends;
- convection and radiation.

The sum of these three contributions should be equal to the applied power:

$$\dot{Q}_{TOT} = \dot{Q}_{gas} + \dot{Q}_{rad} + \dot{Q}_{ends}$$

Pirani gauges work properly between *1 mbar* and *10^{-4} mbar*: in this interval, if temperature remains constant, gas thermal conductivity is predominant and heat transfer is a linear function of pressure. In this case, by measuring the voltage needed to maintain the wire's temperature constant, it is possible to obtain the corresponding pressure value.

This correlation however is not linear over the whole possible pressure range: the lower limit is due to the fact that, at lower pressures, the gas thermal conductivity would be negligible compared to the thermal transfer along the wire ends. If *P>1 mbar* instead, heat loss by convection and radiation becomes predominant.

4.1.2 Ionisation gauges

An ionisation gauge measures pressure in a vacuum system by ionising a fraction of the gas molecules contained in it; the generated ions are collected on a positive electrode and the ion current, which is proportional to the particle number density, is measured by means of an electrometer, giving an indirect measure of the pressure in the system.

It is possible to distinguish between two types of ionisation gauges, the main difference being the source of the ionising particles.

4.1.2.1 *Cold cathode ionisation gauges*

The functioning of these ionisation gauges is based on the establishment of a gas discharge between two unheated electrodes, by means of a high voltage.

Due to the high voltage, negatively charged electrons leave the cathode and move from it to the anode; during their travel, electrons can ionise neutral gas molecules, creating a gas discharge.

In order to increase the device's sensitivity and to ensure that a sufficient quantity of ions is created to maintain the gas discharge even at low pressure, a strong magnetic field (*0.1-0.2 T*) is established, by means of which the electrons are forced to travel on spiral trajectories and their path is significantly extended, thus increasing the probability of collisions with gas molecules.

Usually the design of this type of gauge is the following (Figure 13): a metal wire, i.e. the anode, is surrounded by a concentric metallic chamber, which constitutes the cathode. An axially- magnetised, cylindrical magnet ring is placed on the exterior of this measurement chamber and generates the needed magnetic field.
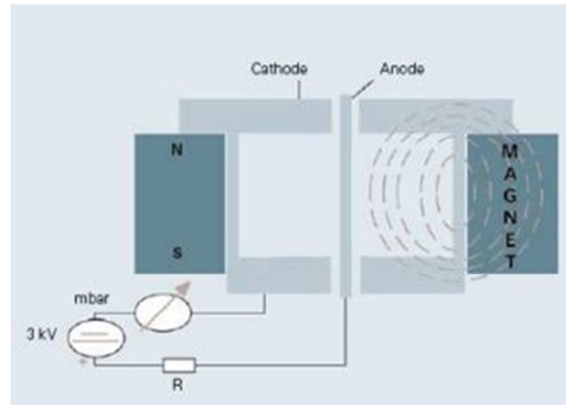
Figure 13 – Schematic view of a cold cathode ionisation gauge.

The discharge current is measured and pressure is obtained due to its relationship with particle number density; the so-obtained pressure is a function of the gas type because each gas is characterised by a different collision cross-section.

The discharge current I_D can be calculated according to the following relationship:

$$I_D = I_R K P$$

where I_R is the ring current established in the anode and sustaining the discharge and K is a constant; it depends on the type of gas and the gauge geometry and it is experimentally determined.

The sensitivity S of the gauge instead can be defined as:

$$S = I_R K$$

It has to be taken into account that the pressure measurement can be different from the actual pressure because gas ions can be absorbed by implantation on the cathode surface. As a matter of fact, SIPs are based on sorption processes initiated by gas ions formed in a Penning discharge. Sputter-ion pumps achieve their pumping speed by incorporating many individual Penning cells. Due to this pumping effect, the gauge behaves like a getter pump: this effect characterises also hot cathode ionisation gauges, but the related pumping speed is much greater for cold cathode ones.

Penning gauges are the most commonly used cold cathode ionisation gauges; they allow the measurement of pressure ranging from about 10^{-3} mbar to 10^{-9}-10^{-10} mbar.

32

4.1.2.2 Hot cathode ionisation gauges

In this case the ionising particles are electrons thermoionically emitted by a heated cathode, usually a tungsten wire (Figure 14). The electrons are accelerated by a high voltage applied between the cathode and the anode, acquiring a high kinetic energy; along their path, electrons can collide with gas molecules which may be positively ionised.

A = Anode
C = Cathode
IC = Ion collector
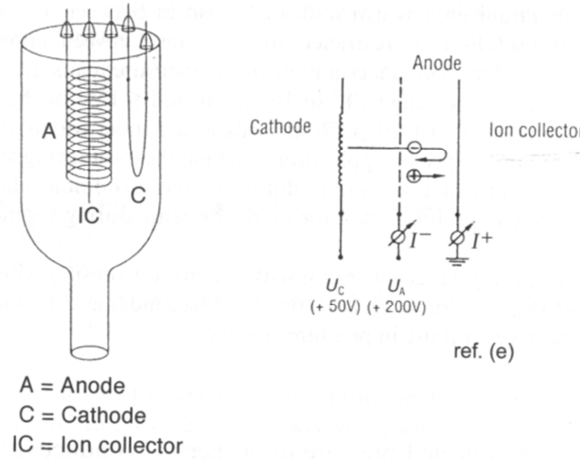
Figure 14 – Schematic view of a hot cathode ionisation gauge.

The amount of ionising collisions ΔN^-, and thus the number of positive ions ΔN^+, is equal to:

$$\Delta N^- = N^- \cdot n \cdot \sigma \cdot l$$

where N^- is the number of electrons going from cathode to anode, l is the distance between the two electrodes, n is the gas particle number density and σ is the collision cross-section, which depends on the type of gas.

An ion collector attracts the ions; the ion current I^+ is equal to:

$$I^+ = \frac{\Delta N^+}{t} = \frac{N^-}{t} \cdot n \cdot \sigma \cdot l = I^- \cdot n \cdot \sigma \cdot l$$

Since:

$$P = n k_B T$$

by measuring the ion current it is possible to obtain the pressure:

$$I^+ = I^- \cdot \frac{\sigma l}{k_B T} \cdot P = I^- K P$$

where K is the same constant already mentioned for cold cathode ionisation gauges and depends on the type of gas and the gauge geometry. The sensitivity S of the hot cathode ionisation gauge is equal to $I^- K$ instead.

Table 5 – Correction factors γ for different gases [5].

Gas	Kr	CO_2	CH_4	Ar	CO	N_2, air	H_2	He
Correction factor γ	0.59	0.69	$0.7 - 0.8$	0.83	$0.92 - 0.95$	1	2.4	$6.9 - 7.1$

As for cold cathode ionisation gauges, I^+ and the measured pressure depend on the type of gas because the collision cross-section σ takes into account that, for the same electron energy, it is easier to ionise some gases than others (Figure 15): the gauges are thus calibrated using N_2 as reference gas and a correction factor γ (Table 5) has to be applied if the actual pressure for a different gas is needed:

$$P_{actual} = P_{measured} \cdot \gamma$$

The higher is the ionisation cross section, the higher will be the correction factor γ.

Hot cathode ionisation gauges can be influenced by two effects, namely X-ray effect and gas-ion desorption.
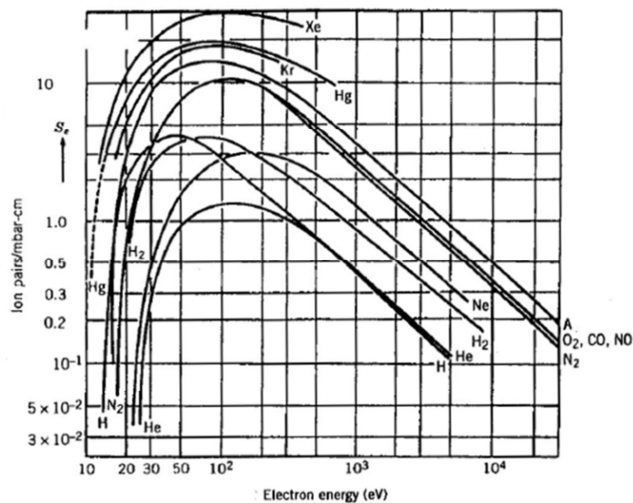
Figure 15 – Ionisation cross section as a function of the electron energy.

This latter effect is due to the initial electric discharge, which is responsible for the desorption of gas molecules from the anode surface; these molecules are ionised in the impact and can afterward reach the collector, leading to an initially increased measured pressure.

The electron impact on the anode also generates the emission of X-rays, which in turn cause a photoelectron effect on the collector. The measured pressure is therefore higher than the actual one because:

$$P_{measured} = \frac{I^+ + I_r}{S}$$

where I_r is the photoelectron current; because of this X-ray limit, such gauges could only read pressures down to 10^{-7} *mbar*.

In order to face this problem, Bayard and Alpert developed a gauge in which the collector surface area is significantly reduced, leading to a strong decrease of I_r: the collector is a thin wire surrounded by a cylindrical and coaxial open anode.

This improvement led to a significant reduction of the minimum readable pressure by means of a hot cathode gauge: the lowest pressure that can be measured by a Bayard-Alpert gauge is of the order of 10^{-12} *mbar* and it is again limited by X-ray effects.

The search for a method of measuring lower pressures led to the development of the so-called extractor gauge. In this device the ion collector is removed from sight of the grid. A simple lens is introduced between the grid and the collector to remove the ions to the collector. An ion reflector is used to reflect the ions onto the collector tip, thus increasing the sensitivity to that of a conventional BA gauge. An extractor gauge is able to measure pressures down to about 10^{-12} *mbar*.

4.2 PARTIAL PRESSURE MEASUREMENTS

Residual gas analysis allows the identification and quantification of the gaseous components which are present in a vacuum system by ionising the different gas species that are present in the system and by calculating their ion currents. With total pressure measurements, partial pressures are needed in order to completely characterise a vacuum system. Once the ion currents have been calculated, partial pressures corresponding to each of the gas species can be easily determined.

Residual Gas Analysers (RGA) are based on quadrupole mass spectrometers and they are made up of three parts:

- − an ion source;
- − a mass-to-charge ratio filter, i.e. a quadrupole separation system;
- − an ion detector.

The ion source ionises the gas atoms contained in the vacuum system, generating an ion beam which goes to the mass separation system. Here continuous changes in the voltage applied to the electrodes of the quadrupole allow the selection of ions with a well-defined mass over

charge ratio (*M/Z*): only these ions are able to pass the mass filter and can finally reach the detector, where the ion currents I^+ associated with each value of *M/Z* are measured. The output is a spectrum which correlates the amplitude of the signal, i.e. the ion current, with *M/Z*; the normal mass range of a RGA is comprised between *1 amu* and *100 amu*.

Partial pressure related to a given value of *M/Z* can be calculated by means of the following relationship:

$$S_{RGA,M/Z} = \frac{I^+_{M/Z}}{P_{M/Z}}$$

where $S_{RGA,M/Z}$ is the sensitivity of the RGA expressed in *[A/mbar]* for a given *M/Z* ratio. Each RGA has its own sensitivity for each *M/Z* value and therefore a calibration of the device is needed before starting measurements.

Gas atoms and molecules generate fragments as they are ionised; each fragment is characterised by a different *M/Z* value and the partial pressure associated to a given gas should therefore take into account the contribution of everyone of its fragments.

Different cracking patterns can be obtained for the same gas molecules, depending on the RGA geometry and the ionising electron energy; an example is reported in Table 6.

Table 6 – Cracking pattern of water vapour (ionising electron energy equal to 102 eV) [5].

Ion	*M/Z*	% of the major peak	*f*
H_2O^+	18	100	0.74
OH^+	17	25	0.185
O^+	16	2	0.015
H_2^+	2	2	0.015
H^+	1	6	0.044
TOT		**135**	**99.9**

Once the fragment distribution pattern related to a certain gas has been found, partial pressure can be calculated in two different ways:

- all the mass fragments M_i associated with the gas of interest are taken into account and the sum of all the associated ion currents is used to calculate the gas partial pressure P_G:

$$P_G = \frac{\sum_i I^+_{M_i}}{S_{RGA,G}} = \frac{I^+_{TOT,G}}{S_{RGA,G}}$$

– one mass fragment M_G is selected and its corresponding ion current is measured; P_G is then obtained by considering the fragmentation factor f of M_G, which corresponds to the part of the gas total spectrum represented by the peak associated with M_G (Table 6):

$$P_G = \frac{I^+_{M_G}}{S_{RGA,G} \cdot f_{M_G}}$$

The selected mass M_G should obviously be related only to the gas of interest and not to others, otherwise the measurement would be altered and pressure overestimated.

The relative amount of each gas is not reproduced in the output of ions generated by the ion source: for this reason, a reference gas, which usually corresponds to N_2, should be used in order to determine the gauge sensitivity and to introduce appropriate correction factors.

The reference sensitivity for N_2, S_{N_2}, is calculated by following one of the above-mentioned methods; the gauge sensitivity S_G for any other gas can be subsequently obtained by means of the following equation:

$$S_G = S_{N_2} \cdot \vartheta_G$$

where ϑ_G is the ionisation probability of G with respect to N_2; values of ϑ_G for several gases of interest are reported in Table 7.

Table 7 – Ionisation probabilities for different gases relatively to N_2 (electron energy equal to 102 eV) [5].

Gas	He	Ne	H$_2$	N$_2$	O$_2$	CO	Ar	CO$_2$	CH$_4$	C$_2$H$_6$	C$_3$H$_8$	H$_2$O
ϑ_G	0.14	0.23	0.44	1.0	1.0	1.05	1.2	1.4	1.6	2.6	3.7	11.0

5. GETTERS

A getter is a solid material able to form stable bonds with chemically-active gas molecules on its surface by chemisorption; it can be considered as a chemical pump and it can be used for different purposes and applications concerning ultra-high vacuum (UHV), i.e. pressures ranging from 10^{-7} *mbar* to 10^{-12} *mbar*.

The molecular absorption on a given surface can be considered stable if the mean sojourn time τ of the molecule on the surface is large enough in comparison with the duration of the experiment; according to Frenkel's law, the mean sojourn time is defined as follows:

$$\tau = \tau_0 \cdot e^{\frac{E}{RT}}$$

where τ_0 is the vibrational period of the absorbed molecule (it can be considered of the order of magnitude of 10^{-13} *s*, without any influence from the nature of the absorbed molecule and of the surface), T is the temperature, E is the binding energy and $R=8,314$ $J \cdot K^{-1} \cdot mol^{-1}$ is the universal gas constant.

The stability of a bond between atoms or molecules depends on the amount of energy that is necessary to break it: the higher is the binding energy, the more stable is the bond.

Physisorption implies weak interactions between molecules, like van der Waals forces, with binding energies generally lower than *50 kJ·mol^{-1}*.

Chemisorption instead implies a chemical reaction and the formation of stronger covalent, ionic or metallic bonds between gas molecules and the absorbing surface, with binding energies even much higher than *50 kJ·mol^{-1}*; this is the reason why chemisorption can give as a result stable bonds also at room temperature, whereas with physisorption this is possible only at very low temperatures, because otherwise the only thermal excitation of the molecules would be sufficient to break the bond.

Therefore, chemisorption, unlike physisorption, does not need to cool down the getter at cryogenic temperatures and allows to create and to maintain UHV conditions in a system even at room temperature for a prolonged time, ranging from some minutes even to some months or years (the latter case is typical for applications in accelerating facilities, like the LHC concerning the present study).

The need to form a stable chemical bond in order to have chemisorption explains why getters are not able to pump noble gases (He, Ne, Ar, Kr, Xe, Rn), which are inert and therefore cannot react with the material.

To be able to perform absorption on its surface, a getter should have an active surface layer with free sites available to form bonds with gas molecules; by absorbing particles on its surface the number of vacant sites decreases, until a reactivation of the material becomes necessary.

Getters can be of two types, according to the method followed to achieve their activation:

- *evaporable getters* are obtained by under vacuum sublimation and deposition of a fresh getter film on a metallic surface;
- the active surface of a *non-evaporable getter* (NEG) is obtained by thermal diffusion of the surface oxide layer, which contains absorbed gas molecules, into the bulk of the material itself.

The employment of NEG alloys in vacuum technology and particle accelerators facilities is the main topic of this thesis work.

5.1 A BRIEF HISTORY OF NEG EMPLOYMENT FOR PARTICLE ACCELERATORS VACUUM SYSTEMS

The main obstacle to the achievement and maintaining of UHV conditions in a vacuum system is represented by the outgassing of the vacuum chamber walls.

Even properly selected and treated metal surfaces show significant desorption rates, in particular for H_2, whose typical values are of the order of *10^{-13} mbar·l·s^{-1}·cm^{-1}* [13]. The outgassing of other species like CH_4, CO and CO_2 is about two orders of magnitude smaller.

In order to ensure the good functioning of a particle accelerator and an appropriate beam life time, lowest possible pressure is needed; for compact vacuum systems, like all the accelerators and storage rings built until the 1970s, this pressure range was easily obtained by installing on the vacuum chamber an appropriate number of pumps.

The need for an increased beam intensity however led to the progressive reduction of vacuum chambers aperture and to the increasing in their length; under these conditions, traditional pumping systems became less efficient due to the chamber's lowered conductance, which reduces significantly the effective pumping speed of the installed pumps.

In this case, it is possible to ensure the same ultimate pressure values only by applying a linearly distributed pumping. The Large Electron-Positron Collider (LEP), which started operating at CERN in 1989, was the first machine adopting extensively this solution: pumping along about *23 km* (over a total circumference of *27 km*) of LEP was provided by sputter-ion pumps and by a *30 mm* wide constantan strips (Figure 16) coated on both sides with a *100 μm* thick layer of non-evaporable getter, namely a Zr-Al alloy produced by SAES-Getters under the trade name of St 101 [14].
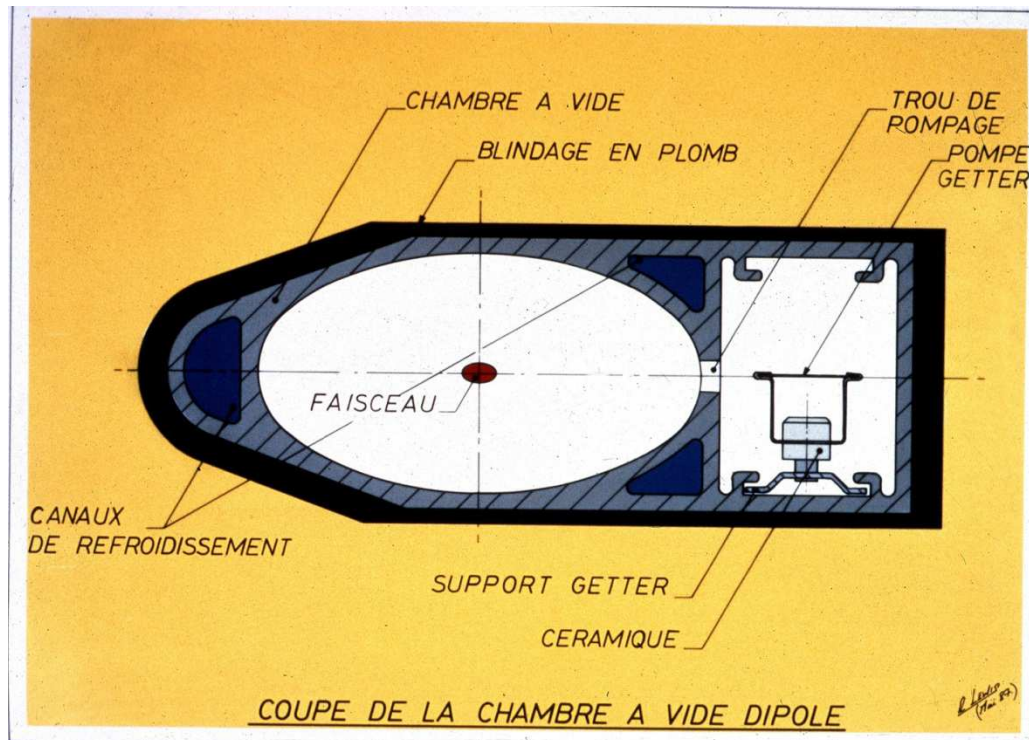
Figure 16 – LEP vacuum chamber cross-section (courtesy CERN).

These strips were vacuum activated at *750 °C*, in order to enhance diffusive processes, by directly applying a current of *90 A* for about half an hour [13]; this required an electrical insulation for the strips, substantially limiting their employment and thus the maximum achievable pumping speed and the ultimate pressure.

The development of new NEG alloys (like the St 707 always from SAES-Getters) needing an activation temperature of about *400 °C* for about 1 hour made possible a passively activation of the layer during the usual bake out of the vacuum system.

Since in this case electrical insulation was no more required, it was possible to install a much larger amount of NEG strips, for example by wrapping them on stainless steel inserts placed inside the vacuum chamber.

The natural evolution of this process was an improvement in pumping efficiency, obtained by decreasing the distance of the linear pumps from the walls; meanwhile the need for a reduced outgassing finally introduced the idea of vacuum chambers coated with NEG thin films, whose study started at CERN in 1995 in conjunction with the development and design of the new Large Hadron Collider.

5.2   CHARACTERISTICS AND SELECTION OF A NEG MATERIAL

The gas chemisorption mechanism of a NEG material is a three-step process:
1. dissociation of gas molecules at the gas-surface interface;
2. sorption of gas molecules at the superficial free sites;
3. dissolution of the absorbed molecules into the bulk through diffusion mechanisms.

H_2 is the only gas pumped by NEG whose sorption is thermally reversible [15]; the dissociation pressure of hydrogen, describing the equilibrium between the desorbing flux of molecules from the getter and the pumping flux inside the material, is definable according to Sievert's law:

$$P_{H_2} = A \cdot c^2 \cdot e^{\Delta H/kT}$$

where c is the concentration of the solid solution of monoatomic dissociated hydrogen, T is the temperature of the getter, ΔH is the dissociation enthalpy and A is a parameter including the entropic contribution of the reaction; the dissociation pressure of a NEG material has to be as low as possible in order to be compatible with operations in UHV.

Except for H_2, gas molecules are chemically adsorbed on the getter surface and they do not diffuse at ambient temperature inside the material bulk.

As the adsorption goes on, a passivating oxide layer is formed on the surface of the material, leading to a decrease of the NEG pumping properties; in order to reactivate the material, this layer must be dissolved by diffusing the surface oxygen into the bulk.

The vacuum activation of NEG coatings requires heating the system in which the getter is installed up to a so called *activation temperature*; if this temperature is compatible with the bakeout temperature of the chamber where the NEG is inserted, the getter can be passively activated during bakeout. High oxygen diffusivity is thus required to dissolve the surface passivation layer even at low temperatures.

Furthermore, since the sorption of gases other than hydrogen is not reversible, solubility limit has to be taken into account: the solubility limit is defined as the maximum concentration up

41

to which a solid solution is thermodynamically stable; when this concentration is exceeded, a secondary phase tends to nucleate and precipitate, damaging the getter: in order to avoid this, NEG materials must be characterised by a high solubility limit, so that the accumulation of a large amount of gas pumped molecules, due to many activation-air venting cycles, becomes possible.

Under the assumption that the thickness of the oxide layer formed during air exposure is equal to *2-3 nm*, a solubility limit of at least *10%* is needed in order to guarantee an acceptable life time to a *1 μm* thick NEG film [13].

A getter material should also provide large enthalpies of absorption for all the gases that are usually present in a UHV vacuum system, i.e. H_2, CO, CO_2 and N_2.

In addition, there are also some other important characteristics that a good NEG material should have, namely a good adhesion of the film to the substrate, a high mechanical resistance and a high melting point. It must be also non-toxic, non-pyrophoric and non-magnetic, in order to be used in particle accelerators; for the same reason, low secondary electron yield is required.

Finally, the cost of the material is another important feature that cannot be neglected.

Taking into account all these requirements, among several elements providing good gettering properties, the transition metals of the 4th group of the periodic table (Ti, Zr, Hf) best fulfil the most restrictive condition, i.e. a high solubility limit for oxygen, which is larger than *10%* for these elements only.

Therefore, these metals and their binary combinations became initially object of the research on NEG materials: as already said, the first NEG strips installed in the LEP were two alloys produced by Saes-Getters, i.e. St101 ($Zr_{84}Al_{16}$, content in weight) and St707 ($Zr_{70}V_{24.6}Fe_{5.4}$); linear pumps made of these gettering ribbons were developed and studied at CERN [16] [17].

The properties of the binary quasi-equiatomic alloy TiZr, which shows the lowest activation temperature (*250 °C* for 24 hours baking) among these combinations, were also deeply investigated [9].

However, elements of the 5th group of the periodic table (V, Nb, Ta), although providing a lower oxygen solubility limit, show much higher oxygen diffusivities [13]; ternary combinations of metals of the 4th and 5th groups were therefore afterwards studied.

In particular, it was found that the ternary alloy TiZrV becomes fully activated after 24 hours heating at *180 °C* (Table 8).

Table 8 – Activation temperature evolution of the main NEG alloys.

Getter	$T_{ACTIVATION}$ [°C] for 24 h heating
St101 $Zr_{84}Al_{16}$ (weight content)	600
St707 $Zr_{70}V_{24.6}Fe_{5.4}$ (weight content)	350
TiZr (atomic content)	250
$Ti_{30}Zr_{30}V_{40}$ (atomic content)	180

Ultimate pressure measurements (Figure 18) and measurements of the variation of the H_2 sticking coefficient (Figure 17) confirmed this conclusion [14].
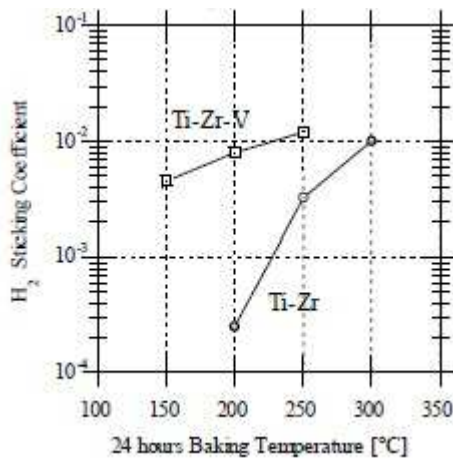
Figure 17 – Variation of the H$_2$ sticking coefficient for TiZr and TiZrV coated chambers as a function of bakeout (*24 h*) temperature [14].
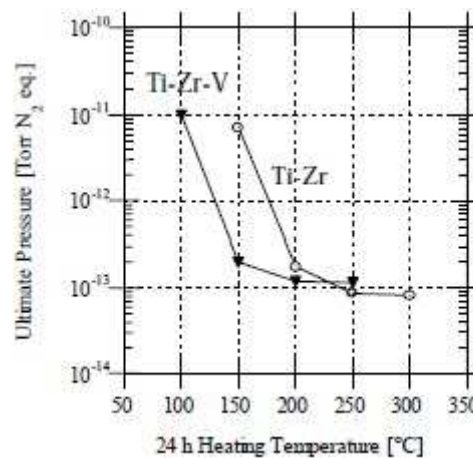
Figure 18 – Ultimate pressure after 24 h baking, without intermediate air venting, on chambers (length=*2 m*, Ø=*10 cm*) coated with TiZr and TiZrV as a function of bakeout temperature [14].

TiZrV NEG coatings were afterward produced and deposited on beam pipes installed in the Long Straight Sections of the LHC; these coatings represent the object of this thesis work and their properties will be described in the following paragraphs.

5.2.1 Thermodynamic considerations

The activation mechanism is ruled by thermodynamic laws, predicting the conditions under which the surface oxide layer of a given metal can be dissolved by forming a solid solution with the metal itself.

In order to handle with this process, the concept of free energy has to be introduced:

$$\Delta G_{ox} = \Delta H_{ox} - T \cdot \Delta S_{ox}$$

$$\Delta G_{ss} = \Delta H_{ss} - T \cdot \Delta S_{ss}$$

The first term represents the free energy of the oxide formation process, while the second concerns the formation of the solid solution; ΔH and ΔS are respectively the changes of the enthalpy and of the entropy of the two states.

This allows to know in which direction the system will evolve, taking into account that the most stable configuration is the one that minimise its free energy.

For $\Delta G_{ox} < \Delta G_{ss}$, the formation of a solid solution is thus inhibited, while $\Delta G_{ox} = \Delta G_{ss}$ means that the two phases are in equilibrium; in the latter case, the oxygen concentration in the solid solution is equal to the solubility limit.

If otherwise $\Delta G_{ox} > \Delta G_{ss}$, the inequality becomes:

$$\Delta H_{ox} - \Delta H_{ss} > -T \cdot (\Delta S_{ss} - \Delta S_{ox})$$

and the entropic term is always negative. In this case the dissolution of the oxide layer is allowed but there are three different possibilities, depending on the enthalpies and entropies of the considered material (Table 9).

In the first case:

$$|\Delta H_{ss}| > |\Delta H_{ox}|$$

this means that the inequality is always true and thus the dissolution of the oxide film is thermodynamically allowed, regardless of the temperature, until the solubility limit is reached; this is the case of the elements of the 4th group of the periodic table (Ti, Zr, V).

When otherwise:

$$|\Delta H_{ss}| < |\Delta H_{ox}|$$

both terms of the inequality are negative: the entropic part becomes thus a decisive factor.

Table 9 – Energy of dissolution of oxygen in pure metals compared to the heat of formation of the stable oxide containing the lowest number of oxygen atoms per atom of metal [18].

	Metal - oxide	ΔH_{ox} per O atom [kJ/mol]	ΔH_{ss} [kJ/mol]
4th group	Ti – TiO	−542.9	−560.67
	Zr – ZrO$_2$	−550.65	−619.23
	Hf – HfO$_2$	−556.9	−552.29
5th group	V – VO	−432.0	−422.15
	Nb – NbO	−419.8	−383.85
	Ta – Ta$_2$O$_5$	−409.5	−385.96
6th group	Cr – Cr$_2$O$_3$	−376.8	−221.97

For some elements (V, Nb, Ta), the inequality is valid only over a given temperature threshold; for most of the other elements instead, the difference between the enthalpies is too large and the entropic term cannot compensate it, even at very high temperature.

In this latter case, dissolution of the surface oxide layer into the bulk is inhibited.

5.2.2 Diffusivity and solubility limit as functions of the crystalline structure of the getter alloying elements

Thermodynamic laws determine under which conditions a chemical reaction can occur or not; in addition however, also kinetic aspects should be taken into account.

Concerning the activation of a NEG coating, these kinetic aspects are related to the diffusivity and solubility limit of the considered material.

Table 10 – Diffusion length of oxygen for elements of the 4th and 5th groups for *2 h* heating at *300 °C* [18].

	4th group			5th group		
Element	Ti	Zr	Hf	V	Nb	Ta
Oxygen diffusion length [nm]	0.4	0.9	0.1	300	650	800

Numerical values of diffusion length and solubility limit of oxygen at *300 °C* for different metals are reported in Table 10 and Table 11, respectively. It should be noted that these

values are valid in the case of single crystals; for polycrystalline structures, both diffusivity and solubility limit increase.

Table 11 – Solubility limit of oxygen for elements of the 4th and 5th groups at 300 °C [18].

	4th group			5th group		
Element	Ti	Zr	Hf	V	Nb	Ta
Oxygen solubility limit [at.%]	33%	29%	17%	4%	0.01%	0.4%

Metals belonging to the 4th group of the periodic table are characterised by hexagonal close-packed (hcp) crystalline structure, whereas metals of the 5th group have a body-centred cubic (bcc) structure.

These data thus clearly show that bcc crystalline structures have higher diffusivities than the hexagonal close-packed ones, which in turn have higher solubility limits, i.e. higher storage capacities, than bcc ones.

a)

b)
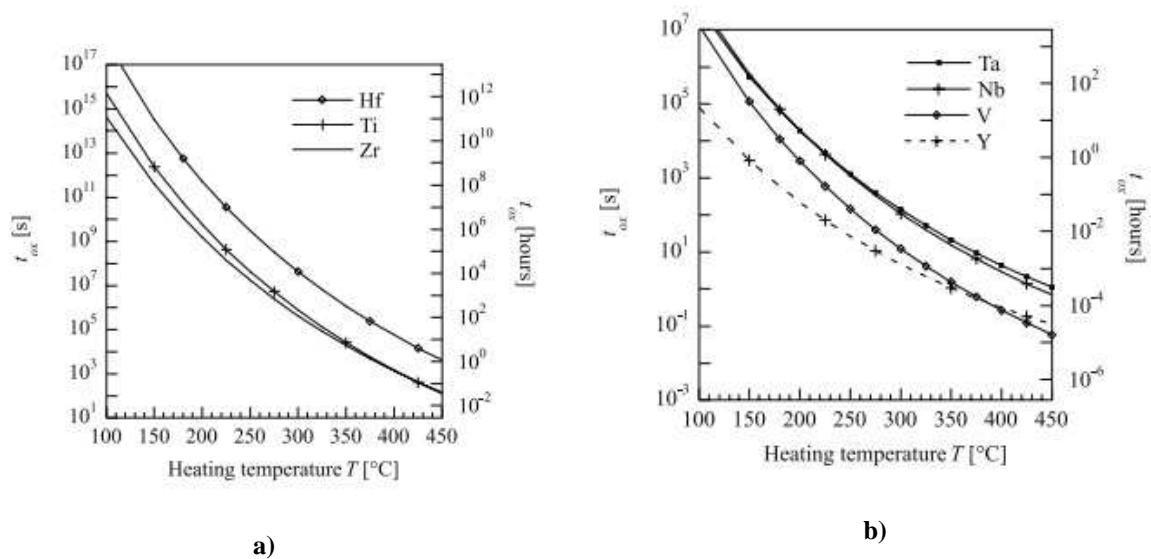
Figure 19 – Activation time as a function of heating temperature for metals of the a) 4th group and b) 5th group [18].

A higher diffusivity means that, for the same heating temperature, a shorter activation time is needed; according to the above-mentioned considerations, metals belonging to the 5th group get activated faster than those of the 4th group (Figure 19).

Diffusion lengths of different elements (H, C, N, O) after *2 h* have been plotted as functions of the heating temperature and compared for three different metals (Ti, Zr, V) [18]; the results show that diffusion is faster for H than for C and O, while the slowest is for N (Figure 20).

a)

b)

c)
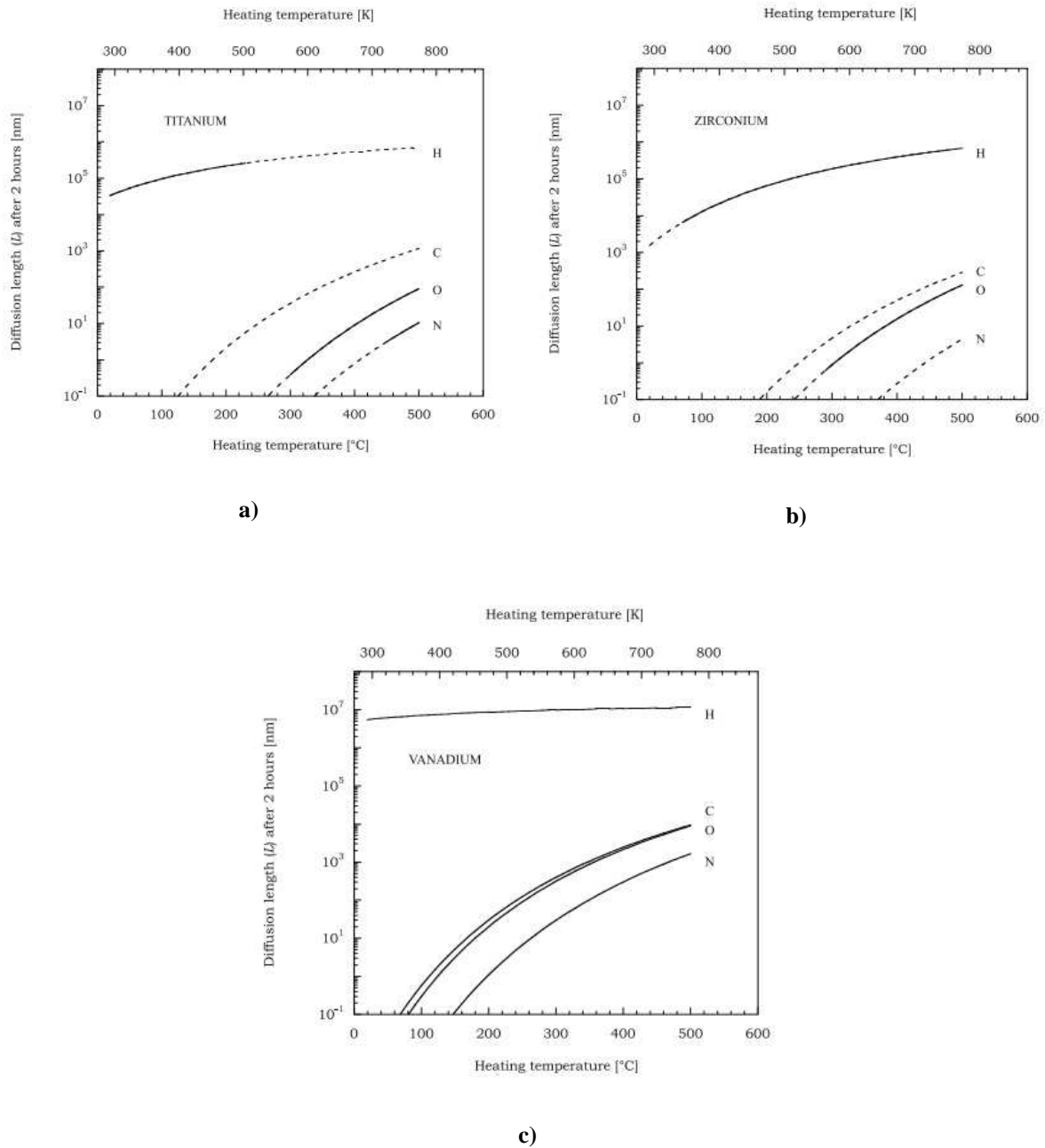
Figure 20 – Diffusion length after 2 hours for H, C, O, N as a function of heating temperature in: a) Ti, b) Zr, c) V. Plots are realised on the basis of diffusion data; extrapolated data are in dashed lines [18].

5.3 VACUUM PROPERTIES OF TiZrV NEG COATINGS

5.3.1 TiZrV pumping speeds and sticking probabilities for different gases

The main parameter for the evaluation of the vacuum properties of a NEG alloy is its pumping speed for the gases that could be found in UHV systems, i.e. H_2, CO, CO_2, N_2, H_2O and O_2.

As already said, due to their adsorbing mechanism based on chemisorption, NEG coatings are not able to pump noble gases (He, Ne, Ar, Kr, Xe, Rn). Furthermore, NEG coatings provide a negligible pumping speed also for hydrocarbons, which are usually present in vacuum systems (particularly CH_4), due to their high dissociation energies at metal surfaces. However, heavy hydrocarbons can be adsorbed at the surface of a getter at room temperature by physisorption [6].

NEG pumping speeds are often reported in terms of sticking probability α, which is comprised in the range $0 \leq \alpha \leq 1$ and is defined as the probability for a particle to be adsorbed by a surface per individual collision with it [19]. The pumping speed S of a NEG surface A, characterised by a sticking probability α, can be expressed as:

$$S = \alpha A \frac{c}{4}$$

where $c/4$ is the mean molecular velocity of the gas [20].

Pumping speed for gas molecules at the entrance of a NEG-coated chamber can also be described by the conductance of the chamber's aperture multiplied by a pumping probability $\%CP$, also referred to as capture probability, which depends on the sticking factor:

$$S = C_{AP} \cdot \%CP$$
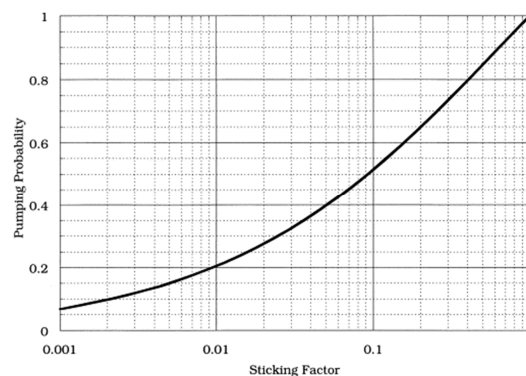
Figure 21 – Variation of the capture probability for H_2 as a function of the sticking factor; these data are valid only for chambers with *L/r>20* [21].

The relationship between capture probability and sticking factor (Figure 21) is influenced by the geometry of the chamber, namely by the ratio of its length and aperture radius (L/r).

	H_2	CO	N_2
Smooth NEG surface	$8 \cdot 10^{-3}$	0.7	$1.5 \cdot 10^{-2}$
Rough NEG surface	$3 \cdot 10^{-2}$	0.9	$3 \cdot 10^{-2}$

Table 12 reports some values of the maximum sticking factors of H_2, CO and N_2 on a TiZrV coating at room temperature [22]; if the surface is rough and porous, the sticking probability is enhanced due to the multiple collisions given by the impinging molecules on the surface and inside the pores.

Other measurements of the sticking factors for TiZrV NEG coatings found values ranging between $6 \cdot 10^{-3}$ and $5 \cdot 10^{-2}$ for H_2 and between 0.4 and 0.8 for CO [23], thus aligned with the values of Table 12. Sticking factor for CO_2 instead has been reported to correspond to that for CO [16].

Further measurements of H_2 sticking factor have been conducted in the framework of this thesis work and will be presented in the following chapters.

The maximum sticking factor at room temperature for CH_4 was also estimated, resulting to be equal to 10^{-6} and thus negligible with respect to active gases [22].

5.3.2 NEG pumping and saturation mechanism

A model for gas molecules pumped by a ZrAl NEG coating has been developed [16], taking into account the following assumptions:

 – molecules are adsorbed as a whole onto defined adsorption sites;
 – each site may accommodate only one molecule
 – the adsorption on one site is independent of the presence of other molecules on neighbouring sites;
 – no desorption takes place.

These are valid for all the gases pumped by NEG with the exception of H_2, which is not chemisorbed and can diffuse also at room temperature.

For a flat surface, according to Langmuir's adsorption isotherm, it is possible to assume that:

$$S = S_0 \left(1 - \frac{Q}{Q_0}\right)$$

where S_0 is the initial pumping speed and Q_0 is the gas quantity needed to full saturate the NEG. This equation, if $S(Q)$ is plotted linearly, represents a straight line intersecting the vertical axis at $S=S_0$ and the horizontal one at $Q=Q_0$.

Experimental measurements however show that, in proximity of Q_0, the lower part of the curve is not straight but is bended and decreases more slowly (Figure 22).
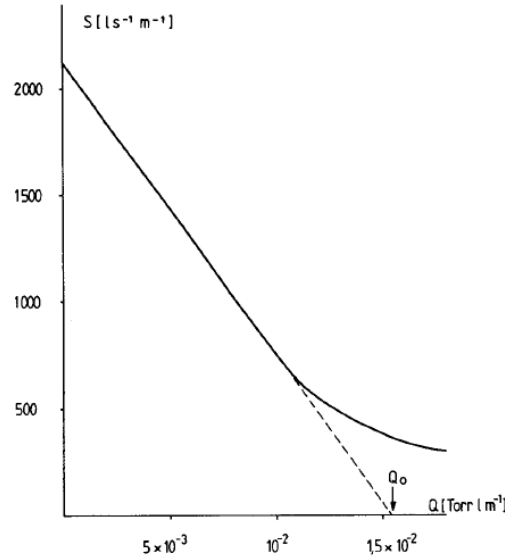
Figure 22 – Linear plot of CO pumping speed per unit length as a function of the gas sorbed quantity [16].

The origin of this mismatch between the model and the real behaviour of the NEG coating has to be found in the surface roughness and porosity of the film; a new model, which takes into account the adsorption inside the pores, has thus been developed.

In order to simplify the formulation, the outer surface of the NEG coating has been assumed perfectly flat. In addition, the irregular pattern of voids distributed in the material's volume is represented by a certain number of cylindrical voids, whose aperture's diameter is fixed and whose length is equal to the film's thickness. The density of surface adsorption sites is the same for both the outer and inner surfaces and it has been obtained by extrapolating the first part of the curve in Figure 22.

Under these assumptions, the saturation process of NEG is the following: at the beginning gas molecules are absorbed either on the outer flat surface or inside the voids. When a certain amount of gas have been pumped, the adsorption goes on essentially only inside the voids and therefore pumping speed becomes limited by the conductance of the void's length that

50

molecules must cover in order to find still free adsorption sites. In this part of the curve the dependence $S(Q)$ is the following:

$$S \propto Q^{-1}$$

due to the fact that the conductance is inversely proportional to the void's length. In a logarithmic plot, this dependence describes a pumping speed decreasing following a straight line with an angular coefficient equal to *-1*; only in the final part of the curve, when complete saturation is reached, pumping speed decreases more rapidly.

It is thus assumed that the pumping speed of a NEG rough surface for a given gas is the sum of two contributions, i.e. the pumping speed of the outer flat surface S_F:

$$S_F = \alpha_F A_F C \left[1 - \frac{Q}{Q_0(1-A_V/A)}\right]$$

and the pumping speed provided by the voids' surface S_V, which depends on the type of gas and for N_2 is equal to:

$$S_V = \alpha_V n^2 A \frac{12.5D^3}{l + 1.3D}$$

where α_V and α_F are the sticking factors inside and outside the voids respectively, A_F is the area of the flat surface, C is the conductance at the aperture of the voids, Q_0 is the gas quantity needed for full saturation, A_V is the area of the aperture, n^2 is the density of voids per unit area of NEG, D is the diameter of the cylindrical voids and l is the depth until which the voids are already saturated.
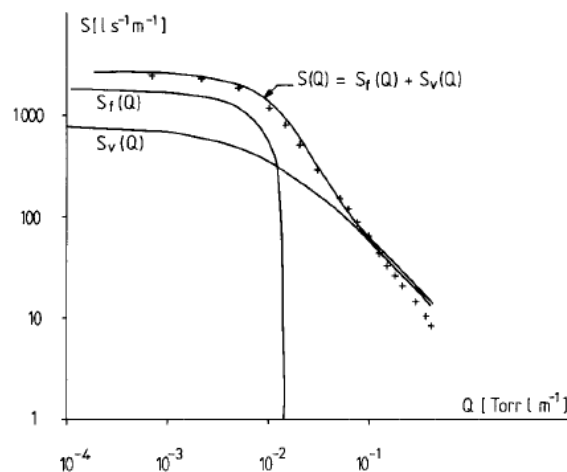
Figure 23 – Comparison between calculated and experimentally measured (+) pumping speed curves. The two contributions of outer surface and voids to the total calculated pumping speed are also showed [16].

51

Figure 23 compares calculated and experimental *S(Q)* curves for CO, showing that the above-described model fits in well with the adsorption mechanism of this gas.

However for N_2 the agreement between calculated and experimental curves is not so satisfying. This is due to the fact that polyatomic molecules usually undergo dissociation before being chemisorbed; each sorbed molecule occupies a number of adsorption sites which is at least equal to its number of atoms. CO constitutes an exception because it is characterised by single-site adsorption although being a diatomic molecule.

For polyatomic molecules, Langmuir's adsorption isotherm becomes:

$$S = S_0 \left(1 - \frac{Q}{Q_0} \right)^p$$

where *p* corresponds to the number of free sites close to each other needed for the adsorption of one molecule; in this case, the adsorption probability is thus reduced with respect to the case of single-site adsorption.

In the case of N_2 however, the best agreement is obtained assuming *p=6* (Figure 24).
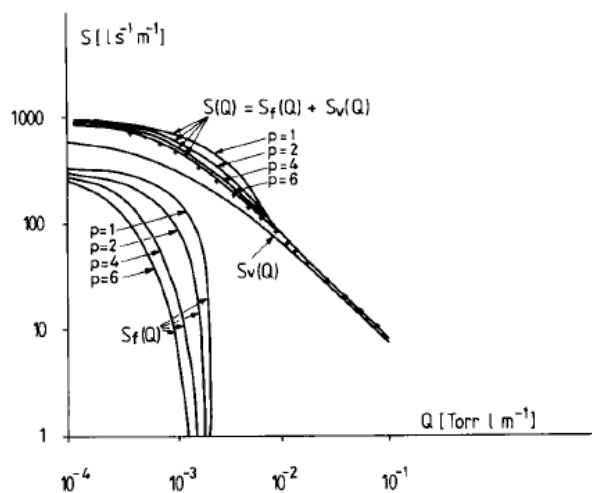
Figure 24 – Comparison of the calculated and measured (+) *S(Q)* curves for N_2, showing that the best agreement is obtained when *p=6* [16].

The lower Q_0 for N_2 with respect to CO is a consequence of the larger number of free sites needed for the adsorption of a single N_2 molecule. The lower sticking factor values for N_2 also explain why this gas leads to a faster saturation of a NEG coating.

Finally, in contrast with CO and other gases which are adsorbed by NEG, the decrease of pumping speed for H_2 as the pumped gas quantity increases is much smaller and depends on the gas injection rate. This is due to the fact that H_2 can diffuse also at room temperature, thus its pumping speed is defined by the equilibrium between two different and competing

processes, i.e. the molecular adsorption on the NEG surface and the diffusion into the NEG bulk.

Figure 25 compares pumping speed curves for CO, N_2 and H_2, which are characterised by the different behaviours and adsorption mechanisms that have been presented in this paragraph.
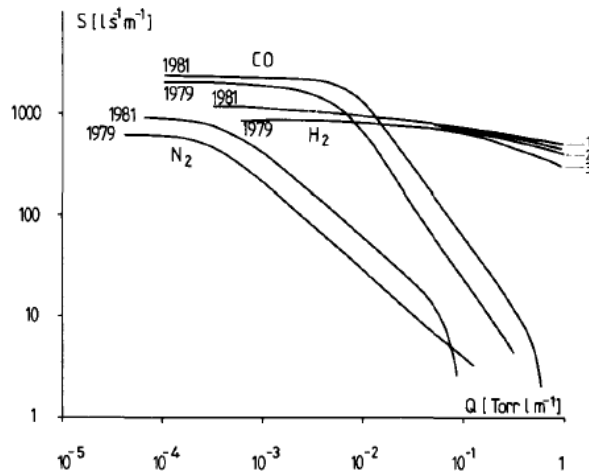
Figure 25 – *S(Q)* for CO, N_2 and H_2. 1981 and 1979 refers to two different groups of measurements. *S(Q)* for H_2 depends on the gas rate of injection: 1) $1.8 \cdot 10^{-6}$ Torr·l·s^{-1}·m^{-1}, 2) $5 \cdot 10^{-5}$ Torr·l·s^{-1}·m^{-1}, 3) $5 \cdot 10^{-4}$ Torr·l·s^{-1}·m^{-1}, 1981) $5 \cdot 10^{-4}$ Torr·l·s^{-1}·m^{-1} [16].

5.3.3 Ultimate pressure

Ideally, the ultimate pressure achievable in a NEG-coated vacuum system would be limited only by the outgassing of gas molecules that are not pumped by the NEG, namely CH_4 and Kr, which is commonly used as discharge gas in NEG deposition processes; also hydrogen dissociation pressure would play a role in the determination of the ultimate pressure.
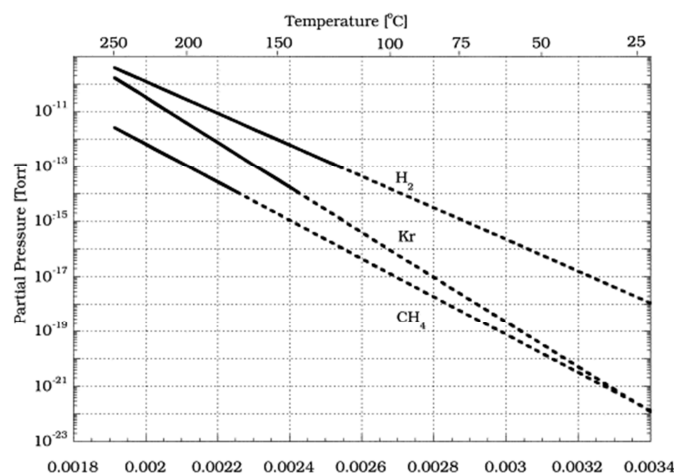
Figure 26 – **Partial pressures' evolution measured while heating an activated NEG-coated chamber (internal diameter *58 mm*) [21].**

However, it has been shown that, in real situations, ultimate pressure limitations in TiZrV NEG-coated vacuum chambers are due only to the outgassing of the gauges employed and to the NEG pumping speed available at the gauges' position [21] [22].

The degassing from the NEG-coated walls of a vacuum chamber has been calculated by measuring the variation of the partial pressures of different gases as a function of the temperature during vacuum activation and by extrapolating these so-obtained degassing curves down to room temperature (Figure 26). The result is well below the resolution of any vacuum gauge.

5.3.4 NEG desorption and secondary electron yields

As already mentioned in Chapter 2, the inner surface of high-energy particle accelerators are bombarded by electrons, photons and ions during beam operation, causing the desorption of a significant quantity of gas molecules. A lower desorption yield for a vacuum activated NEG surface becomes thus a crucial requirement for the selection of a proper NEG material.

Electron desorption yields of TiZrV coatings have been measured for H_2 and CO [22]; the result is that they are at least 10 times lower compared to those for stainless steel. Concerning CH_4, this difference is even more enhanced, i.e. at least 100 times lower. Similar results have been obtained for photon induced desorption.

Also secondary electron yield (SEY) has to be as low as possible; it can be reduced by removing the oxide layer, as in the case of induced desorption yields. At equal electron dose, the SEY of a vacuum activated TiZrV film has been found to be lower than that of traditional structural materials.

5.4 COATING PROCESS

The first NEG strips produced by SAES getters, which were installed in the LEP facilities, were made by sintering of the metallic powders of the desired alloying elements.

Nowadays, all the TiZrV NEG coated vacuum chambers for the LHC are produced by magnetron sputtering.

Sputtering is ideally suited for this application: it is simple and applicable to a wide range of materials and alloys, the stoichiometry of which it preserves. Moreover, it allows uniform and distributed coating of long, narrow vacuum chambers and can produce the desired alloys or compounds by using composite cathodes.

5.4.1 NEG deposition

The procedure for NEG deposition by magnetron sputtering on the inner surface of cylindrical vacuum chambers has been optimised through the years and several researches have been focused on this topic [22] [24].

The substrate materials are chemically treated before coating; an inadequate surface treatment leads to NEG film deterioration and, in the worst case, peel-off.
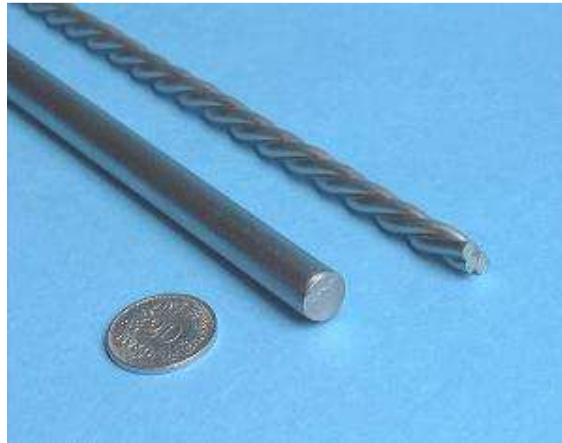
Figure 27 – Twisted metallic wires used as cathode in the NEG deposition process.

The cathode consists of a wire of the chosen metal; an alloy can be obtained by twisting together wires of different materials (Figure 27). The alloy composition can be varied by changing the number of wires for a given element and by modifying their diameters: the wider is a wire, the larger will be the percentage of material deposited in the coating coming from that wire. The deposition rate of a given material also depends on its sputtering yield: data concerning the ion-induced sputtering yields from monoatomic solids have been collected for various ion-target combinations as functions of the incident ion energy [25].
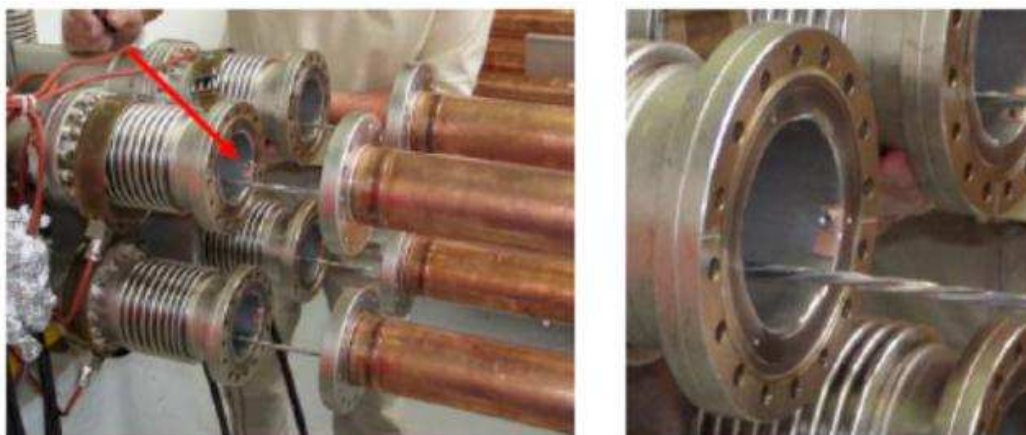
Figure 28 – Positioning of the intertwisted cathode inside the vacuum chambers to be coated.

The required magnetic field is produced by an external solenoid, coaxial to the chamber to be coated. The employment of a magnetic field allows the obtainment of higher electron ionisation efficiency with respect to normal sputtering, due to the fact that the electron path is made longer by the applied magnetic field.

The adopted magnetron sputtering configuration allows the discharge gas pressure to be reduced and consequently to limit the energy loss undergone by the sputtered atoms via gas scattering. Since excessive energy loss may endanger film adhesion, this configuration is mandatory whenever the cathode to wall distance is large (*>5 cm*). On the other hand, the magnetron configuration is also necessary if tubes of very small diameter (*≤20 mm*) have to be coated, because in this case the applied magnetic field is needed to increase the ionising path of the electrons and sustain the sputtering discharge.

A noble gas is employed as discharge gas: krypton is preferred to argon because it is less prone to be trapped into the film during the deposition process and thus its subsequent degassing is lower [26]. This is due to the fact that Kr has an atomic weight higher than the cathode material's one. Furthermore, following the Ar signal allows air leaks possibly appearing during coating to be immediately detected.

Film properties, as for instance the coating surface roughness, strongly depend on coating parameters, i.e. magnetic field, cathode voltage and discharge gas pressure. Ion current density varies depending on the cathode wire's diameter. The geometry and dimensions of the sample to be coated are also very important, as well as its temperature during the deposition process: the higher is the temperature of the sample during deposition, the larger will be the resulting film surface roughness, leading to increased pumping performances but also to an accelerated ageing.

However, full process optimisation provides results valid for a given material only and it is a time consuming activity. Benvenuti *et al.* [27] reported the following values for the non-optimised coating process of the internal walls of *50 cm* long cylindrical stainless steel samples, with an internal diameter equal to *10 cm*: a magnetic field of *~100 G*, a cathode voltage of *–500 V* (sample at ground potential) and a discharge gas pressure equal to $2 \cdot 10^{-2}$ *Torr*. During deposition the cathode, consisting of a *1 mm* thick wire of the chosen material, reached a temperature of *~1300 °C* and the sample was kept at *100 °C*; the obtained deposition rates were of the order of *1 Å/s*, with a final film thickness of about *1.5 μm*.

5.4.2 NEG characterisation

During NEG activation under UHV conditions, the oxygen surface content is progressively reduced and surface pumping is restored. Therefore both surface elemental analysis by means of Auger spectroscopy and pumping speed measurements are adequate solutions for monitoring the activation process [27].

Secondary electron microscopy (SEM) and X-ray diffraction (XRD) may also be exploited for the evaluation of NEG morphology and crystalline structure, respectively. The composition of the coating instead can be estimated by X-ray photoelectron spectroscopy (XPS) and energy dispersive X-ray (EDX) analyses.

5.5 VACUUM ACTIVATION OF NEG COATINGS

When exposed to air, NEG surfaces become saturated and lose their pumping capability. Therefore after having been installed in a vacuum system, NEG coated components must be vacuum activated, in order to create a surface layer able to adsorb gas molecules and to ensure UHV conditions during operation.

This process is also needed in order to restore the pumping properties of previously activated NEG coatings that have been subsequently partially or totally saturated by residual gases in vacuum systems.

The activation is obtained by keeping the NEG coated components at an appropriate temperature for a given time and it is usually performed in combination with the bakeout of the vacuum system.

Vacuum activation allows the adsorbed gas molecules to diffuse from a NEG surface into the bulk, leading to the generation of new free surface adsorbing sites. The increased temperature dissolves the oxide layer that was formed at the NEG surface and restores the pumping properties of the material. The activation temperature T_a is the lowest temperature at which a NEG has to be heated to become fully activated and depends on the NEG alloy to be activated and on the duration of the activation process. After having been vacuum activated, a NEG coating guarantees also low desorption and secondary electron yields.

TiZrV NEG coatings employed in the room temperature vacuum sectors of the LHC become fully activated at relatively low temperatures, allowing to use copper vacuum chambers for the beam pipes.

The bakeout and vacuum activation process commonly adopted for the NEG coated beam pipes of the LHC is shown in Figure 29. Heating jackets, collars and tapes are used to provide the heating, depending on the component's shape and on temperature requirements. A programmable bakeout controller regulates the heating parameters for each heater, i.e. heating rate in *[°C/h]*, maximum temperature in *[°C]* and duration of the temperature plateau in *[h]*.
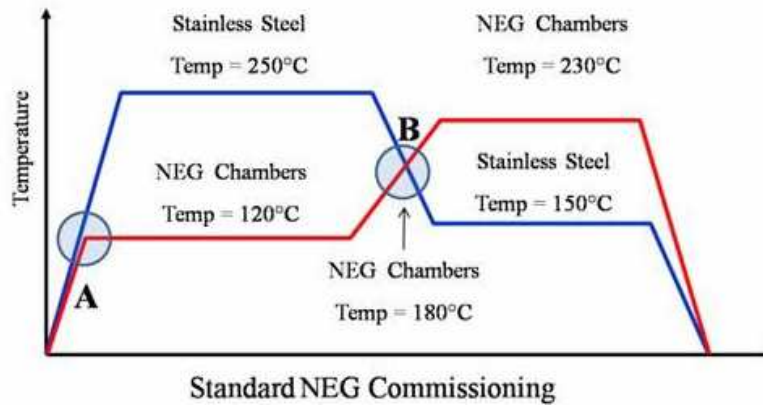
Figure 29 – Bakeout and vacuum activation cycle of the TiZrV NEG coated beam pipes [2].

During the first part of the process, all the uncoated components (stainless steel bellows and instrumentation) are baked for *24 h* at *250 °C* and *350 °C*, respectively. During this step, the NEG coated vacuum chambers are kept at *120 °C*, in order to avoid the adsorption of water coming from the degassing of the other components. The pressure rise reach a maximum when the NEG coating is at 120 °C and it is dominated by the thermal outgassing of the NEG coated chambers, while the contribution of the other components is negligible (Figure 30.a).

a)   b)
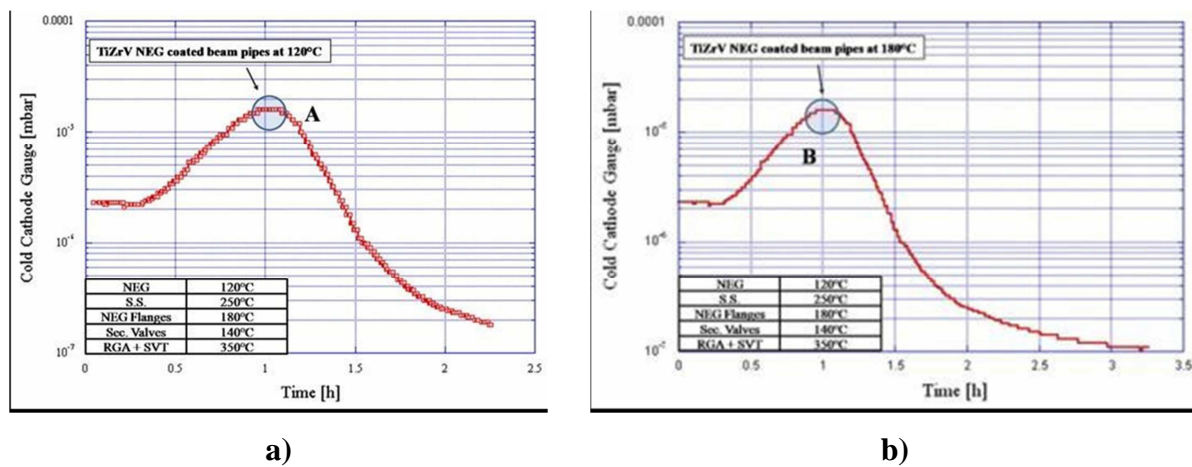
Figure 30 – Pressure variations during: a) bakeout; b) NEG vacuum activation [2].

The second part of the process instead leads to the vacuum activation of the TiZrV coating: this is made possible by heating the NEG coated vacuum chambers and by keeping them at *230 °C* for *24 h*. The non-coated bellows and the instrumentation instead are cooled and kept at *150 °C* and *180 °C*, respectively.

Pressure is still dominated by the outgassing of the NEG coating and increases until temperature reaches *180 °C*. Afterward pressure starts to decrease because the NEG starts to be activated, thus becoming able to pump the residual gas (Figure 30.b).

The NEG coating should be activated at *230 °C* because a lower temperature could cause the formation of a non-uniform oxygen concentration profile along the thickness of the material, resulting in a faster degradation of the pumping. Moreover, a temperature higher than *200 °C* is needed to dissolve into the bulk the carbon adsorbed on the NEG surface [2].

5.6 FACTORS AFFECTING NEG PERFORMANCES

The performance of a given NEG is characterised by several factors, i.e. activation temperature, sticking probability, surface capacity and ultimate achievable pressure.

Film properties depend strongly on coating parameters.

5.6.1 NEG alloy composition

Different samples have been produced and tested in order to study the influence of the composition of TiZrV alloys on the activation temperature of the getter coating [23].

For each of them, the activation process taking place while increasing the temperature has been monitored by Auger Electron Spectroscopy (AES). The results show that coatings with a composition characterised by a relatively low Ti content exhibit the lowest activation temperatures.

Furthermore, a large range of compositions with a Ti concentration lower than about *45%* allows to obtain a nanometric grain size and a fast oxide layer dissolution during vacuum activation [22].

5.6.2 Surface roughness and film structure

Surface roughness plays an important role in the definition of the molecular sticking factor: as a matter of fact, rough surfaces have a larger surface area, resulting in a larger number of adsorption sites per unit area and thus in an increased surface gas capacity.

Moreover, pumping speed and capture probability of a rough and porous surface are enhanced due to the multiple collisions given by the impinging molecules on it and inside the surface pores.

Figure 31 shows the typical trend of TiZrV pumping speed for CO as a function of the absorbed gas quantity for two NEG coatings, one smooth and the other rough; the smooth surface provides a total pumping capacity for CO which is lower by almost two orders of magnitude.
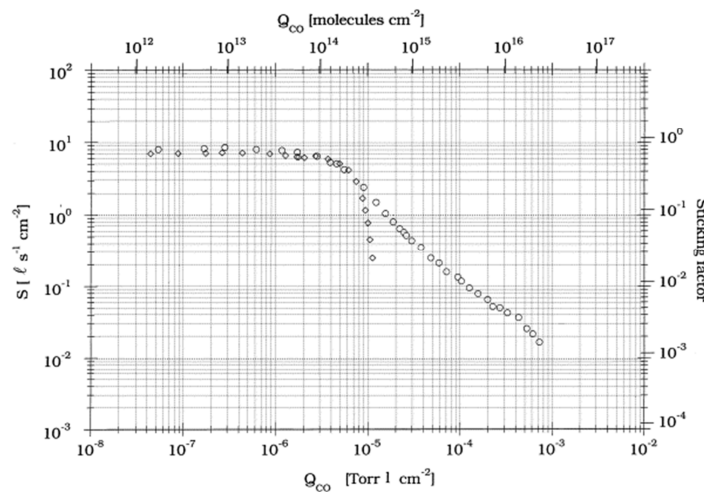
Figure 31 – Variation of pumping speed for CO as a function of the pumped quantity of gas for a TiZrV smooth film (squares) and for a very rough coating (circles) [23].

Also the film microstructure determines important variations in the characteristics of a NEG alloy: low activation temperatures are presumably caused by a large density of grain boundaries, which facilitates the diffusion of oxygen molecules from the surface into the bulk. To increase the density of grain boundaries and thus their contribution to atomic diffusion, small grain size is an advantage.

Transport along grain boundaries is enhanced also by amorphous or nanocrystal surface structures [23].

5.6.3 Bakeout and vacuum activation temperature

The influence of the bakeout and vacuum activation temperature on the ultimate pressure was measured for NEG coated chambers of different diameters [21]. The higher is the heating temperature, the lower the ultimate pressure measured in the vacuum system after *24 h* of bakeout (Figure 32).
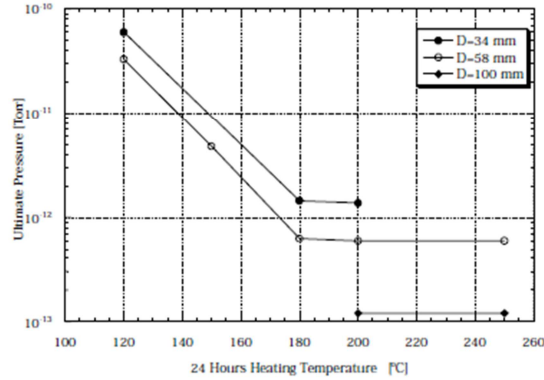
Figure 32 – Ultimate pressures measured in NEG coated chambers of different diameters after *24 h* bakeout, as functions of the heating temperature [21].

Moreover, the heating temperature influences also the pumping performances and the sticking factors for different gases of TiZrV coatings [18]. For both H2 and CO, the higher is the heating temperature, the higher the resulting sticking probability at the end of the vacuum activation of the NEG coating. However, heating at temperatures higher than *250 °C* seems to result in a slight decrease of the NEG sticking factor for CO.

5.6.4   Nature of the substrate and substrate coating temperature

The roughness of a coating may depend also on the nature of the substrate and on the sputtering parameters, namely on the substrate coating temperature.

TiZrV films have been deposited under similar conditions on different substrates giving interesting results [23]; aluminium and beryllium produced a particular TiZrV "cauliflower" structure characterized by an appreciable roughness, while stainless steel and copper led to the formation of a very smooth NEG surface (Figure 33).

Also the substrate coating temperature plays an important role in the determination of the vacuum properties of NEG coatings: a variation of this parameter during the film deposition significantly affects activation temperature, pumping speed and gas surface capacity of the material [24].

Several oxygen-free copper disks were coated at different deposition temperatures, ranging from *100 °C* to *350 °C* in steps of *50 °C*; before being coated, the samples were chemically surface treated and for all of them the same average and maximum surface roughness were obtained (respectively $R_a=0.08$ *μm* and $R_t=0.59$ *μm*). The composition of the deposited coating was the same for all the samples as well as the film thickness, that was equal to *2 μm*.

61

The evaluation of morphology and crystalline structure of the coated disks was performed by SEM and XRD analyses, respectively.
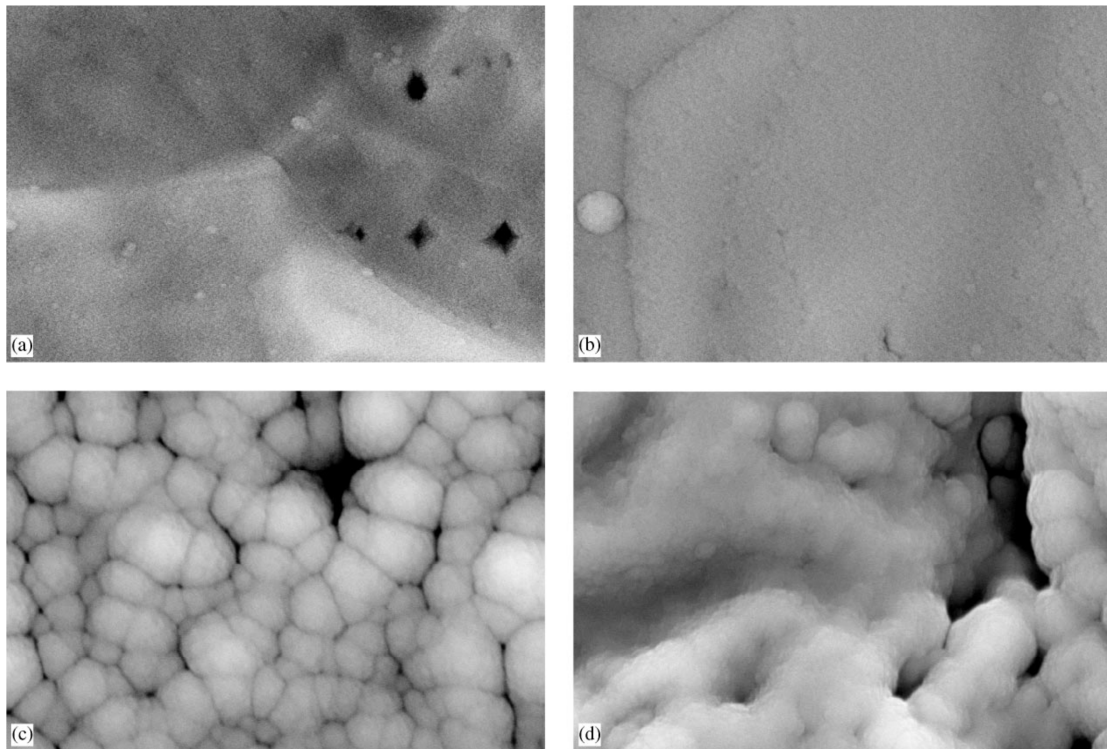
Figure 33 – Influence of the nature of the (smooth) substrate on the morfology of TiZrV coatings: a) copper, b) stainless steel, c) aluminium and d) beryllium. Pictures were obtained by scanning electron microscopy; each of them represents a sample area of *5 µm* x *3 µm* [23].

The analysis pointed out that variations of the substrate temperature strongly affect the coating morphology: up to *200 °C* the films are compact and smooth, while above this temperature it is possible to obtain a progressively more columnar and granular structure, leading to higher surface roughness and porosity and thus to an increase in surface gas capacity and sticking probability.

On the other hand, higher heating temperatures are required in order to perform the activation of samples coated at *350 °C*, while substrate coating temperatures lower than *300 °C* have a limited influence on the activation process; this could be due to the formation at temperatures equal to or higher than *350 °C* of a secondary phase characterized by a larger grain size and thus by a lower density of grain boundaries. The formation of this secondary phase, which shows a grain size of about *9-11 nm*, is highlighted by X-ray diffraction analysis and it is proved by the appearance of a corresponding peak in the spectra for films deposited at high substrate temperatures; At *T<300 °C* instead, the average grain size is less than *5 nm*.

Similar results can be obtained also using stainless steel substrates.

5.6.5 Ageing due to activation-air venting cycles

The activation of a saturated NEG-coated film is achieved by diffusing the oxygen present in the passivation layer inside the bulk of the getter material.

Due to the limited thickness of a NEG coating, this process leads to an increase of oxygen concentration inside the material and, after a certain number of activation-saturation cycles, it can give as a result a non-negligible deterioration of NEG performances in terms of pumping speed and pumping capacity.

C. Benvenuti *et al.* investigated the influence of these cycles on the NEG sticking factor for H_2 by repeatedly activating and venting a *5 μm* thick TiZrV film; the first activation was performed at *200 °C* but the activation temperature had to be progressively increased after every saturation in order to balance the gradual decrease of the sticking factor.

This study showed that after 26 cycles the film deterioration could be counteracted only by increasing the activation temperature up to *350 °C*; in this case, the H_2 sticking factor lost only *30%* of its initial value [23].

The decrease of the H_2 sticking factor thus seems to depend on the heating temperature during activation; for activation cycles performed for *24 h* at *200 °C*, the sticking probability has been found to decrease more or less as the inverse of the number of venting-activation cycles [22]. The same study showed that activations performed at *300 °C* reduce of a factor of two the H_2 sticking factor after about 30 cycles, thus substantially confirming the first above-mentioned study.

As a matter of fact, heating at lower temperatures does not allow a uniform diffusion of the absorbed oxygen atoms inside the film, leading to the formation of a concentration profile with the maximum close to the surface and thus accelerating the degradation of the NEG pumping properties due to the ageing.

Films characterized by a higher surface roughness and porosity absorb more oxygen during air venting, leading to an increased deterioration of the NEG performances as a function of the number cycles.

In addition, these measurements seemed to demonstrate that the ageing process can be reduced by venting under a controlled dry air atmosphere.

A possible solution to the problem of ageing for NEG films could come from the employment of noble metals, which do not undergo the formation of a stable passivation layer on their surface and which are able to release all the pumped gas by heating, thus resulting in a practically unlimited life. Palladium thin film coatings, in particular, have low

binding energies for H_2 and CO but, on the other hand, they have a very high dissociation pressure for H_2 and they provide a negligible pumping for N_2 and CO_2; platinum coatings also seem to have similar characteristics [28].

Another possible solution which has been investigated might be the deposition of Pd or PdAg coatings on a pre-deposited NEG film. In this case, H_2 could be efficiently pumped by the noble metals and then it could migrate through the first layer to the NEG film, where it could be stored with a negligible dissociation pressure. For these purposes, Pd coatings could be replaced by PdAg ones, which provide a higher diffusion of H_2 to the NEG layer.

5.6.6 Discharge gas trapping and degassing

The presence of impurities in the deposited NEG coating is obviously undesired because it may strongly affect the getter's performances and it may lead during vacuum operations to a degassing of trapped molecules.

In particular, discharge gas molecules impinging on the cathode during the sputtering process may conserve a large fraction of their initial kinetic energy when they bounce back, leading to their possible subsequent implantation in the growing film.

The release of discharge noble gases, which are not pumped by NEG, could definitively compromise the maintenance of the required pressure degree inside a vacuum system during operation.

This seems to be particularly true for discharge gases with an atomic weight lower than that of the cathode material; in order to avoid this problem, the employment of a heavier discharge gas is preferred. Different materials have been sputtered using different discharge gases and the amount of gas trapped inside the film has been measured [23]: the results show that, for TiZrV deposition, krypton represents a better choice instead of argon, which has a lower atomic weight. An argon content of about *3500 ppm* has been found, while the value for krypton is lower by two orders of magnitude; a dependence on the surface film microstructure has also been pointed out.

6. TOOLS FOR PRESSURE DISTRIBUTION ANALYSIS

During the design of complex UHV systems like the LHC it is important to predict the pressure distribution in different parts of the system, for a given gas load and for the chosen pumping configuration. By varying the layout of a vacuum chamber, as well as its pumping configuration, it is possible to optimise the system's efficiency and to ensure the required specifications.

For certain applications, this process can be done simply exploiting analytical formulae of gas dynamics. However, if the accuracy of these formulae is too scarce or the vacuum system is too complex, the use of analytical formulations becomes impossible. In this cases, the Test-Particle Monte Carlo method is usually used: its theoretical principle will be briefly described in the next paragraph, as well as the functioning of MOLFLOW+, which is a code based on this method.

Moreover, the estimation of residual gas density profiles is indispensable to validate the design and to confirm the required vacuum stability conditions and beam lifetime in the UHV systems of high-energy particle accelerators where, as already said, the circulating beam can cause and enhance the desorption of gas molecules from the inner walls.

VASCO code was developed to face this need during the design of the beam vacuum system of the LHC and it will also be presented in this chapter.

6.1 MOLFLOW+

MOLFLOW+ is a C/C++ code which implements the test-particle Monte Carlo method (TPMC), allowing the analysis under UHV conditions of complex geometries that can be created using a CAD program [29]. In addition to the TPMC method, this software also implements the angular coefficient method (AC), which however has not been used for the purposes of this thesis.

MOLFLOW+ allows calculating pressure profile, transmission, adsorption distribution and effective pumping speed of a given vacuum system, in which a given amount of gas

molecules is injected, by dividing its internal surface into a certain number of finite elements and by calculating the interactions of the impinging gas molecules with everyone of them.
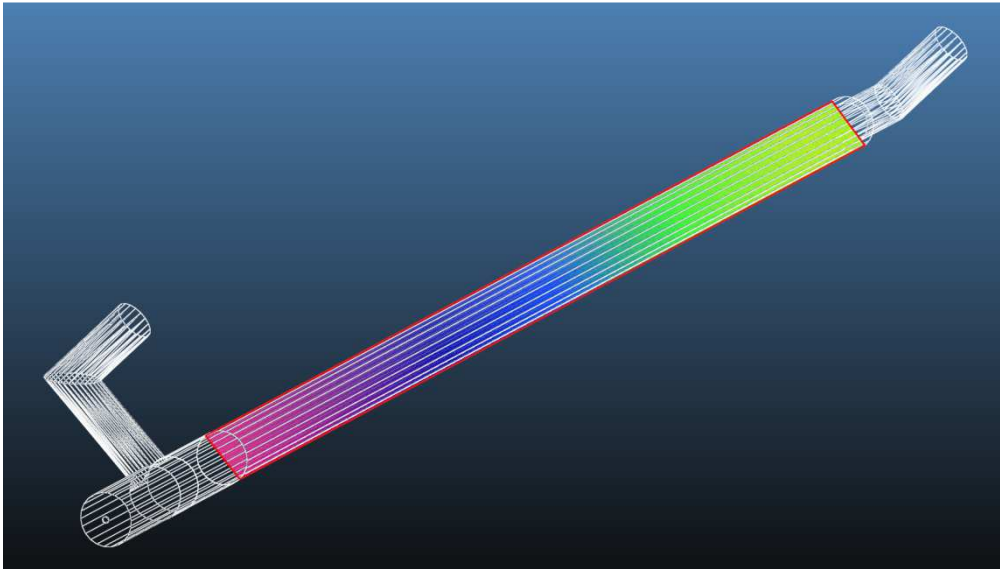
Figure 34 – Typical MOLFLOW+ output, with a texture applied indicating the pressure profile along a NEG vacuum chamber.

The program can also simulate the presence of different pumping systems, either localised (sputter-ion pumps) or distributed (NEG coatings). NEG sticking factor, entering molecular flow, outgassing from a surface, temperature and molecular mass are among the parameters that can be set before starting the simulation.

6.1.1 Theoretical basis: the test-particle Monte Carlo method

The TPMC method is an important tool for the calculation and determination of vacuum parameters in a system where molecular flow conditions are established: it consists in calculating a large number of molecular trajectories in order to get a picture of a rarefied gas flow. This technique has been widely used for computing pumping speeds and sticking probabilities of vacuum systems with adsorbing walls or of cryogenic surfaces and other pumps.

The virtue of the Monte Carlo method is that, with relatively little effort, also extremely complicated situations may be treated [19] [20] [30]. This is made possible by some assumptions that allow to simplify the calculations needed for the determination of the parameters of interest.

The gravitation is neglected and the molecular trajectories are assumed to be rectilinear.

Particles interact solely with the tube walls, therefore the history of a particle as it bounces down the tube is an event which is statistically independent on the histories of other particles. Following this assumption, a large number of typical particle trajectories can be numerically generated one by one and the average of these paths can be calculated, thus obtaining an estimation for the probabilities of various events. Since the trajectories are random, all decisions, such as the starting positions of the molecules in the desorbing plane, are governed by probability laws. In particular, desorption directions of particles are uniformly distributed and follow the cosine law:

$$p \cdot d\omega = \frac{1}{\pi} \cos \vartheta \cdot d\omega = \frac{1}{\pi} \cos \vartheta \cdot \sin \varphi \cdot d\vartheta d\varphi$$

where $pd\omega$ is the probability that a particle enters within the elementary solid angle $d\omega$ about θ and φ, the polar and azimuthal angles with respect to the normal to the entrance plane (Figure 35).
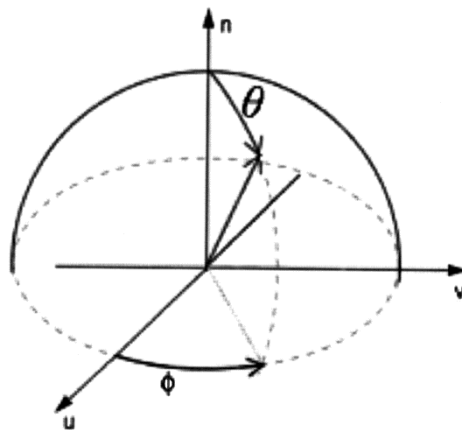
Figure 35 – Trajectory of a molecule emerging or being reflected from a surface, in accordance with the cosine law [29].

Also reflection is diffuse according to the same law, where the angles are, in this case, with respect to the normal to the tube wall, at the point of impact. Moreover, the angle of reflection does not depend on the angle of incidence.

For each individual collision of a particle with the adsorbing wall, the probability of being adsorbed is given by the sticking probability s. A random sequence of numbers uniformly distributed in the interval *[0,1]* is generated. Upon collision with the wall a random number Ψ is obtained and compared to the assigned value of s: if $\Psi \geq s$, the particle is reflected from the wall, otherwise it is considered to have been adsorbed and the calculation for its trajectory is terminated.

6.2 VASCO

The Vacuum Stability Code (VASCO) is a multi-gas code for the estimation of vacuum stability and gas density profiles in steady state conditions in UHV systems [10] [31]. Although being applicable to general problems requiring the solution of diffusion equations in geometries with cylindrical symmetry and with distributed sources and pumping, this code has been conceived for an accelerator performing hadron beam operations, like the LHC. As a matter of fact, VASCO code has been employed to validate the design of the beam vacuum system of the LHC, in order to check that the chosen geometry, pumping scheme, material and treatment are able to guarantee vacuum stability and low residual gas pressure, in accordance with the required beam lifetime and background noise to the experiments.

The model used for vacuum calculations assumes that the rate of change of molecules per unit volume depends on:

- molecular diffusion along the chamber, due to pressure gradient;
- beam-induced dynamic effects, i.e. ion, electron and photon-stimulated gas desorption;
- gas pumping distributed along the pipe (NEG coating in room temperature sectors or cryopumping in the magnets working at cryogenic temperatures);
- gas lumped pumping provided by sputter-ion pumps.

The model is based on cylindrical geometries with radial symmetry, thus allowing one-dimensional approximation along the beam axis: non-cylindrical beam pipes are approximated with cylinders having the same conductance and each parameter that is function of the wall surface area is scaled to take into account the real area (Figure 36).
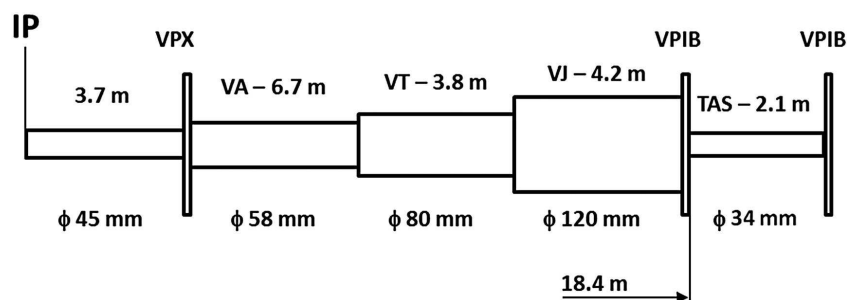
Figure 36 – Schematic view of the ATLAS vacuum system used for VASCO calculations [10].

Moreover, the code implements time invariant parameters, meaning that the residual gas density estimations performed are valid only for a specific moment in time, because some of these parameters (e.g. desorption yields and NEG distributed pumping) are time-dependent.

Finally, VASCO is a finite elements code, because it divides the vacuum system in several elements, each one characterised by a different set of parameters; boundary conditions must be properly set in order to ensure the continuity of gas density and flux between each pair of elements (Figure 37). This subdivision in several elements makes VASCO particularly suitable for residual gas pressure analyses concerning very long vacuum beam pipes, as for example the LSS of the LHC.
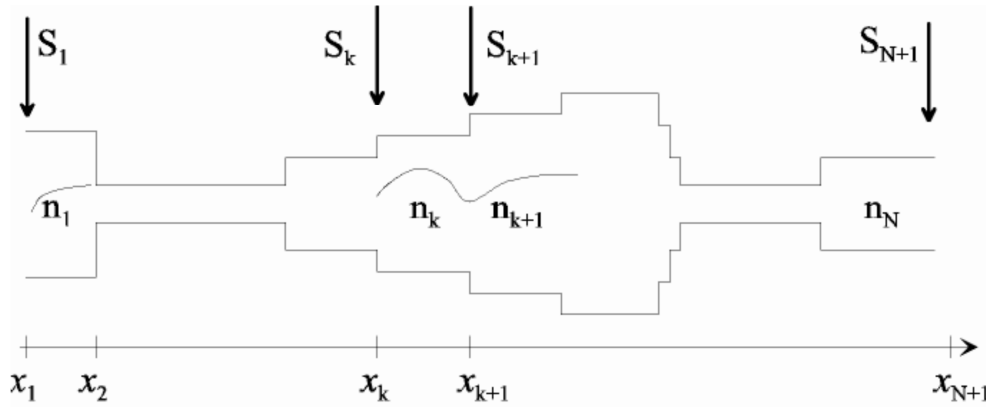
Figure 37 – Schematic view of a beam pipe with boundary conditions properly set: the sum of flux of molecules coming from the two sides of one boundary must be equal to the amount of molecules pumped (S) or generated by a local gas source (g) [31].

6.2.1 Theoretical basis: the multi-gas model

A valid estimation of gas density profiles in the LSS of the LHC should consider the presence of H_2, CH_4, CO and CO_2, which are usually the main residual gases present in UHV systems. The multi-gas model takes into account that each gas species, once ionised and accelerated to the wall by the charged beam, can desorb any other species of gas both from the inner walls of the system and, in case of a cryogenic system, from the condensed gas layer.

Therefore the equations for each gas depend on the gas densities of other species, resulting in an interdependence of all the equations. A single-gas model, instead, would imply that each gas species, once ionised, is able to desorb only molecules of the same species.

The general equation describing the evolution of the number of molecules per unit volume n_g for a given gas g is the following, where V is the volume of the vacuum chamber per unit length in $[m^2]$ and a is the vacuum chamber cross-section area in $[m^2]$:

$$V\frac{\partial n_g}{\partial t} = a \cdot D_g \cdot \frac{\partial^2 n_g}{\partial x^2} + \frac{I}{e}\sum_j \left(\eta_{i,j^+ \to g} \cdot \sigma_j^b \cdot n_j\right) - S_{dis}n_g + \eta_{ph} \cdot \dot{\Gamma}_{ph} + \eta_e \cdot \dot{\Gamma}_e + Aq_g$$

where the terms on the right side refer to:

- Molecular diffusion due to pressure gradient: aD_g is the specific conductance per unit length in $[m^4/s]$.

- Ion-induced cross-desorption: I is the beam current in $[A]$, e is the electron charge in $[C]$, $\eta_{i,j}$ is the ion-induced desorption yield in number of molecules per incident ion j^+ and σ_j^{b} is the ionisation cross-section of the gas-beam particle beam interaction in $[m^2]$.

- Distributed pumping of NEG coatings or cryopumping S_{dis}.

- Photon-induced gas desorption: η_{ph} is the gas desorption yield in number of molecules per incident photon, Γ_{ph} is the photon flux to wall per unit length $[m^{-1}{\cdot}s^{-1}]$.

- Electron-induced gas desorption: η_e is the gas desorption yield in number of molecules per incident electron, Γ_e is the electron flux to wall per unit length $[m^{-1}{\cdot}s^{-1}]$.

- Thermal outgassing q_g in $[mbar{\cdot}l/s]$, A being the surface area per unit length $[m]$.

Moreover, the set of equations that must be solved for each gas in order to obtain the evolution of the number of its molecules per unit volume can be expressed in a more compact and convenient matrix form by defining an appropriate set of vectors and matrices.

A more detailed discussion about the equations governing the model can be found in the mentioned references.

6.2.2 VASCO input file

VASCO code is implemented in Matlab. The input file must be a rectangular matrix without empty elements and the parameters are inserted per rows (Figure 38). Each component of the vacuum system should occupy four columns of the matrix, i.e. one for each gas subjected to analyses (H_2, CH_4, CO, CO_2).

Some parameters are independent of gas species: diameter and length of the chamber, temperature, electron and photon flux hitting the walls.

The other parameters depend on the type of gas and are related to lumped pumps, local gas sources, sticking probabilities for distributed pumping at room temperature (NEG coatings) or cryogenic temperature, ionisation cross-sections, ion, photon and electron-stimulated desorption yields, thermal outgassing and equilibrium pressure at a given temperature.

				Modulo Jura				NEG 7m				Modulo SS Jura				NEG 7m			
2	%		%	H2	CH4	CO	CO2	H2	CH4	CO	CO2	H2	CH4	CO	CO2	H2	CH4	CO	CO2
3	in_Segment = [		%	1	0	0	0	2	0	0	0	3	0	0	0	4	0	0	0
4	in_d = [	[mm]	%	80	0	0	0	80	0	0	0	80	0	0	0	80	0	0	0
5	in_L = [	[mm]	%	300	0	0	0	7000	0	0	0	300	0	0	0	7000	0	0	0
6	in_dist_ref = [	[mm]	%	0	0	0	0	300	0	0	0	7300	0	0	0	7600	0	0	0
7	in_T = [	[K]	%	300	0	0	0	300	0	0	0	300	0	0	0	300	0	0	0
8	in_S = [	[l/s](H2)	%	25	0	0	0	0	0	0	0	0	0	0	0	0	0	0	0
9		[l/s](CH4)	%	0	12.5	0	0	0	0	0	0	0	0	0	0	0	0	0	0
10		[l/s](CO)	%	0	0	25	0	0	0	0	0	0	0	0	0	0	0	0	0
11		[l/s](CO2)	%	0	0	0	25	0	0	0	0	0	0	0	0	0	0	0	0
12	in_g = [	[torr·l/s]	%	0	0	0	0	0	0	0	0	0	0	0	0	0	0	0	0
13	in_sigma = [		%	1.00E-23	0	0	0	1.00E-23	0	0	0	1.00E-23	0	0	0	1.00E-23	0	0	0
14			%	0	1.00E-23	0	0	0	1.00E-23	0	0	0	1.00E-23	0	0	0	1.00E-23	0	0
15			%	0	0	1.00E-23	0	0	0	1.00E-23	0	0	0	1.00E-23	0	0	0	1.00E-23	0
16			%	0	0	0	1.00E-23	0	0	0	1.00E-23	0	0	0	1.00E-23	0	0	0	1.00E-23
17	in_alpha = [		%	1.00E-12	0	0	0	0.05	0	0	0	1.00E-12	0	0	0	0.05	0	0	0
18			%	0	1.00E-12	0	0	0	1.00E-12	0	0	0	1.00E-12	0	0	0	1.00E-12	0	0
19			%	0	0	1.00E-12	0	0	0	0.50	0	0	0	1.00E-12	0	0	0	0.50	0
20			%	0	0	0	1.00E-12	0	0	0	0.50	0	0	0	1.00E-12	0	0	0	0.50
21	in_alpha_p = [		%	1.00E-12	0	0	0	1.00E-12	0	0	0	1.00E-12	0	0	0	1.00E-12	0	0	0
22			%	0	1.00E-12	0	0	0	1.00E-12	0	0	0	1.00E-12	0	0	0	1.00E-12	0	0
23			%	0	0	1.00E-12	0	0	0	1.00E-12	0	0	0	1.00E-12	0	0	0	1.00E-12	0
24			%	0	0	0	1.00E-12	0	0	0	1.00E-12	0	0	0	1.00E-12	0	0	0	1.00E-12
25	in_eta_i = [		%	0.541818964	0.541818964	0.541818964	0.541818964	0.541818964	0.541818964	0.541818964	0.541818964	0.541818964	0.541818964	0.541818964	0.541818964	0.541818964	0.541818964	0.541818964	0.541818964
26			%	0.036121264	0.054181896	0.072242528	0.108363793	0.036121264	0.054181896	0.072242528	0.108363793	0.036121264	0.054181896	0.072242528	0.108363793	0.036121264	0.054181896	0.072242528	0.108363793
27			%	0.25284885	0.288970114	0.288970114	0.325091378	0.25284885	0.288970114	0.288970114	0.325091378	0.25284885	0.288970114	0.288970114	0.325091378	0.25284885	0.288970114	0.288970114	0.325091378
28			%	0.144485057	0.144485057	0.144485057	0.144485057	0.144485057	0.144485057	0.144485057	0.144485057	0.144485057	0.144485057	0.144485057	0.144485057	0.144485057	0.144485057	0.144485057	0.144485057
29	in_eta_p_i = [		%	1.00E-03	0	0	0	1.00E-03	0	0	0	1.00E-03	0	0	0	1.00E-03	0	0	0
30			%	0	1.00E-03	0	0	0	1.00E-03	0	0	0	1.00E-03	0	0	0	1.00E-03	0	0
31			%	0	0	1.00E-03	0	0	0	1.00E-03	0	0	0	1.00E-03	0	0	0	1.00E-03	0
32			%	0	0	0	1.00E-03	0	0	0	1.00E-03	0	0	0	1.00E-03	0	0	0	1.00E-03
33	in_eta_e = [		%	0.001774173	6.46E-05	0.000452095	0.000387369	0.001774173	6.46E-05	0.000452095	0.000387369	0.001774173	6.46E-05	0.000452095	0.000387369	0.001774173	6.46E-05	0.000452095	0.000387369
34	in_eta_p_e = [		%	0	0	0	0	0	0	0	0	0	0	0	0	0	0	0	0
35	in_eta_ph = [		%	0.00015	0.000004	0.000015	0.000025	0.00015	0.000004	0.000015	0.000025	0.00015	0.000004	0.000015	0.000025	0.00015	0.000004	0.000015	0.000025
36	in_eta_p_ph = [		%	0	0	0	0	0	0	0	0	0	0	0	0	0	0	0	0
37	in_Cbs = [		%	0	0	0	0	0	0	0	0	0	0	0	0	0	0	0	0
38			%	0	0	0	0	0	0	0	0	0	0	0	0	0	0	0	0
39			%	0	0	0	0	0	0	0	0	0	0	0	0	0	0	0	0
40			%	0	0	0	0	0	0	0	0	0	0	0	0	0	0	0	0
41	in_Qth = [		%	7.06E-12	3.53E-15	1.76E-14	1.76E-14	5.00E-14	3.00E-17	1.00E-14	1.00E-14	7.06E-12	3.53E-15	1.76E-14	1.76E-14	5.00E-14	3.00E-17	1.00E-14	1.00E-14
42	in_n_e = [		%	0	0	0	0	0	0	0	0	0	0	0	0	0	0	0	0
43	in_N_e = [		%	0	0	0	0	0	0	0	0	0	0	0	0	0	0	0	0
44	in_Gamma_ph = [		%	0	0	0	0	0	0	0	0	0	0	0	0	0	0	0	0
45	in_S_Nplus1 = [	[l/s](H2)	%	25	0	0	0	0	0	0	0	0	0	0	0	0	0	0	0
46		[l/s](CH4)	%	0	12.5	0	0	0	0	0	0	0	0	0	0	0	0	0	0
47		[l/s](CO)	%	0	0	25	0	0	0	0	0	0	0	0	0	0	0	0	0
48		[l/s](CO2)	%	0	0	0	25	0	0	0	0	0	0	0	0	0	0	0	0
49	in_g_Nplus1 = [	[torr·l/s]	%	0	0	0	0	0	0	0	0	0	0	0	0	0	0	0	0

Figure 38 – Example of a typical VASCO input file.

71

7. EXPERIMENTAL SETUP

The aim of this work is to study the saturation behaviour of NEG coated vacuum chambers, focusing on the evolution of their pumping characteristics as the saturation of the coating progresses.

Two different NEG coated vacuum systems were therefore saturated by means of several consecutive CO injections and the progressive variations of transmission, pumping speed and capture probability for different gases were recorded and analysed. The first measurements were conducted on a *2 m* long NEG coated vacuum chamber, that allowed to easily collect important data thanks to its relatively simple configuration.

Figure 39 – View of the laboratory at CERN; the *28 m* long pilot sector is in the foreground.

The second and more complex system is a *28 m* long NEG coated vacuum pilot sector, which reproduces the structure of a typical LSS vacuum beam pipe described in Chapter 1, thus

allowing to use the so-obtained experimental results for the evaluation of the real saturation levels in the LHC beam pipes.

Both these vacuum systems are installed at CERN in the laboratory and will be exhaustively described in the following two paragraphs (Figure 39).

7.1   2 m LONG NEG COATED VACUUM CHAMBER

A schematic view of the experimental test bench is showed in Figure 40. The system comprises a stainless steel Fischer-Mommsen type dome with an internal conductance, whose diameter is equal to *1 cm*.
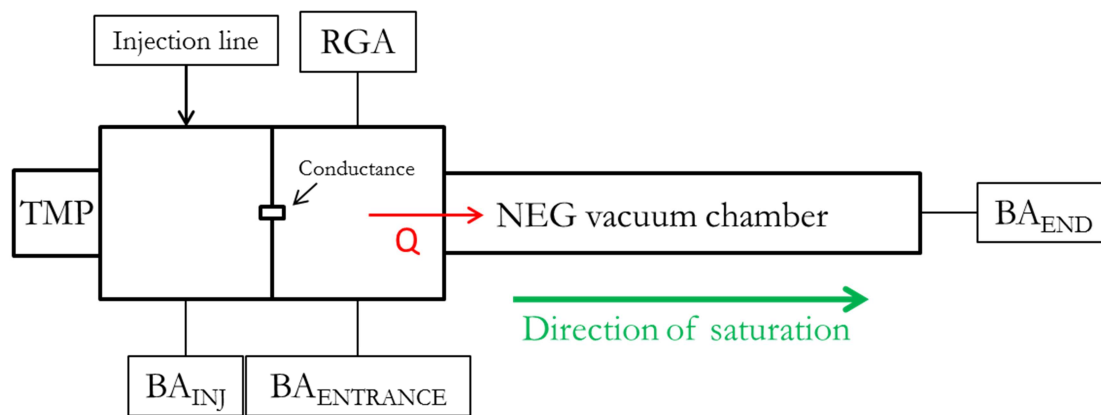
Figure 40 – Schematic view of the experimental test bench, showing the Fischer-Mommsen dome, the *216 cm* long NEG coated vacuum chamber and all the equipment for pumping and pressure measurements.

A *216 cm* long cylindrical NEG coated vacuum chamber is connected to the dome; as the vacuum beam pipes of the LSS in the LHC, this chamber is made of OFC copper, its wall thickness is equal to *2 mm* and the diameter of its cross-section is *8 cm*.

The dome is equipped with two hot cathode Bayard-Alpert (BA) gauges – respectively before and after the conductance – and with a RGA (Balzers QMG422 with a QMA 125 head). A third BA gauge is situated at the end of the NEG coated vacuum chamber.

In addition to the pumping supplied by the NEG coating, a turbomolecular pump (TMP) is installed on the dome, providing a nominal pumping speed of *60 l/s* for N_2.

Finally, the injection line is connected to the dome by means of a Varian variable leak valve. In the line, gas bottles of H_2, CO and N_2 are installed. Pumping on the injection line is provided by another TMP, with the same characteristics of the previous one.

7.2   28 m LONG NEG COATED VACUUM PILOT SECTOR

The pilot sector is made of four NEG coated OFC vacuum chambers. Each one of these chambers is *7 m* long, for a total length of *28 m* NEG coated beam pipe (Figure 41). As for the smaller vacuum system described in the previous paragraph, each chamber has an internal diameter equal to *8 cm* and a wall thickness of *2 mm*. Beam pipes with the same length and diameter are commonly employed in the LSS vacuum sectors of the LHC.

The NEG coated chambers are interconnected by three stainless steel modules with integrated stainless steel RF screens (Figure 42): the central one (1) is *28 cm* long, while the other two (2, 3) are *18 cm* long.
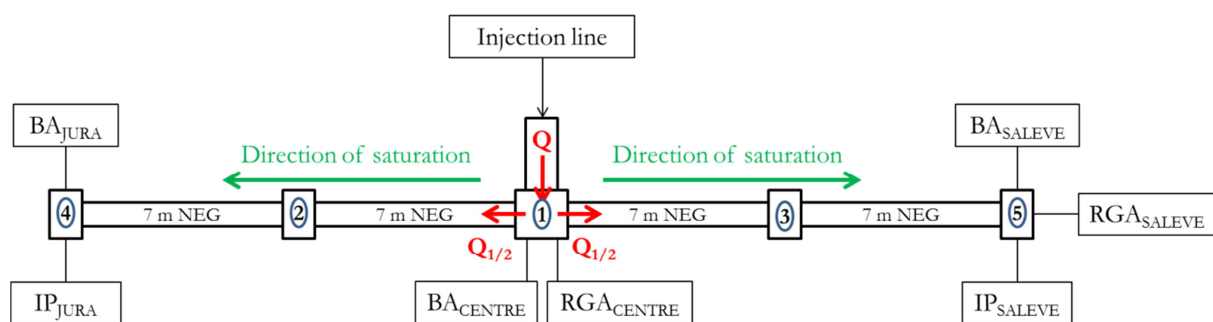
Figure 41 – Schematic view of the 28 m long pilot sector, showing the four 7 m long NEG coated vacuum chambers, the interconnecting stainless steel modules and all the equipment for pumping and pressure measurements.

For simplicity, according to the orientation of the pilot sector in the laboratory with respect to Geneva's surrounding mountains, the two sides of the pilot sector will be indicated as "Jura side" and "Salève side", respectively.

Two additional modules (4, 5), each one *28 cm* long, are located at the ends of the pilot sector; each of them houses a BA gauge (BA_{JURA} and BA_{SALEVE}) and a sputter-ion pump (IP_{JURA} and IP_{SALEVE}), each providing a nominal pumping speed of *30 l/s* for N_2. The module on Salève side houses also a RGA, namely RGA_{SALEVE} (Balzers QMG422 with a QMA 125 head).

In addition, a third BA gauge (BA_{CENTRE}) and a second RGA (RGA_{CENTRE}) are located in the central module, which is connected to the injection line by an all-metal seal valve. Finally, a Penning gauge is installed in the central module and it is used to follow pressure during bakeout and vacuum activation processes.

74
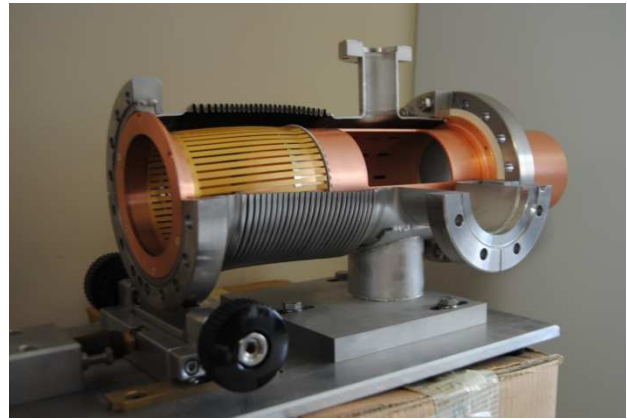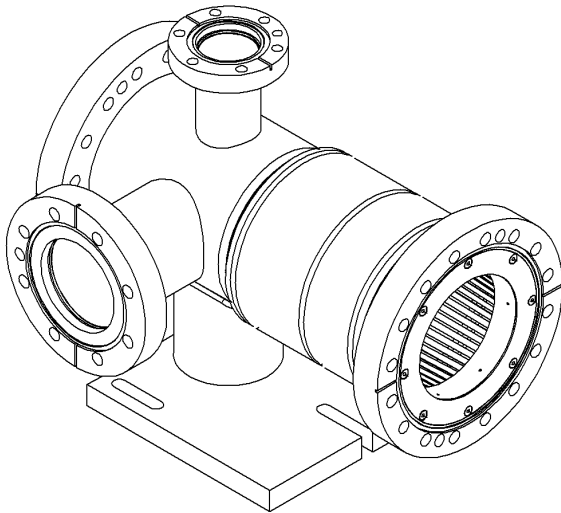
Figure 42 – Layout and picture of a stainless steel module identical to those located at the ends of the pilot sector; the inner RF copper screen and the insert for the instrumentation are visible.

7.2.1 Injection line of the 28 m long pilot sector

A schematic view of the injection line is visible in Figure 43.
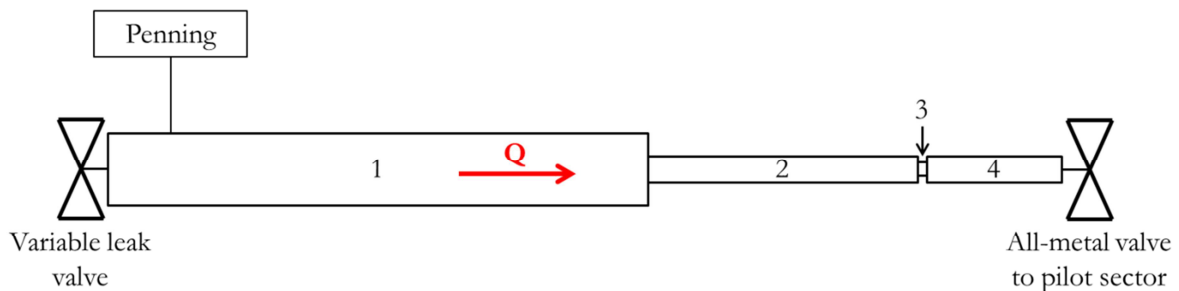
Figure 43 – Schematic view of the injection line.

The line is made of three pipes (1, 2, 4) with the following dimensions:

- *40 cm* of length and *1.6 cm* of diameter (1);
- *20 cm* of length and *0.6 cm* of diameter (2);
- *10 cm* of length and *0.6 cm* of diameter (4).

Between the last two pipes is located a conductance (3) with negligible thickness and diameter equal to 0.*15 cm*.

The line is connected to the pilot sector by the above-mentioned all-metal seal valve.

At the other end, a variable leak valve connects to the rest of the injection line, where pressure is monitored by means of a compact full-range gauge and which is in turn connected to the gas bottles and pumped by a TMP.

A Penning gauge is located on the *40 cm* long pipe, just after the variable leak valve, and it is used to calculate the gas flow entering into the pilot sector according to the following equation:

$$Q = C_{TOT}\left(\Delta P_{INJ} - \Delta P_{CENTRE}\right)$$

where, for every gauge, *ΔP* refers to the difference between the measured pressure during the injection and the initial one. P_{INJ} is the pressure measured by the Penning gauge on the injection line, while P_{CENTRE} is measured by the BA$_{CENTRE}$ gauge. C_{TOT} is the total conductance of the injection line, calculated considering a series connection of three pipes with constant cross-section (1, 2, 4) and one aperture (3):

$$C_{TOT} = \left(\frac{1}{C_1} + \frac{1}{C_2} + \frac{1}{C_3} + \frac{1}{C_4}\right)^{-1}$$

Values of C_{TOT} in *[l/s]* for different gases at *20 °C* are reported in Table 13.

Table 13 – Conductance of the injection line calculated for different gases at *20 °C*.

Air [l/s]	H$_2$ [l/s]	N$_2$ [l/s]	CO [l/s]
0.0583	0.222	0.0593	0.0593

8. RESULTS ANALYSIS

8.1 ACCURACY OF VACUUM GAUGES

The relative uncertainty in the pressure measurements of the BA gauges employed at CERN has been estimated by measuring pressure at the same time with ten different gauges of the same type in a vacuum dome where a certain gas flow was injected.

The results of these calculations for each gauge are plotted in the form of N_2 eq. pressure as a function of the average N_2 eq. pressure measured by all the gauges (Figure 44). It is possible to notice that the average relative uncertainty for these gauges corresponds to approximately *20%* of the average measured pressure.
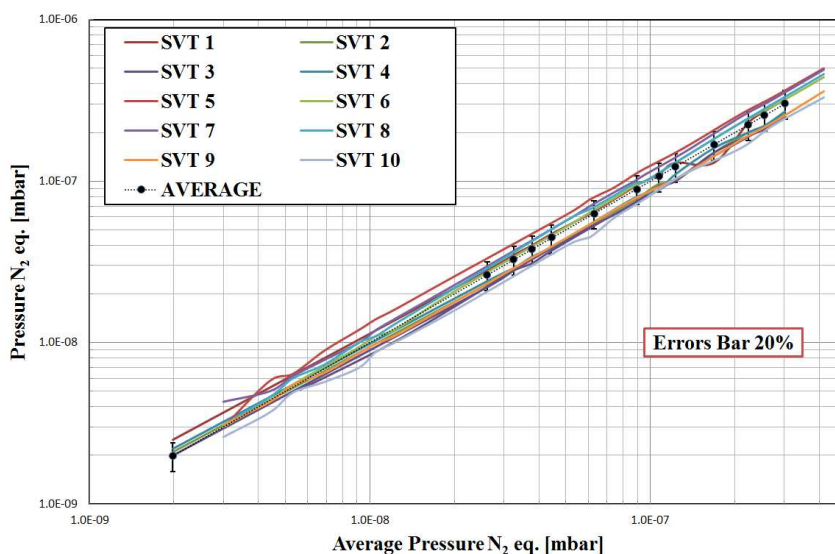
Figure 44 – Estimation of the relative uncertainty in pressure reading of the BA gauges used at CERN.

In addition, a correct estimation of the error in pressure readings of a BA gauge should take into account the fact that the sensibility of the gauge is a non-linear function of pressure and therefore the uncertainty of a measurement depends also on the pressure range under investigation: the closer is the measurement to the limits of the gauge's working range, the higher is the uncertainty. Moreover, data collected at pressures lower than $8 \cdot 10^{-12}$ *mbar* are more subjected to fluctuations due to their proximity to the lower functioning limit of the gauge (Figure 45).

The obtainment of accurate and precise results depends also on several other factors, such as the fact that the calibration constants may change with time, as well as the prior usage of the gauge and its cleanliness.
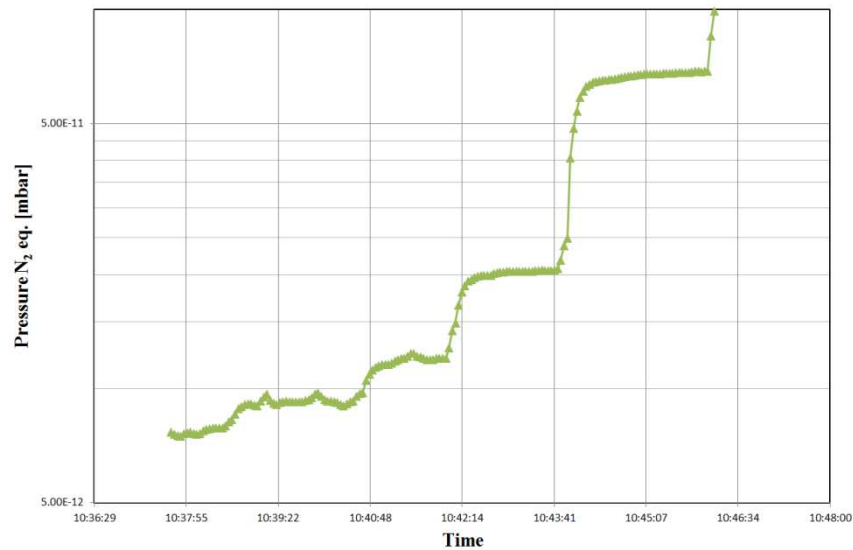
Figure 45 – Significant pressure fluctuations are observable for BA gauges at very low pressures.

Other measurements conducted at CERN in the past seem to confirm this error quantification and add an estimation of the relative uncertainty also for other types of vacuum gauges that have been employed for the purposes of this thesis work (Table 14).

Table 14 – List of vacuum gauge, showing their operating pressure ranges and accuracies.

Type of gauge	Pressure range	Relative uncertainty (% of the reading)
Pirani passive gauge	$1000 - 10^{-3}$ mbar	≈30% (if P<100 mbar)
Compact full range gauge	$100 - 10^{-9}$ mbar	≈30%
Cold-cathode Penning gauge	$10^{-3} - 10^{-11}$ mbar	≈30%
Hot-cathode Bayard-Alpert gauge with modulator	$10^{-7} - 10^{-12}$ mbar	≈10% for calibrated gauges, otherwise ≈30%

All the mentioned influencing factors should be taken into account when calculating transmissions, pumping speeds and capture probabilities, because these quantities are derived from pressure data and therefore they are characterised by a certain uncertainty.

However, the calculation of the precise relative uncertainty for every performed measurement would has been too hard, due to the several influencing factors that must be considered, and therefore it has been omitted in this study.

A percentage relative uncertainty ranging between *20%* and *50%* must be considered for these quantities.

8.2   2 m LONG NEG COATED VACUUM CHAMBER

8.2.1   Working procedure

The saturation of the NEG coated chamber was performed by means of several injections of CO. After every CO saturation, two small H_2 and N_2 injections were also performed, aiming to measure the variations of transmission, pumping speed and capture probability for each gas as functions of the NEG saturated length.

Table 15 summarises how transmission, pumping speed and capture probability have been calculated, according to the description of the experimental setup reported in Chapter 7. For a given gauge, *ΔP* refers to the difference between the measured pressure during the injection and the initial one.

Table 15 – Expressions for transmission, pumping speed and capture probability of the *2 m* long NEG coated vacuum chamber.

	Units	Expression
Transmission	[-]	$Tr = \dfrac{\Delta P_{ENTRANCE}}{\Delta P_{END}}$
Pumping speed	[l/s]	$S = \dfrac{Q}{\Delta P_{ENTRANCE}} = C \cdot \dfrac{\Delta P_{INJ} - \Delta P_{ENTRANCE}}{\Delta P_{ENTRANCE}}$
Capture probability	[-]	$\%CP = \dfrac{S}{C_{ENTRANCE}}$

Q is the entering gas flow in *[mbar·l/s]* and C is the conductance inside the Fischer-Mommsen type dome. As already explained in Chapter 2, the conductance of an aperture for air at *20 °C* in *[l/s]* is calculated as:

$$C = 11.6 \cdot A$$

where A is the area of the aperture's cross-section in $[cm^2]$. Its values for H_2, N_2 and CO have been derived from this equation and are reported in Table 16.

Table 16 – Conductances characterising the system for H_2, N_2 and CO (the diameter of the internal conductance in the Fischer-Mommsen type dome is *1 cm*.

	H₂	**N₂**	**CO**
C [l/s]	34.7	9.3	9.3
C$_{ENTRANCE}$ [l/s]	2220.3	593.4	593.4

Capture probability *%CP* represents the probability for gas molecules to be absorbed after having entered the NEG vacuum chamber. As already mentioned in Chapter 5, capture probability increases if the NEG sticking coefficient increases (Figure 21) and it is calculated as:

$$\%CP = \frac{S}{C_{ENTRANCE}}$$

where $C_{ENTRANCE}$ is the conductance in *[l/s]* at the entrance of the NEG coated vacuum chamber, i.e. its ideal pumping speed. Values of $C_{ENTRANCE}$ for different gases have also been derived from the same equation used for *C* (taking into account that in this case the diameter of the cross-section correspond to the diameter of the NEG coated vacuum chamber, which is equal to *8 cm*) and are reported in Table 16.

The operating procedure for every gas injection has been the following. Before starting injecting gas, a first RGA scan has to be done in analog mode, in order to calibrate each channel of the gas analyser: every channel is set to monitor in time the precise mass corresponding to the maximum of a mass peak. For example, aiming at following mass *2* (H₂), the related channel could be set to *2.19* because the maximum of the hydrogen peak measured by the RGA is centred at this value.

Meanwhile, the injection line must be cleaned from the residual gases of previous injections, in order to ensure the highest possible gas purity during the injection. This is made possible by injecting a certain quantity of the needed gas into the line and then by pumping it until a pressure in the low 10^{-7} *mbar* range is reached. This operation must be repeated at least *3-4* times.

Table 17 – Example of H₂ injection performed step by step; data refer to the same injection of Figure 46.

Step	P_{INJ} [mbar]	$P_{ENTRANCE}$ [mbar]	P_{END} [mbar]	Tr	S [l/s]	%CP
0	$2.3 \cdot 10^{-10}$	$2.5 \cdot 10^{-11}$	$7.5 \cdot 10^{-12}$	-	-	-
1	$2.3 \cdot 10^{-9}$	$2.7 \cdot 10^{-10}$	$2.5 \cdot 10^{-11}$	14.1	240.1	10.8%
2	$3.6 \cdot 10^{-9}$	$4.5 \cdot 10^{-10}$	$3.8 \cdot 10^{-11}$	14.2	242.2	10.9%
3	$5.9 \cdot 10^{-9}$	$7.4 \cdot 10^{-10}$	$5.7 \cdot 10^{-11}$	14.2	240.9	10.9%
4	$9.3 \cdot 10^{-9}$	$1.2 \cdot 10^{-9}$	$8.9 \cdot 10^{-11}$	14.1	237.4	10.7%
5	$1.1 \cdot 10^{-8}$	$1.4 \cdot 10^{-9}$	$1.1 \cdot 10^{-10}$	13.6	243.6	11.0%

Finally, after the RGA has been properly set and the injection line filled with gas, the injection can start. Every gas injection is performed in steps by opening little by little the injection valve. After every step it is necessary to wait for pressures to stabilise on the three gauges around a certain value before opening again the valve. For every opening step, pressure measured by every gauge after the stabilisation is noted down and thus transmission, pumping speed and capture probability characterising every step can be afterward calculated (Table 17).
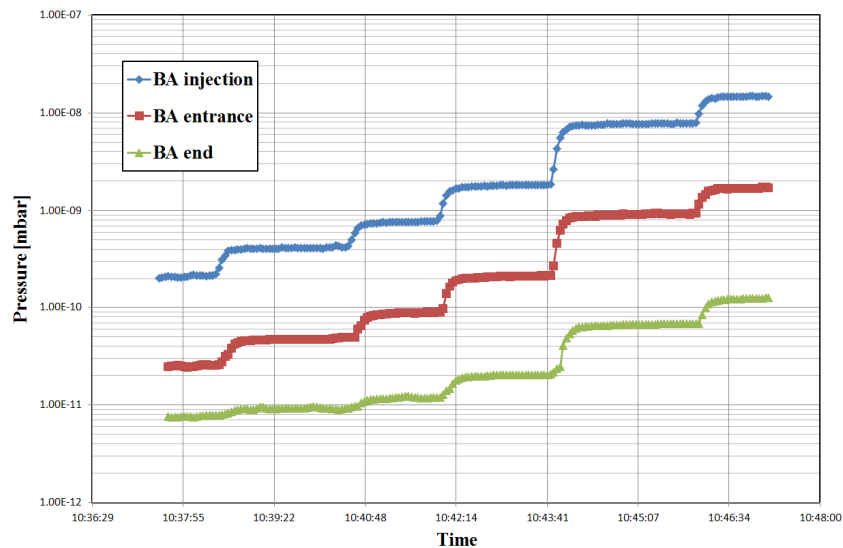
Figure 46 – Example of H₂ injection performed step by step.

During the injection, all the ion current data coming from the RGA and the pressure values from the BA gauges are collected and displayed by an especially conceived Labview program, which allows to save all the data in .txt format files (Figure 46).

The injection ends when a fixed ultimate value of P_{INJ} is reached on the BA gauge close to the injection line (Table 18).The ultimate pressures for H_2 and CO are determined by the fact that a higher pressure would cause instability in the incoming gas flow. The ultimate pressure for N_2 instead is considerably lower because, as already explained in Chapter 5, this gas is able to saturate a NEG surface faster than CO, due to the fact that every atom needs *6-7* free adjacent surface sites to be adsorbed. For the same reason, N_2 injections have also been the shortest (maximum *4-5* minutes) and have been performed in only one step.

Table 18 – Ultimate P_{INJ} pressure at the end of every injection for the three gases of interest.

H_2	N_2	CO
$1 \cdot 10^{-8}$ mbar	$1 \cdot 10^{-9}$ mbar	$5 \cdot 10^{-7} - 1 \cdot 10^{-6}$ mbar

8.2.2 Evolution of transmission, pumping speed and capture probability as functions of the NEG saturated length

Table 19 reports the initial values of transmission, pumping speed and capture probability for the three gases of interest. These values have been measured when the NEG coating was still completely activated, after having performed a full bakeout and NEG activation of the vacuum system.

CO transmission is considerably larger because the NEG sticking coefficient for this gas is the highest (about *0.7*) and therefore only a small amount of CO molecules can reach the end of the vacuum chamber if the NEG is completely activated. The sticking coefficients for N_2 and H_2 instead are lower (about *0.1* and *$5 \cdot 10^{-3}$*, respectively), thus their transmissions are also lower. Capture probability reflects this behaviour because, as already said, it is directly proportional to the sticking factor.

Table 19 – Initial values of transmission, pumping speed and capture probability, corresponding to a completely activated NEG coating.

	Tr	S [l/s]	%CP
H_2	16.9	284.5	12.9%
N_2	99.8	107.4	18.1%
CO	231.5	239.6	40.5%

Figure 47 shows the transmission variations for H_2, N_2 and CO as the saturation of the NEG coating progresses: as expected, transmission (which is the inverse of transmission probability) decreases for all gases as the saturated length increases, due to the fact that, if a larger NEG wall area is saturated, more gas molecules are able to reach the end of the vacuum chamber without being absorbed.
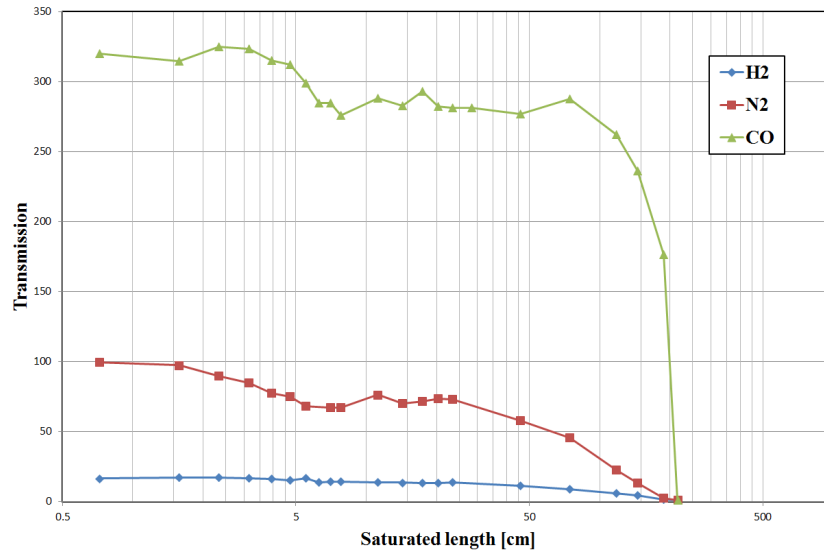

Figure 47 – Transmissions of H_2, N_2 and CO as functions of the NEG saturated length.

When there is no more NEG activated, i.e. when *Tr=1*, the pressure along the vacuum chamber is constant because there is no more pumping.

The percentage of lost transmission with respect to the initial one is shown in Table 20 for different saturated lengths. CO transmission seems to decrease more slowly as saturation progresses, while for H_2 and N_2 it is reduced by approximately half of the initial value even if only one third of the total length is saturated.

Table 20 – Percentage of lost transmission of H_2, N_2 and CO as a function of the NEG saturated length.

	NEG Saturated length			
	17 cm	74 cm	145 cm	188 cm
H_2	20%	46%	74%	90%
N_2	10%	43%	83%	97%
CO	8%	10%	26%	45%

This behaviour could be explained by the different sticking coefficients and the different adsorption mechanisms of the NEG coating for these gases.

As already mentioned at the beginning of this paragraph, the sticking coefficients for H_2, N_2 and CO are reported to be about $5 \cdot 10^{-3}$, 0.1 and 0.7, respectively. The higher is the sticking factor, the higher is the transmission for different saturated lengths, as shown in Figure 47.

NEG coating adsorption mechanism plays a crucial role too. The transmission curve for CO gives us important information about the saturation process of the NEG coating. Each CO molecule needs one free site to be adsorbed. The saturation of the NEG vacuum chamber is progressive and, due to the high CO sticking factor, a small length of activated NEG is enough to keep the transmission to a constant value.

However, this CO saturation front is responsible for the transmission decreases of H_2 and N_2: their pumping speed is inhibited by the CO pre-adsorption. In particular for H_2 molecules, due to their low sticking coefficient, as the saturation front advances, a higher amount of gas molecules could reach the end of the NEG vacuum chamber without being adsorbed.

The NEG pumping mechanism for N_2 is different compared to CO and H_2: N_2 molecules require to be adsorbed in many adjacent free sites underneath the first surface monolayer. As the CO saturation front advances, beside the relatively high sticking factor for N_2, the number of active sites for the adsorption decreases and a major amount of gas can reach the end of the NEG vacuum chamber.

Table 21 reports the percentage of lost pumping speed for different saturated lengths. It is possible to notice that, for all the gases, even approximately one tenth of the initial total length is sufficient to ensure about *25%* of the initial pumping speed.

Table 21 – Percentage of lost pumping speed of H_2, N_2 and CO as a function of the NEG saturated length.

	NEG Saturated length			
	17 cm	74 cm	145 cm	188 cm
H_2	17%	33%	52%	72%
N_2	27%	48%	62%	75%
CO	42%	58%	66%	73%

The percentage of lost pumping speed abruptly increases only when even the last *20 cm* of still vacuum activated NEG become saturated (Figure 48).

Thanks to the fact that this quantity does not depend on the geometry of the vacuum system, the calculation of the percentage of lost pumping speed is very important because it could

help in estimating the saturated length of the NEG coated vacuum beam pipes of the LHC, as will be widely explained in Chapter 9.

The decrease of capture probability follows the same trend, due to the fact that its value is derived from pumping speed.
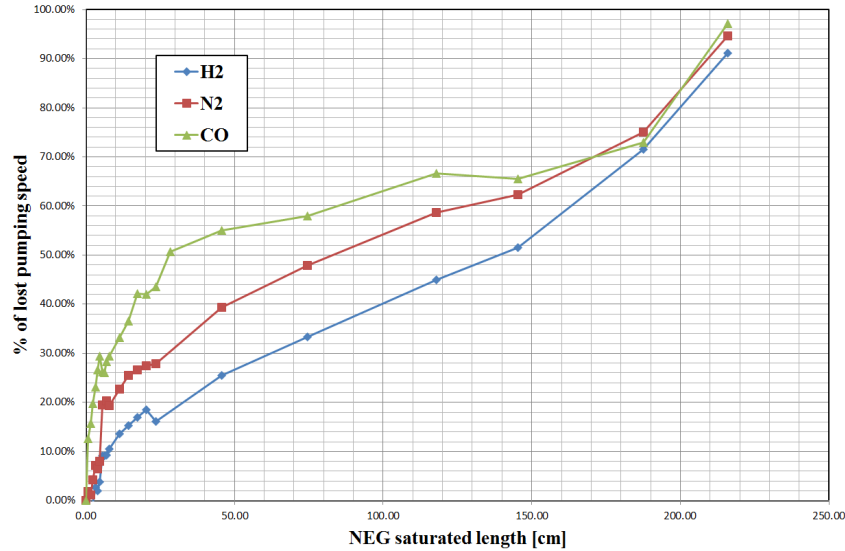
Figure 48 – Percentage of lost pumping speed with respect to the initial one as a function of the NEG saturated length.

The injections of CO, alternated with those of H_2 and N_2, continued until the whole length of the NEG coated chamber was saturated.

Figure 49 shows the pressure profiles recorded by the three BA gauges during the last CO injection. P_{END} progressively increased until it became equal to $P_{ENTRANCE}$, thus indicating that the NEG chamber was completely saturated and did not provide pumping anymore.

Afterwards, by analysing the Labview pressure data collected during every CO injection, it was possible to calculate the total amount of CO molecules injected for the complete saturation of the NEG surface.

Labview records pressure on the three gauges every three seconds, so that for everyone of this time intervals it is possible to calculate the incoming gas flow Q in *[mbar·l⁻¹·s⁻¹]*:

$$Q = C \cdot \left(\Delta P_{INJ} - \Delta P_{ENTRANCE}\right)$$

The total quantity of gas $G_{t=x+3}$ in *[mbar·l⁻¹]* injected during the time interval *t=x+3* can be obtained according to the following equation:

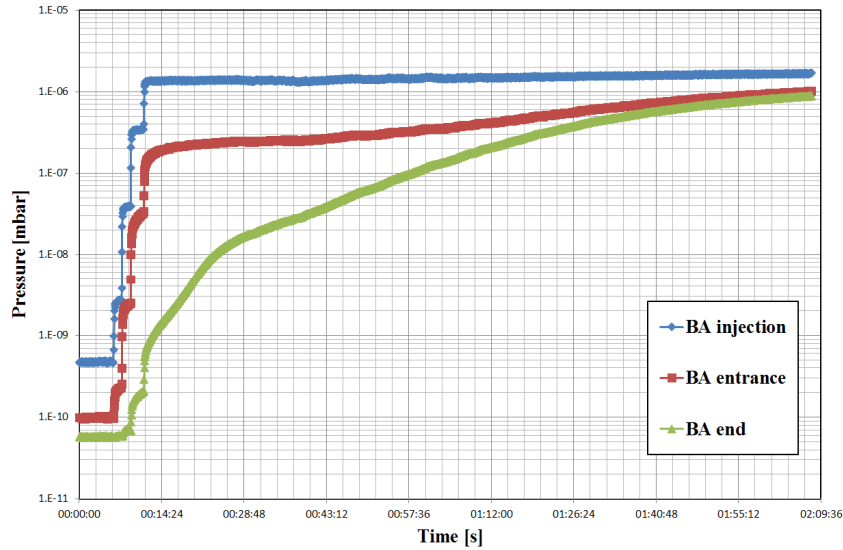$$G_{t=x+3} = G_{t=x} + Q_{t=x+3} \cdot (t_{x+3} - t_x)$$

Figure 49 – Pressure evolution in the system during the last CO injection.

After having calculated G_{total}, corresponding to the amount of molecules injected during the whole injection, and having converted it in [$Pa \cdot m^3$], the corresponding total amount N_{total} of injected CO molecules can be obtained as follows:

$$N_{total} = M_{total} \cdot N_A = \frac{G_{total}}{RT} \cdot N_A$$

Table 22 – Summary of the performed CO injections and of the progression of NEG saturation.

Injection	Total injected molecules	Total saturated area [cm^2]	Total saturated lenght [cm]
1	$4.02 \cdot 10^{16}$	18.07	0.72
2	$8.82 \cdot 10^{16}$	39.65	1.58
3	$1.30 \cdot 10^{17}$	58.68	2.33
4	$1.75 \cdot 10^{17}$	78.87	3.14
5	$2.20 \cdot 10^{17}$	98.89	3.93
6	$2.63 \cdot 10^{17}$	118.39	4.71
7	$3.09 \cdot 10^{17}$	139.03	5.53
8	$3.51 \cdot 10^{17}$	157.75	6.28
9	$3.93 \cdot 10^{17}$	176.53	7.02
10	$4.36 \cdot 10^{17}$	195.92	7.80
11	$6.25 \cdot 10^{17}$	281.29	11.19
12	$8.00 \cdot 10^{17}$	359.82	14.32
13	$9.71 \cdot 10^{17}$	436.65	17.37
14	$1.14 \cdot 10^{18}$	512.35	20.39
15	$1.31 \cdot 10^{18}$	590.12	23.48
16	$1.58 \cdot 10^{18}$	712.59	28.35
17	$2.55 \cdot 10^{18}$	1147.72	45.67
18	$4.16 \cdot 10^{18}$	1871.15	74.45
19	$6.59 \cdot 10^{18}$	2964.68	117.96
20	$8.13 \cdot 10^{18}$	3654.34	145.40
21	$1.05 \cdot 10^{19}$	4713.08	187.53
22	$1.21 \cdot 10^{19}$	5428.67	216.00

where M_{total} is the total injected amount of CO in *[mol]*, *R=8.314 J·mol⁻¹·K⁻¹* is the gas constant and $N_A=6.022·10^{23}$ is Avogadro's number.

By summing the N_{total} contributes of every CO injection, the total amount of injected CO necessary to achieve the complete saturation of the NEG chamber results to be equal to *1.2·10¹⁹ molecules* (Table 22).

Finally, knowing that the internal wall area of the NEG coated chamber is equal to *5428.67 cm²*, it is possible to calculate the number of CO molecules per unit area adsorbed by the NEG vacuum chamber, which corresponds to *2.2·10¹⁵ molecules/cm²*.

This result is in agreement with the values obtained from previous measurements [22] [23].

8.2.3 Correlation between pumping speed and conductance of the vacuum chamber

The evolution of pumping speed for H_2, N_2 and CO as a function of the NEG saturated length was compared to the effective pumping speed S_{EFF} (Figure 50).

S_{EFF} corresponds to the real NEG pumping speed seen by the BA gauge at the beginning of the NEG chamber, scaled with the conductance of increasingly longer saturated part of the chamber separating the gauge by the still activated one:

$$S_{EFF} = \left(\frac{1}{S_{NEG,0}} + \frac{1}{C_{TUBE}} \right)^{-1}$$

where C_{TUBE} is the conductance of the pipe and $S_{NEG,0}$ is the initial NEG pumping speed measured before starting the saturation, when the chamber was still completely activated.
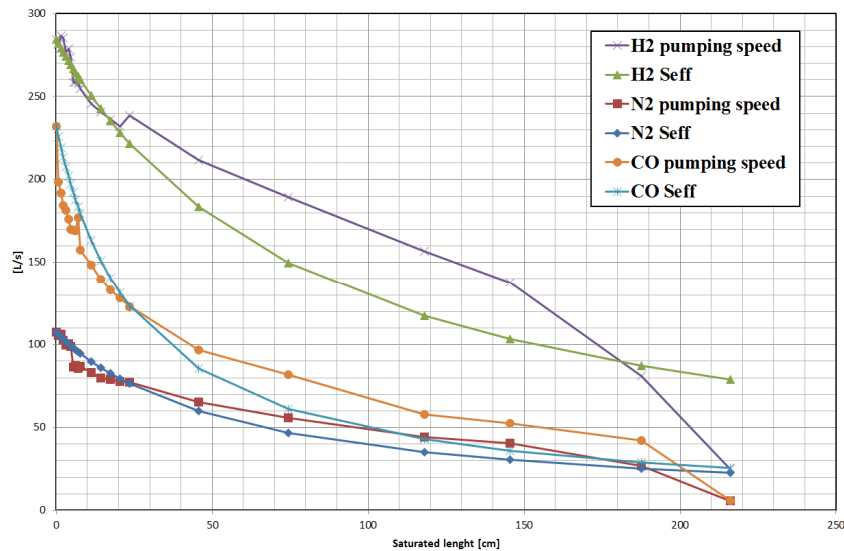

Figure 50 – Comparison between pumping speed and effective pumping speed for H₂, N₂ and CO.

It is possible to notice that, except for the last and the first points (the latter corresponding to few *cm* of NEG saturated), for each gas S_{EFF} is always lower, indicating that the calculated scaling with the conductance of the vacuum chamber's saturated length underestimates the measured pumping speed.

8.2.4 Pumping speed variations as seen by the BA gauges

Figure 51 compares the H_2 pumping speed variations as seen by the two gauges BA_{END} and $BA_{ENTRANCE}$, located respectively at the end and at the beginning of the NEG vacuum chamber.

When the whole NEG chamber was activated for the first time, it was possible to calculate the degassing flow $Q_{DEGAS}=2.3\cdot10^{-9}mbar\cdot l/s$ of BA_{END} by considering the value of P_{END} after NEG activation and the pumping speed $C_{ENTRANCE}$ of the aperture of the NEG chamber.

For every H_2 injection, pumping speed as seen at the end of the NEG chamber has been calculated dividing Q_{DEGAS}, which is constant, by the initial pressure value $P_{END,0}$ on BA_{END} before starting injecting H_2:

$$S_{BA_{END}} = \frac{Q_{DEGAS}}{P_{END,0}}$$
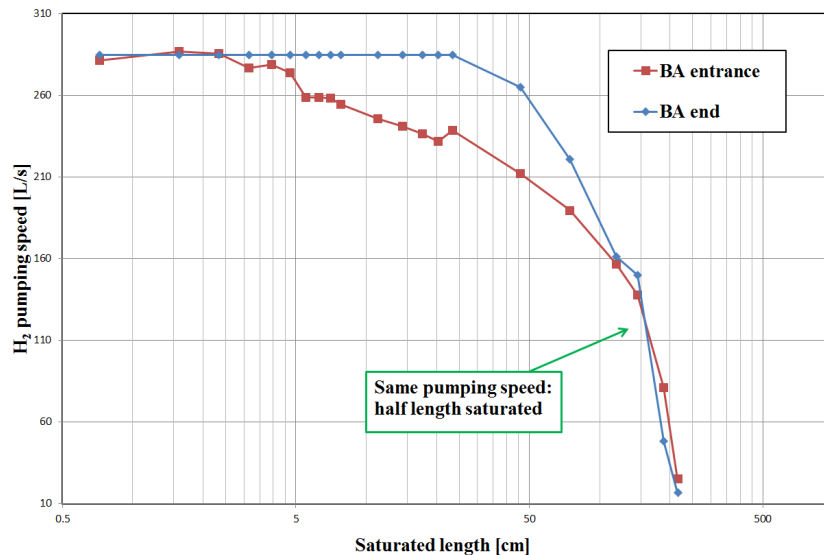
Figure 51 – H_2 pumping speed as function of the saturated length for the gauges $BA_{ENTRANCE}$ and BA_{END}.

It is interesting to notice that the pumping speed seen by the BA located at the end remains constant after even more than *50 cm* of NEG coated vacuum chamber result saturated.

The same graph also shows that both gauges are characterised by the same pumping speed when the saturated length corresponds to half of the total chamber's length.

8.2.5 Comparison between experimental data and MOLFLOW+ simulations

A CAD model of the experimental setup was created in order to simulate with MOLFLOW+ the effects of the progressive saturation of the NEG chamber. For simplicity reasons, the model includes only the *216 cm* long NEG coated vacuum chamber, the two elbows where the $BA_{ENTRANCE}$ and BA_{END} gauges are located and the half of the Fischer-Mommsen dome downstream of the inner conductance, which is used as injection point (Figure 52).
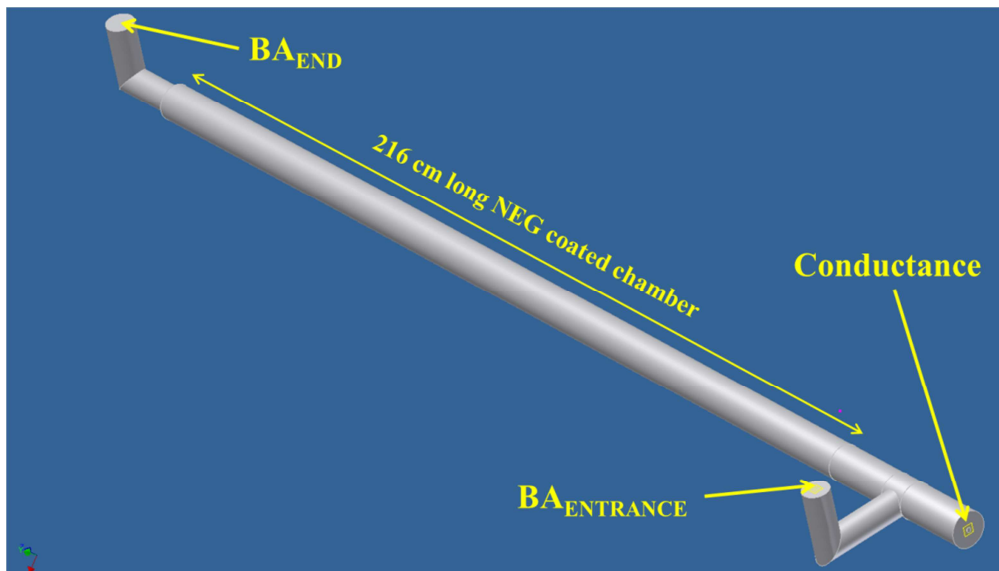

**Figure 52 – Orthographic view of the CAD model of the *2 m* long NEG coated vacuum system.**

Table 23 resumes the five different configurations that have been simulated: assuming that the NEG saturation front progressively moves along the flow direction, a NEG sticking factor $\alpha \neq 0$, ranging from 10^{-6} to *1*, has been applied on a gradually more and more limited pipe's wall area.

A sticking $\alpha = 0$, representing the already saturated coating, has been in turn assigned to the more and more large wall area starting from the entrance of the NEG vacuum chamber.

Table 23 – Saturated and activated NEG lengths of each MOLFLOW+ simulation.

Simulation	Saturated NEG length	Activated NEG length
1	0 cm	216 cm
2	17 cm	199 cm
3	74 cm	142 cm
4	140 cm	76 cm
5	188 cm	28 cm

For each of these configurations, H_2 injections were simulated assuming an incoming gas flow equal to $3 \cdot 10^{-7} mbar \cdot l/s$ and transmission, calculated as the ratio between the pressure values recorded in correspondence of $BA_{ENTRANCE}$ and BA_{END}, was plotted as a function of α. The results of these simulations are shown in Figure 53: as the saturated length increases, transmission for the same sticking factor decreases because more gas molecules are able to reach the end of the vacuum chamber without being absorbed, showing the same behaviour observed in the experimental measurements.
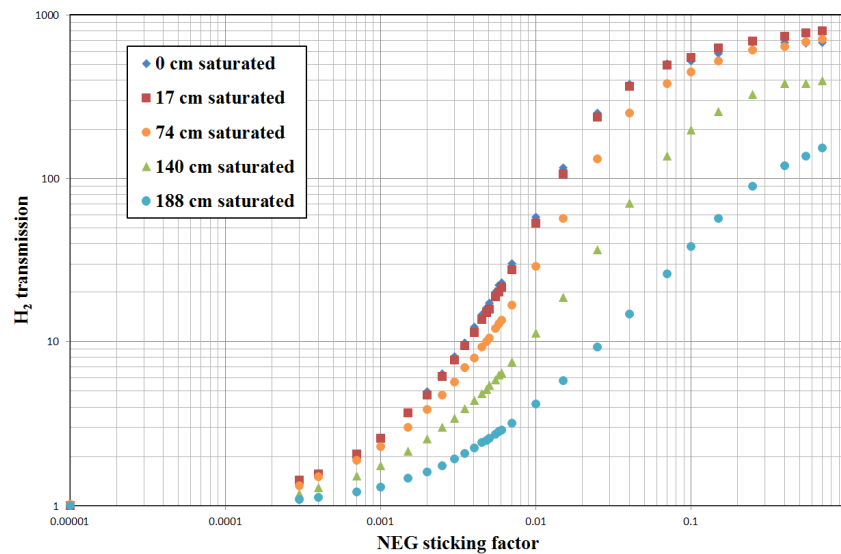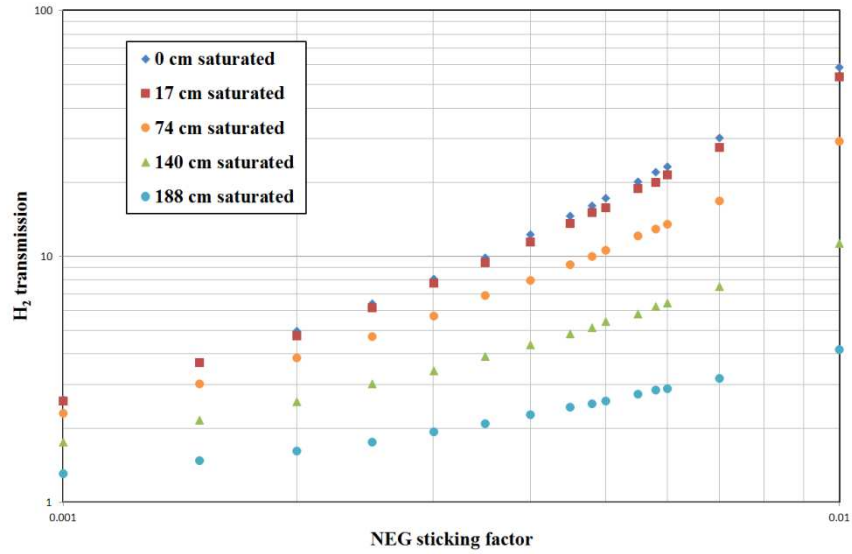

Figure 53 – Simulated H_2 transmission for different saturated lengths as a function of the NEG sticking factor $10^{-5} \leq \alpha \leq 1$.

It is possible to distinguish three areas:

– for $\alpha < 0.001$ transmission tends to *1* independently of the NEG saturated length;

– for $0.001 < \alpha < 0.01$ the largest transmission increases occur, even for small variations of the sticking factor;

– for $\alpha > 0.1$ transmission becomes more or less constant, especially for small NEG saturated lengths.

Figure 54 shows an enlargement of the same plot for sticking factors ranging between *0.001* and *0.01*, i.e. the most probable interval for real H_2 sticking factors.

Figure 54 – Simulated H$_2$ transmission for different saturated lengths as a function of the NEG sticking factor *0.001≤α≤0.01*.

Furthermore, the experimental measurements of H$_2$ transmission as a function of the saturated length have been compared with the results of these latter simulations. An error of the *20%* was taken into account for the experimental data due to the uncertainty in pressure measurement of the BA gauges.
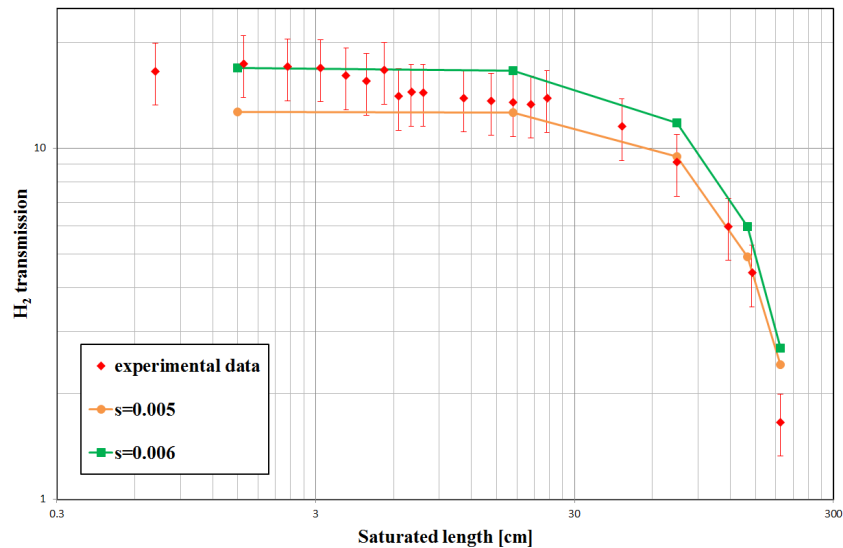
Figure 55 – Measured and simulated H$_2$ transmission as a function of the NEG saturated length.

Figure 55 clearly shows that the simulated values perfectly match the experimental data if the NEG sticking factor for H$_2$ is comprised in the range between *5·10^{-3}* and *6·10^{-3}*. This statement is in accordance with the results of previous studies, which measured a hydrogen

sticking coefficient of the same order of magnitude for a NEG surface with the same elemental composition [13] [22].

8.3   28 m LONG PILOT SECTOR

### 8.3.1   Bakeout and NEG vacuum activation of the pilot sector

In October 2011 a first bakeout and vacuum activation process was conducted in order to restore the NEG pumping properties in the pilot sector, which had been previously vented with air. Moreover, before starting saturation measurements, the pilot sector underwent a second complete bakeout and NEG vacuum activation process in January 2012, in order to ensure the best possible performances of the coating during the study.

In both cases, the bakeout and activation procedure habitually used for the LSS beam pipes at room temperature in the LHC was adopted. Table 24 reports the parameters that have been set during the process for the different components of the pilot sector.

Table 24 – Heating rate, maximum temperature and duration of every step of the bakeout/vacuum activation process, depending on the type of component involved.

		Bakeout	NEG activation	Cooling down
NEG coated vacuum chambers	Heating rate [°C/h]	50	50	80
	Maximum temperature [°C]	120	230	20
	Plateau duration [h]	24	24	24
Stainless steel components	Heating rate [°C/h]	50	50	50
	Maximum temperature [°C]	250	150	20
	Plateau duration [h]	24	24	24
NEG coated vacuum chambers	Heating rate [°C/h]	50	50	50
	Maximum temperature [°C]	180	250	20
	Plateau duration [h]	24	24	24
Stainless steel flanges on NEG coated vacuum chambers	Heating rate [°C/h]	50	50	50
	Maximum temperature [°C]	140	140	20
	Plateau duration [h]	24	24	24
RGAs and BA gauges	Heating rate [°C/h]	100	100	50
	Maximum temperature [°C]	350	180	20
	Plateau duration [h]	24	24	24

According to the procedure, before starting the NEG activation step, a degassing of all the gauges, RGAs and sputter-ion pumps installed on the system was performed, in order to reduce as much as possible any possible residual gas source in the pilot sector. During the entire process, due to the high pressures caused by the degassing of the inner walls, all the BA gauges were switched off and pressure data were collected by means of the Penning gauge installed in the central module.
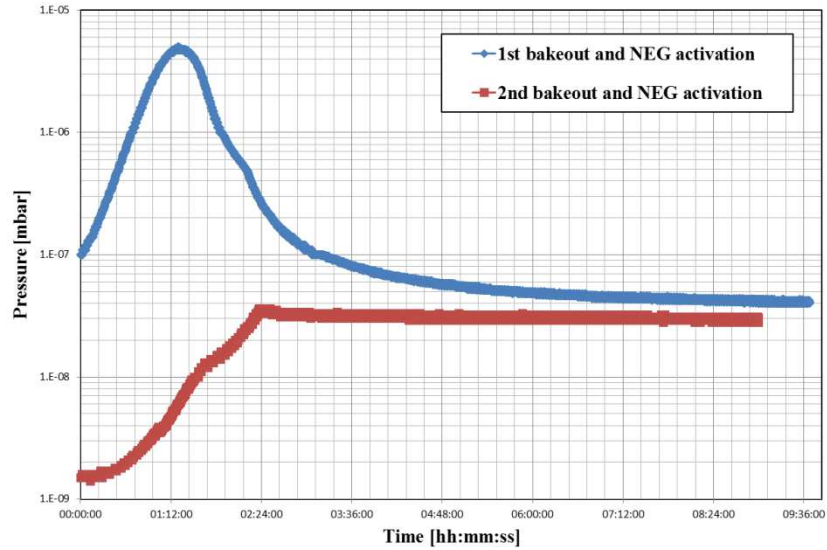
Figure 56 – Pressure variations recorded during the two NEG activations performed in the pilot sector.

Figure 56 reports the measured pressure trend during the NEG activation step for both cases, corresponding to the heating ramp of the NEG chambers from *120 °C* to *230 °C*. The first is characterised by the pressure peak typical of NEG activation, which usually appears when a temperature equal to *180 °C* is reached. This behaviour is due to the fact that, at lower temperatures, pressure is dominated by the outgassing of the saturated NEG coating and increases during the heating process. At *180 °C* the NEG becomes activated and therefore it starts to pump the residual H_2, thus lowering pressure into the system until a plateau is reached when temperature of the NEG chambers reaches the maximum, i.e. *230 °C*.
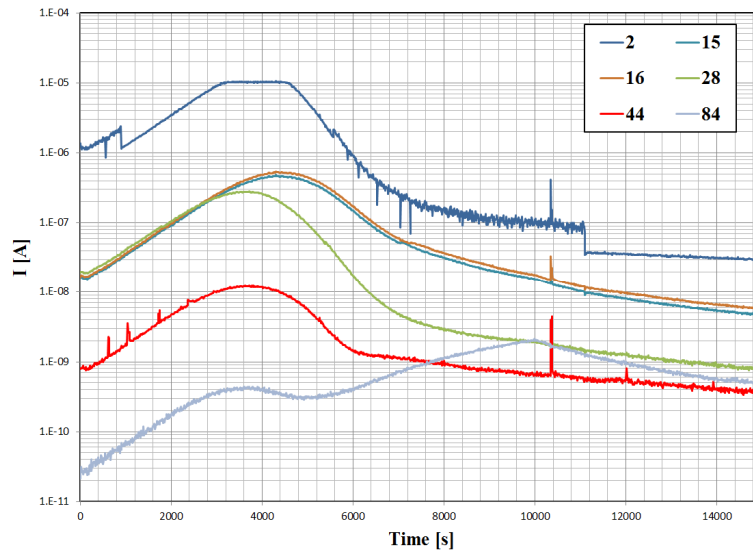
Figure 57 – Variation s of ion currents corresponding to different masses during the first NEG activation.

93

The second bakeout and NEG activation process instead was performed even if the pilot sector had already been activated in the previous occasion, without being afterwards exposed to air. This is clearly demonstrated by the second curve in the plot, which starts at *120 °C* from a much lower pressure value (about *$1\cdot10^{-9}$ mbar* instead of *$1\cdot10^{-7}$* mbar) and shows no peak, indicating that the NEG coating is already pumping. After having reached *230 °C*, the pressure plateau roughly corresponds to the one of the previous activation.

Finally, Figure 57 shows the RGA data collected by RGA_{CENTRE} during the first NEG activation for several currents corresponding to different gases.

The peak of the H_2 curve, which is not visible because the maximum value is over range, is reached as already said when the NEG coating is at about *180 °C*. It is possible to notice that not all the gases show the same behaviour: some currents start to decrease at lower temperatures (28 and 44, corresponding to CO and CO_2 respectively) and other at higher ones. In particular, 15 and 16 correspond to CH_4, which is not pumped by NEG; however, if H_2 pressure decreases, the production of CH_4 due to H_2 cracking on metallic surfaces also starts to decrease. CH_4 follows the trend of H_2. 84 is the mass of Kr, which is a noble gas and therefore is not pumped by NEG. The presence of Kr in the pilot sector is due to the fact that this gas is employed in the sputtering deposition of the NEG coating; as temperature increases during NEG activation, the degas of Kr increases, reaches a maximum and then stabilises after a certain time.

Finally, the ultimate lowest pressures measured at the end of the second bakeout and NEG activation are reported for the three BA gauges located along the pilot sector (Table 25). These values constitute a baseline for the pressures recorded during the saturation measurements that have been successively performed.

Table 25 – Lowest pressures measured on the three BA gauges at the end of the second bakeout and NEG activation process.

BA_{CENTRE}	BA_{JURA}	BA_{SALEVE}
$1.3\cdot10^{-11}$ mbar	$4.7\cdot10^{-12}$ mbar	$3.6\cdot10^{-12}$ mbar

Apart from pressure, it is also important to assess the gas density distributions inside the pilot sector, considering the NEG coated vacuum chambers completely activated. A VASCO simulation of the system was ran and the gas density profiles of H_2, CH_4, CO and CO_2 in *[molecules/m^3]* along the pilot sector were calculated (Figure 58).
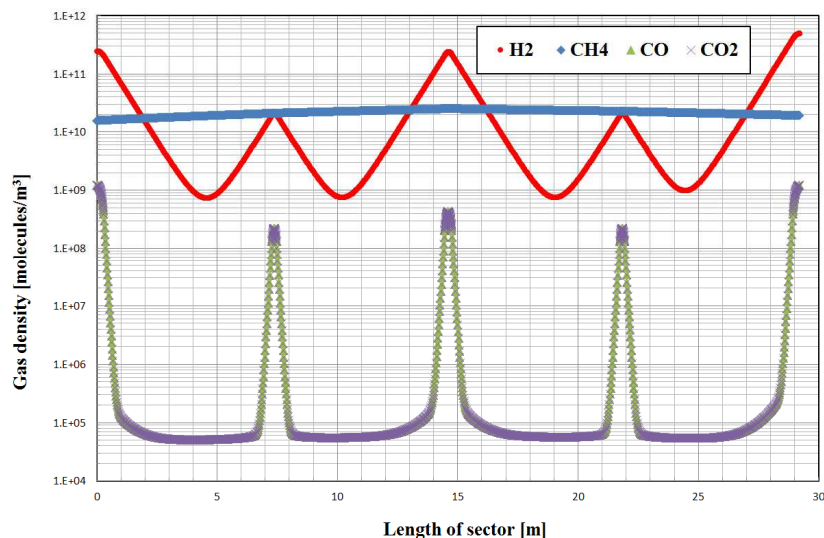
Figure 58 – VASCO simulation of gas density profiles inside the pilot sector after bakeout and NEG activation.

The simulation shows that H_2 is dominant in correspondence of the stainless steel modules, where also the gauges and the RGAs are located; H_2 density quickly decreases along the NEG coated chambers. CO and CO_2 are present in lower concentration and density peaks for these gases are again in correspondence of the modules; the decrease of density in this case is more prominent due to the high NEG sticking factor for these gases.

CH_4 is dominant in the NEG coated beam pipes and its profile is more or less constant because the sticking factor for this gas is very little. The density profile of CH_4 is parabolic due to the pumping provided by the two sputter-ion pumps located at the ends of the pilot sector.

Peaks on the right correspond to Salève side and are slightly higher with respect to Jura side because, due to the presence of the RGA, higher degassing rates were considered on Salève side. The same values of degassing rate were considered also in the centre, where another RGA is located, but gas densities here are lower due to the presence of NEG coated chambers on both sides of the central module.

8.3.2 Working procedure

The saturation of the pilot sector has been conducted similarly to that of the *2 m* long vacuum chamber, by means of several injections of CO. After every CO saturation, two small H_2 and N_2 injections were also performed, aiming to measure the variations of transmission, pumping speed and capture probability for each gas as functions of the NEG saturated length.

In addition, after every saturation a measurement of the degassing from the internal walls of the pilot sector was also performed. This was made possible by switching off the two sputter-ion pumps, every time for a fixed time interval equal to *1.5 h*.

The working procedure for everyone of these measurements has been analogous to the one employed for the *2 m* long vacuum chamber. The pressure data were collected using again the same Labview program, whereas the ion current data coming from the two RGAs were displayed by the software Quadstar32, especially conceived for these devices by the manufacturer. Before starting measurements, each mass channel of the RGA has always been accurately calibrated and the injection line cleaned, as already mentioned in the previous paragraphs.

Again, every gas injection was performed in steps by opening little by little the injection valve, waiting for pressures on the three gauges to stabilise around a certain value before opening again the valve.

Table 26 summarises how transmission, pumping speed and capture probability have been calculated, according to the description of the experimental setup reported in Chapter 7. Also in this case, *ΔP* for a given gauge refers to the difference between the measured pressure during the injection and the initial one.

Table 26 – Transmissions, pumping speed, capture probability and gas flow during degassing analysis calculated for the pilot sector.

	Units	Expression
Transmission Jura-side	[-]	$Tr_J = \dfrac{\Delta P_{CENTRE}}{\Delta P_{JURA}}$
Transmission Salève-side		$Tr_S = \dfrac{\Delta P_{CENTRE}}{\Delta P_{SALEVE}}$
Pumping speed (half sector)	[l/s]	$S_{1/2} = \dfrac{Q_{1/2}}{\Delta P_{CENTRE}} = \dfrac{1}{2} \cdot C_{TOT} \cdot \dfrac{\Delta P_{INJ} - \Delta P_{CENTRE}}{\Delta P_{CENTRE}}$
Capture probability	[-]	$\%CP_{1/2} = \dfrac{S_{1/2}}{C_{ENTRANCE}}$
Degassing flow	[mbar·l/s]	$Q_{DEGAS} = \dfrac{\Delta P_{CENTRE} \cdot V}{\Delta t}$

Due to the fact that the configuration of the *28 m* long pilot sector is symmetrical with respect to the central module in which gases are injected, the system can be considered as an assembly of two identical NEG coated beam pipes, each one *14 m* long.

For this reason, transmission has been calculated for both Jura and Salève sides. Pumping speed instead is calculated as $S_{1/2}$, referring to the pumping speed "seen" by each half of the pilot sector and obtained from $Q_{1/2}$, which is half of the total gas flow entering into the system (Figure 41). Similarly, also the percentage of capture probability $\%CP_{1/2}$ refers to half of the total length of the pilot sector.

Finally, the degassing flow Q_{DEGAS} obtained during degassing measurements is calculated by multiplying the pressure increase ΔP_{CENTRE} for the total volume *V* of the pilot sector, which is equal to *146.78 l*, and by dividing it by the switching-off time interval Δt of the sputter-ion pumps, which corresponds to *5400 s*.

The ultimate pressure values P_{INJ} in the injection line for every gas injection are reported in Table 27. Their choice is dictated by the same considerations about instability of the incoming gas flow at high pressures that have already been exposed in the description of the *2 m* long vacuum chamber. Again, due to the higher saturating capability of N_2, the injections of this gas have been performed in only one step and for maximum *4-5 minutes*.

Table 27 – Ultimate P_{INJ} pressure at the end of every injection in the pilot sector for the three gases of interest.

H_2	N_2	CO
$2 \cdot 10^{-5}$ mbar	$1 \cdot 10^{-4}$ mbar	$5 \cdot 10^{-4}$ mbar

8.3.3 Influence of CH_4 degassing of the Penning gauge

After having performed the first injections in the pilot sector, it was clear that the Penning gauge located on the injection line strongly affects the possibility to collect reliable transmission data during injections. As a matter of fact, when P_{INJ} increases, the Penning gauge starts to degas a certain amount of CH_4, which is not pumped by NEG and therefore results in a considerable pressure increase on both ends of the pilot sector, where BA_{JURA} and BA_{SALEVE} are located.

For these reasons, it was decided to keep the Penning gauge switched on only during H_2 and N_2 injection and to switch it off during CO injections, which are much longer (*2-8 hours*) and therefore could be more influenced by CH_4 desorption. Only the last two CO injections were

performed with the Penning gauge on because in these occasions the influence of CH_4 degassing was negligible.
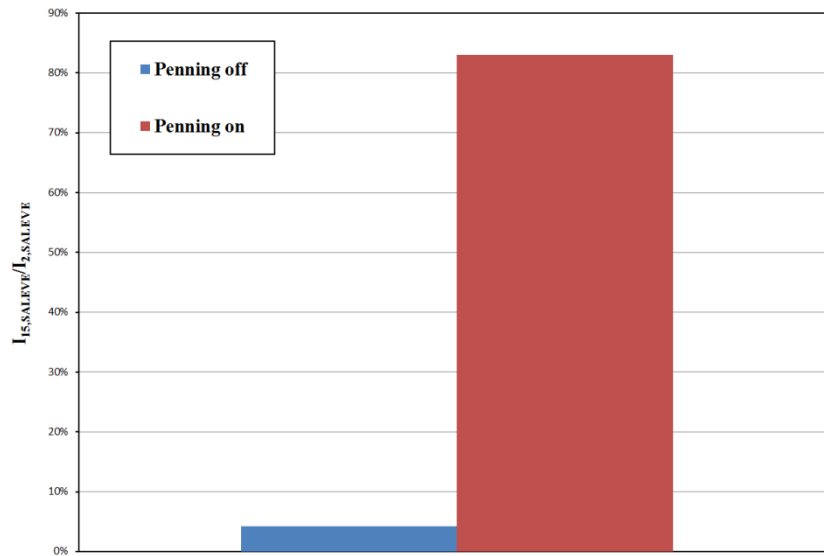
Figure 59 – I_{15}/I_2 measured by RGA$_{SALEVE}$ during two distinct H_2 injection, one with the Penning gauge on and the other not, for the same H_2 flow $Q=10^{-6}$ mbar·l/s.

The above-described effect due to the CH_4 degassing of the Penning gauge has been quantified by calculating the percentage ratio of I_{15} (representing CH_4) and I_2 (representing H_2) measured by RGA$_{SALEVE}$ during two distinct H_2 injection, one with the Penning gauge switched off and the other not, performed when the NEG in the pilot sector was still completely activated. For the same injection flow $Q=10^{-6}$ mbar·l/s, when the Penning gauge is off I_{15} is only about *4%* of I_2, while in the other case this ratio becomes 83% (Figure 59). The influence of CH_4 is very strong at the ends of the pilot sector, whereas it is negligible in the centre, where pressure is dominated by the injected gas flow: for the two same injections, I_{15} is *0.04%* of I_2 if the Penning is off and *1%* if the gauge is on.

8.3.4 Transmission, pumping speed and capture probability variations as functions of the NEG saturated length

As already explained, all the CO injections were performed with the Penning gauge in the injection line off, except for the first and the last two injections. For this reason, it is not possible to calculate precisely the injected gas flow if the Penning gauge is off and, consequently, to calculate the actual NEG saturated length for every injection.

The total amount of injected CO molecules and the NEG saturated length for every CO injection were therefore estimated by scaling the precise results of the last two injections and

by assuming that the number of CO molecules adsorbed per unit area by the NEG surface is the same of the *2 m* long vacuum chamber, i.e. *2.2·10^{15} molecules/cm^2*.

8.3.4.1 *H$_2$ transmission*

Figure 60 shows the variation of H$_2$ transmission as a function of the NEG saturated length in the pilot sector for both Jura and Salève sides. It is possible to notice that Tr$_{SALEVE}$ remains more or less constant until about *20 m* of NEG coating are saturated, while Tr$_{JURA}$ starts to decrease when about *15 m* are saturated, indicating that the NEG saturation has not been perfectly symmetrical in the two halves of the pilot sector.
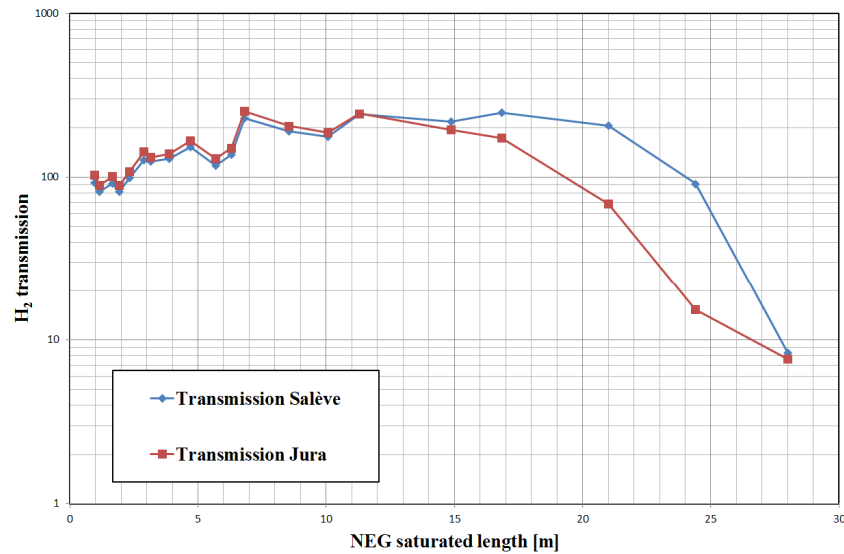
Figure 60 – H$_2$ transmission of both Jura and Salève side as a function of the NEG saturated length.

It is worth remembering that, as already explained in the previous paragraph, transmission measurements have been considerably influenced by the degassing of the Penning gauge. Figure 61 reports the ratio of the ion currents *I$_{15}$* and *I$_2$* (representing CH$_4$ and H$_2$, respectively) as a function of the NEG saturated length for both RGA$_{CENTRE}$ and RGA$_{SALEVE}$, measured for an injected H$_2$ flow *Q=10^{-6} mbar·l/s*: this ratio always remains more or less constant for the central RGA, whereas it decreases on Salève side as the NEG saturation progresses, confirming that *P$_{CENTRE}$* during injections is dominated by the injected gas, while the effects of CH$_4$, together with those of the progressive NEG saturation, are more evident at the ends of the pilot sector. The first two values of both curves are much lower because they were acquired with the Penning gauge off.
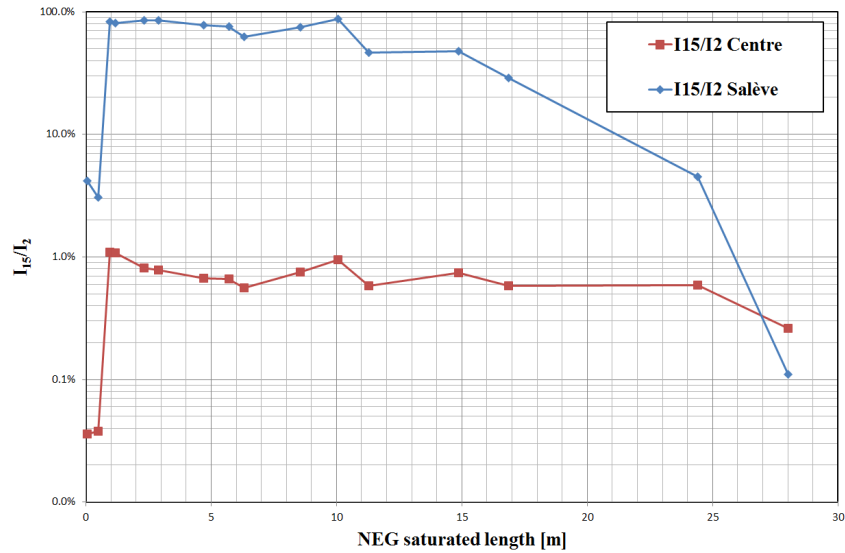
Figure 61 – Comparison between I_{15}/I_2 measured by RGA_{CENTRE} and RGA_{SALEVE} as a function of the NEG saturated length, for an injected H_2 flow $Q=10^{-6}$ mbar·l/s.

Figure 62 shows the evolution of the ion currents I_2 and I_{15} measured by RGA_{CENTRE} during the third (NEG coating still almost completely activated) and the last H_2 injections (NEG coating completely saturated), both performed with the Penning gauge on.
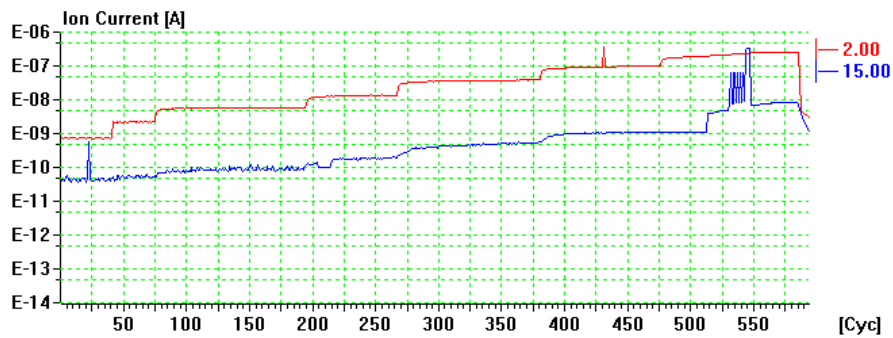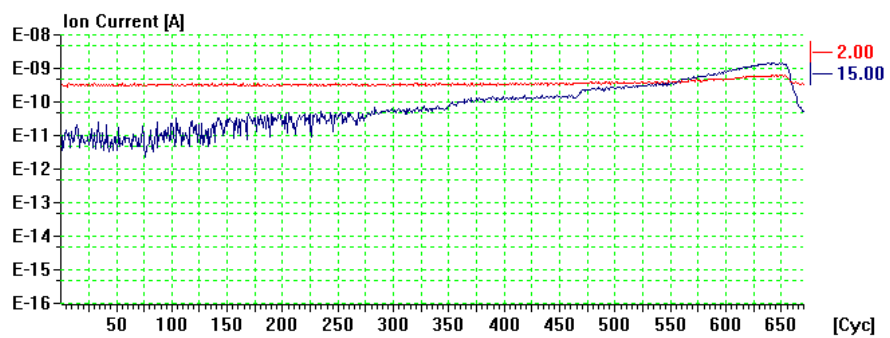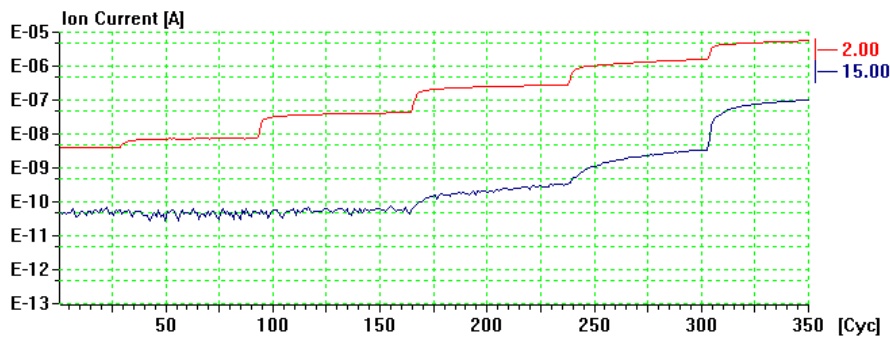

a)
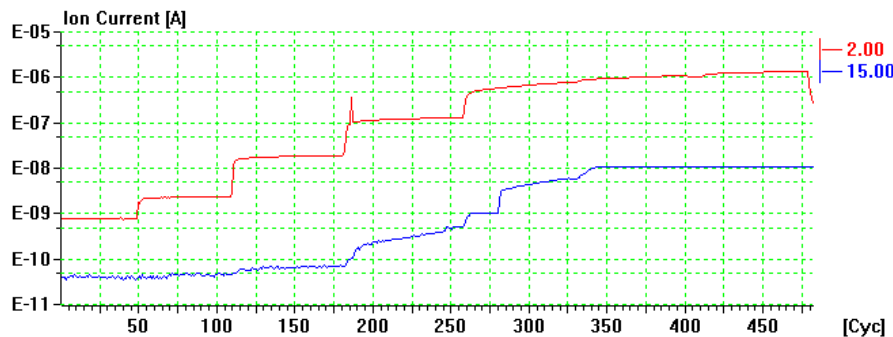
b)

Figure 62 – Variations of I_2 and I_{15} measured by RGA_{CENTRE} during: a) the third H_2 injection (*1 m* of NEG saturated in total), b) the last H_2 injection (*28 m* of NEG saturated).

100

In both cases, the ratio between the two currents is approximately the same and I_2 is much higher than I_{15} even when the NEG saturation is complete.

Figure 63 shows the same evolution relatively to the RGA located on Salève side: when the NEG coating is activated, I_2 remains constant during the injection because all the incoming H_2 molecules are adsorbed by the *14 m* of NEG between the injection valve and RGA$_{SALEVE}$. I_{15} progressively increases and, at the end of the injection, CH_4 becomes the dominating gas, thus influencing transmission that, without the pressure contribution of this gas, would be much higher. On the other hand, when the NEG coating is saturated, I_{15} still increases during the injection but P_{SALEVE} is always dominated by the contribution of H_2, which is no more adsorbed by NEG and can easily reach the ends of the pilot sector.

a)

b)

Figure 63 – Variations of I_2 and I_{15} measured by RGA$_{SALEVE}$ during: a) the third H_2 injection (*1 m of NEG saturated in total*), b) the last H_2 injection (*28 m of NEG saturated*).

Hence the ratio I_{15}/I_2 measured on Salève side progressively decreases as the NEG saturated length increases, because more and more H_2 is able to reach the ends of the pilot sector without being adsorbed by the NEG coating (Figure 64).
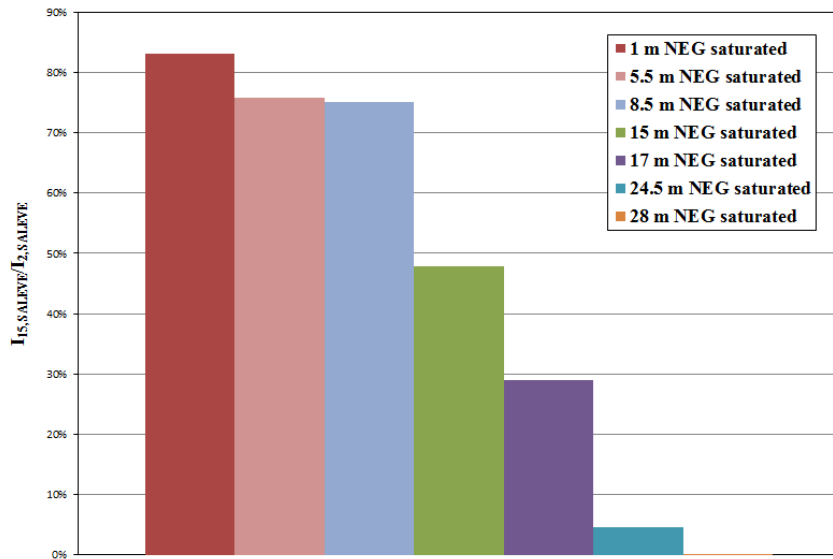
Figure 64 – I_{15}/I_2 **measured by RGA$_{SALEVE}$ as the saturation of the pilot sector progresses.**

These considerations could also explain why H_2 transmission seems to increase during the saturation of the first meters of NEG coating (Fig…): CH_4 partial pressure slightly decreases and H_2 one remains constant, so that the resulting transmission is increased. Afterwards, the progressively increasing amount of H_2 arriving at the ends of the pilot sector, due to the raised NEG saturated length, leads to a steady decrease of transmission.

Moreover, H_2 transmission measurements are affected also by the pumping contribution of the two sputter-ion pumps IP$_{JURA}$ and IP$_{SALEVE}$, situated at the ends of the pilot sector.
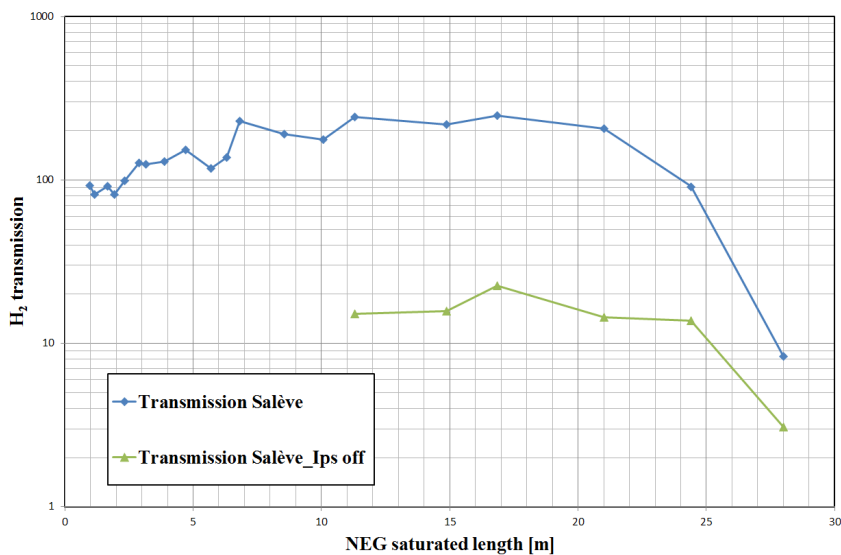

Figure 65 – Comparison between H_2 transmissions measured on Salève side with IP$_{SALEVE}$ on and off.

These two pumps have been constantly working during all gas injections, providing a crucial pumping capability for CH_4. In order to quantify their influence, Tr_{SALEVE} for H_2 has also been measured during the last step of every injection after having switched off the IP located on Salève side; data are available only for a saturated length higher than *10 m* (Figure 65).

It is worth underlining that it is much easier to recognise significant differences of transmission when the IP is turned on. As a matter of fact, in this case transmission variations for NEG saturated length comprised between *10 m* and *20 m* are of the order of *30-40*, whereas they become only *2-3* when the sputter-ion pump is switched off. This is due to the fact that, in this latter situation, CH_4 partial pressure at the ends of the pilot sector is very high and does not allow to see significant variations of H_2 pressure at these positions.

8.3.4.2 *CO transmission*

Figure 66 shows the variations of CO transmission for both sides of the pilot sector as functions of the NEG saturated length. In both cases, transmission remains constant until about *7 m* of the NEG chamber are saturated and then begins to gradually decrease.

Compared to the case of H_2, CO transmission is much higher, starting from a value of about $3 \cdot 10^4$ during the 2nd injection (when the NEG coating was almost completely activated), because all CO injections, except for the first, have been performed with the Penning gauge on the injection line switched off, leading to a negligible contribution of CH_4 to the total pressure at the ends of the pilot sector during the injections.
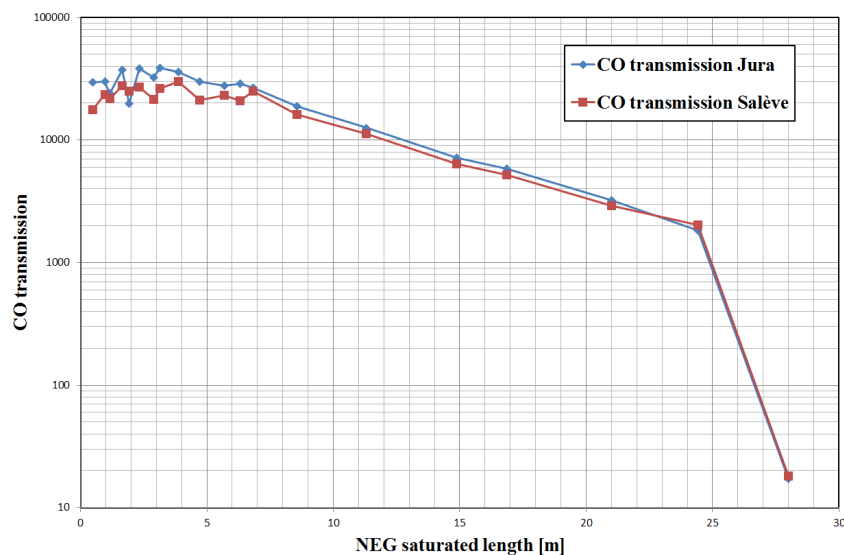

Figure 66 – CO transmission of both Jura and Salève side as a function of the NEG saturated length.

However, the first CO injection performed with the Penning gauge on is characterised by a transmission value (which is not plotted in the graph) of about *3000* on both sides, which is still considerably higher than the corresponding initial H_2 transmissions (about *100*). This is due to the fact that, as already mentioned for the *2 m* long vacuum chamber, NEG sticking factor for CO is much higher than the one for H_2 and thus, when the pilot sector is completely activated, CO molecules can reach its ends only thanks to the so-called *beaming effect*, i.e. by travelling along the pilot sector axis without colliding with its walls.

8.3.4.3   *Pumping speeds and capture probabilities*

Figure 67 shows the measured pumping speed $S_{1/2}$ of H_2, N_2 and CO for half of the pilot sector as functions of the NEG saturated length, compared with the corresponding effective pumping speeds, which are calculated analogously to the case of the *2 m* long vacuum chamber.
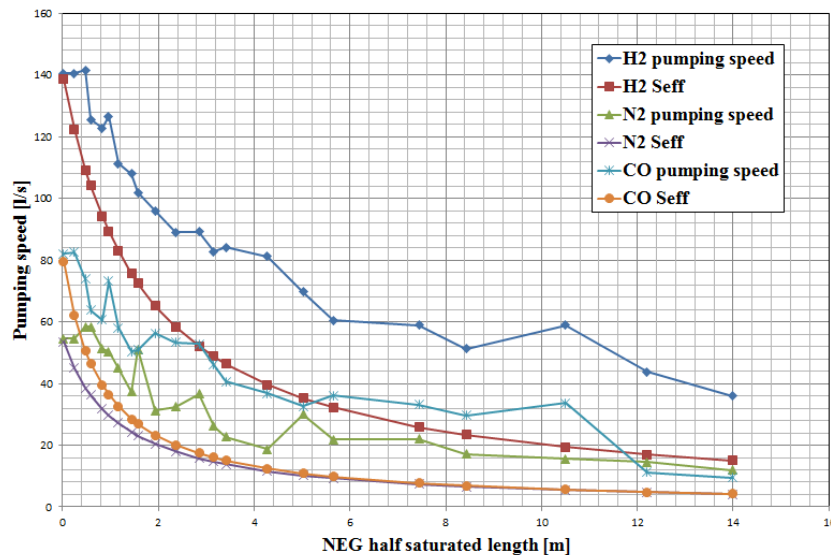

Figure 67 – Comparison between pumping speed and effective pumping speed for H_2, N_2 and CO.

The behaviour is the same already observed for the previous measurements, with S_{EFF} (calculated with a simple scaling of conductances) underestimating the measured values.

Figure 68 instead reports the trends of capture probability for the three gases, again referring to half of the pilot sector. The values for each gas are determined by their respective sticking factors: the higher is α, the higher the capture probability.
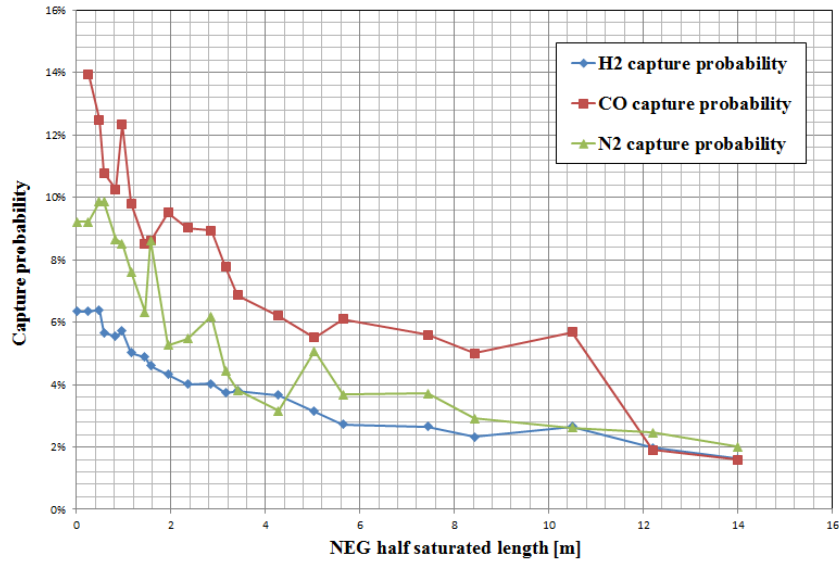
Figure 68 – Percentage of capture probability for H_2, N_2 and CO.

8.3.5 Degas analysis

Figure 69 shows the results of the degas analyses: the degassing flow Q_{DEGAS} in *[mbar·l/s]* is derived for both ΔP_{CENTRE} and ΔP_{SALEVE} and plotted as a function of the NEG saturated length. As already said, these measurements were conducted by switching off the two sputter-ion pumps located at the ends of the pilot sector for *1.5 h*, without injecting any gas. Each value of Q_{DEGAS} was calculated at the end of this time interval and represents the quantity of residual gas that has been desorbed per unit time by the internal walls of the pilot sector while the IPs were off and only the NEG coating was pumping.
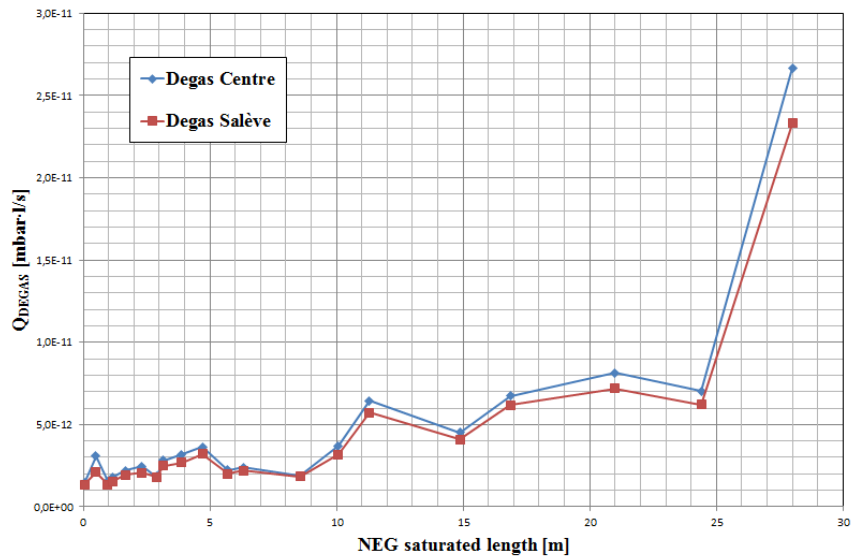

Figure 69 – Q_{DEGAS} as a function of the NEG saturated length, calculated for both ΔP_{CENTRE} and ΔP_{SALEVE}, 1.5 h after having turned off the two sputter-ion pumps.

The possible sources of CH_4 are mainly represented by the stainless steel surface of the modules, by the copper RF inserts and by the BA gauges and RGA filaments. Also the NEG coated surfaces constitute a possible source of this gas.

Table 28 shows the calculated values of CH_4 degassing characterising the different materials of the inner surfaces of the pilot sector. As the saturation progresses, Q_{DEGAS} for the stainless steel modules and the copper inserts remains constant, whereas the CH_4 degassing flow of the saturated NEG is about two orders of magnitude larger than the one for the activated NEG.

Table 28 – CH_4 degassing flow of the inner surfaces of the pilot sector.

Q_{DEGAS} [mbar·l/s]			
Stainless steel	**OFC copper**	**Activated NEG**	**Saturated NEG**
$1 \cdot 10^{-15}$	$1 \cdot 10^{-17}$	$1 \cdot 10^{-18}$	$9 \cdot 10^{-17}$

In Figure 70 it is possible to see the pressure increases due to CH_4 degassing for different NEG saturated lengths, calculated in P_{CH4} eq. The contributions of stainless steel modules, copper inserts and RGA and BA gauges remain constant; the one due to the activated NEG instead decreases because the NEG activated area progressively decreases, whereas the NEG saturated surface increases and thus its pressure contribution also increases.
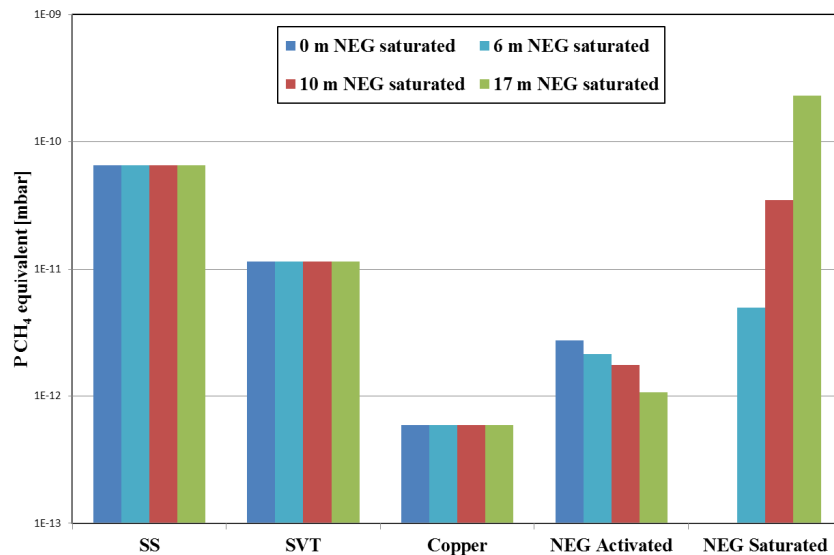

Figure 70 – Pressure increases due to CH_4 degas of different inner surfaces of the pilot sector as functions of the NEG saturated length.

The difference between the degassing flow measured in the centre of the pilot sector and at the end of Salève side, as expected, is negligible. As a matter of fact, during these analyses no

gas was injected in the system and the main responsible for the recorded pressure increases is CH_4, which is not pumped by NEG and therefore can easily reach the ends of the pilot sector, even if the NEG coating is still partially activated.

This is confirmed by comparing, for each degas analysis, Q_{DEGAS} and the variations of the ion currents I_2 and I_{15} registered by RGA_{SALEVE} (Figure 71): the evolution of Q_{DEGAS} perfectly follows that of ΔI_{15}.
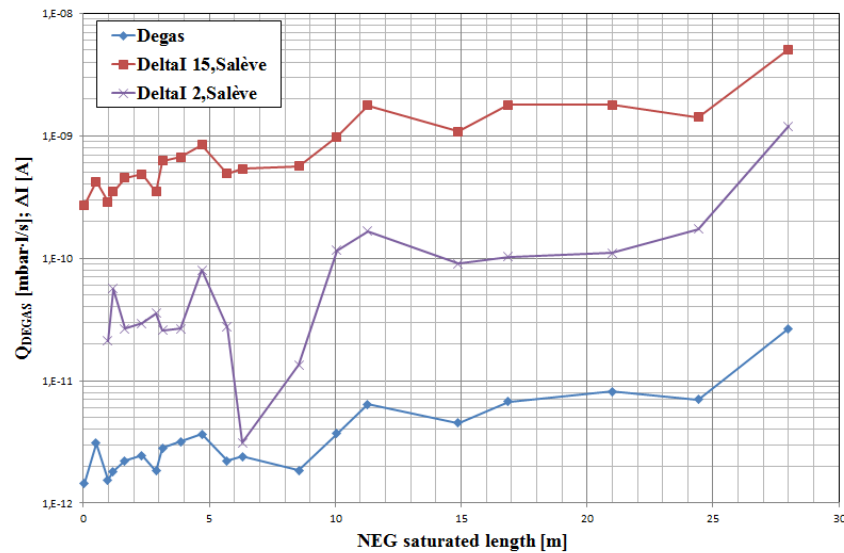
Figure 71 – Comparison between Q_{DEGAS} and ΔI for masses 2 and 15 measured by RGA_{SALEVE}.

Table 29 instead reports the initial and final ion currents for masses 2 and 15 measured by RGA_{SALEVE} during five degas analyses corresponding to different NEG saturated lengths.

When the sputter-ion pumps are off, I_{15} always increases of about two orders of magnitude and CH_4 becomes the dominant residual gas, while the partial pressure of H_2 remains unvaried.

Table 29 – Ion currents for masses 2 and 15 measured by RGA_{SALEVE} at the beginning and at the end of five different degas analyses, corresponding to five different NEG saturated lengths.

Saturated length [m]	$I_{2,START}$ [A]	$I_{2,END}$ [A]	$I_{15,START}$ [A]	$I_{15,END}$ [A]
0	$2.3 \cdot 10^{-10}$	$2.3 \cdot 10^{-10}$	$2.8 \cdot 10^{-12}$	$2.7 \cdot 10^{-10}$
3.2	$4.5 \cdot 10^{-10}$	$4.8 \cdot 10^{-10}$	$4.4 \cdot 10^{-12}$	$6.3 \cdot 10^{-10}$
10	$4.6 \cdot 10^{-10}$	$5.8 \cdot 10^{-10}$	$3.0 \cdot 10^{-12}$	$9.8 \cdot 10^{-10}$
24.4	$4.9 \cdot 10^{-10}$	$6.6 \cdot 10^{-10}$	$4.7 \cdot 10^{-12}$	$1.4 \cdot 10^{-9}$
28	$2.9 \cdot 10^{-9}$	$4.1 \cdot 10^{-9}$	$1.4 \cdot 10^{-11}$	$5.1 \cdot 10^{-9}$

The contribution of H_2 partial pressure becomes more significant only when the NEG coated surfaces are completely saturated, but also in this case the largest contribution to pressure increase in the pilot sector is due to CH_4 degassing.

These analyses, however, show that the degassing flow does not increase very much as the NEG saturation progresses but always remains more or less constant.

The amount of Q_{DEGAS} is limited, ranging between $1 \cdot 10^{-12}$ *mbar·l/s* (when the NEG is completely activated) and $7 \cdot 10^{-12}$ *mbar·l/s* (when more than *24 m* of the pilot sector are saturated). These small increases as function of the NEG saturated length may be due to the fact that a saturated NEG surface has a higher degassing rate of CH_4 with respect to an activated one. However, these variations are very small and only when the pilot sector is totally saturated Q_{DEGAS} considerably increases, with a value of about $2.5 \cdot 10^{-11}$ *mbar·l/s*.

8.3.6 Feasibility of MOLFLOW+ simulations

MOLFLOW+ simulation were conducted in order to calculate H_2 transmission on both sides of the pilot sector as a function of the NEG sticking factor and of the NEG saturated length.

Due to the length of the pilot sector, running this kind of simulations becomes extremely difficult because, especially if NEG is completely activated, only very few molecules are able to reach the end of the pilot sector without being adsorbed by the coating. In order to obtain reliable pressure and thus transmission values from the simulations, an adequate number of molecules should be injected in order to have a sufficient amount of molecules reaching the ends of the system. For the same reason, the number of injected molecules should increase as the NEG activated length increases, because this means that fewer molecules are able to reach the ends. On the other hand, this need results in a very long time for the completion of every simulation.

For these reasons, it was decided to run simulations starting from the opposite situation, i.e. from the situation in which the NEG chamber is almost completely saturated. In order to minimise the time needed for each simulation, a server with *16* CPUs was employed to run the program.
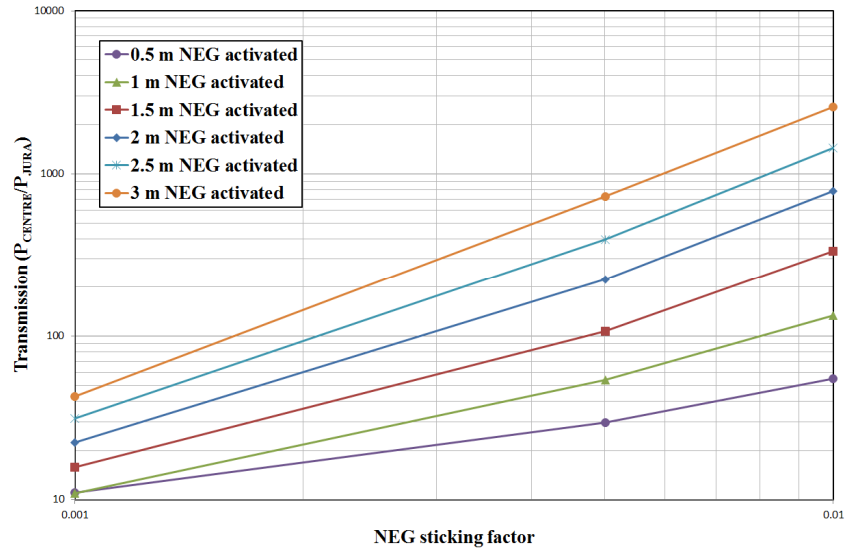
Figure 72 – MOLFLOW+ simulations of Tr$_{JURA}$ as a function of the NEG activated length (lengths refer to a single side of the pilot sector, thus each represents half of the total NEG activated length).

Figure 72 shows the results of these simulations: Tr$_{JURA}$ is plotted as a function of the NEG sticking factor for H$_2$ for different saturated lengths. The results obtained for Tr$_{SALEVE}$ are very similar due to the symmetrical geometry of the pilot sector.

The simulations were performed considering an injected H$_2$ flow equal to *3·10^{-7} mbar·l/s*, as it was for the case of the *2 m* long vacuum chamber. CH$_4$ degassing from stainless steel modules and gauges was omitted for simplicity.

However, in spite of the adopted solutions, the time needed for each simulation was still high and increased as the NEG saturated length decreased.

The last performed simulation, corresponding to *α=0.01* and *3 m* of activated NEG on each side, took about *30.5 h* for completion.

9. APPLICATIONS TO THE LHC

The measurements performed on the experimental test benches situated at CERN in Building 113 and described in the previous chapter were focused on the possibility to find a feasible method, based on the observation of the NEG pumping properties' variations, for a correct estimation of NEG saturation levels in the LHC sectors where this material is extensively employed.

The tests conducted on the *28 m* long pilot sector show that the best estimation of NEG pumping properties can be obtained by injecting CO, that gives more precise transmission measurements compared to H_2.

However, CO injections in the room temperature sector of the LHC must be avoided because they would saturate the NEG coating, whereas H_2 does not cause this inconvenient. Moreover, due to technical, logistical and safety reasons, it is not possible to install injections lines on the LHC vacuum sector and to store CO bottles in the accelerator's tunnel.

A source of H_2 instead can be obtained simply by heating small NEG cartridge installed along the LHC, without any need of injections line, due to the fact that the equilibrium pressure of H_2 in a system increases as temperature increases, according to Sievert's law.

On the other hand, degas analyses cannot constitute a feasible and practical option for the estimation of NEG saturated lengths in the LHC because, as already mentioned, Q_{DEGAS} increases very moderately as NEG saturation progresses and its values are always very small.

Moreover, even if the sputter ion pumps installed in the LSS room temperature were off, the Penning gauges located near the sector valves would provide a limited (about *1 l/s* for each gauge) pumping speed for CH_4, thus altering the results of degas analyses.

For these reasons, H_2 was chosen as reliable gas and transmission measurements were conducted in the LSS room temperature vacuum sectors and in CMS NEG coated beam pipes. The results are exposed in the next paragraphs.

9.1 ESTIMATION OF NEG SATURATION IN THE LSS VACUUM SECTORS

The LHC started operations in November 2009 and pressure increases have been measured ever since in different areas of the LSS vacuum sectors at room temperature.

These pressure variations are caused by beam-induced desorption of residual gases during beam operation. As a matter of fact, with high-intensity proton beam, stimulated degassing in the room temperature sectors of the LSS from the non NEG-coated components (cold-warm transitions, collimators, beam monitors) can determine a partial saturation of the NEG coated vacuum chambers.

Table 30 reports the pressures measured in four different vacuum sectors in February 2009 (just after NEG vacuum activation) and during the technical stop in March 2012 (after the 2011 high-intensity proton beam physics run). All data were taken without beam circulating (static vacuum conditions).

Table 30 – Pressure variations measured in four different sectors of the LSS at room temperature.

Vacuum sector	Pressure [mbar]		ΔP [mbar]
	February 2009	March 2012	
B5R7.R	$1.9 \cdot 10^{-10}$	$1.6 \cdot 10^{-9}$	$1.4 \cdot 10^{-9}$
B5L7.R	$1.2 \cdot 10^{-10}$	$9.6 \cdot 10^{-10}$	$8.4 \cdot 10^{-10}$
A5R5.B	$2.3 \cdot 10^{-11}$	$1.9 \cdot 10^{-10}$	$1.7 \cdot 10^{-10}$
A5L5.R	$2.7 \cdot 10^{-11}$	$1.6 \cdot 10^{-10}$	$1.3 \cdot 10^{-10}$

In particular, NEG conditions in the A5R5.B vacuum sectors have been investigated. The NEG coated beam pipes of this sector have a total length of *16 m* and the major residual gas source is represented by a collimator, which is located at *2 m* from the BA gauge that measured the reported pressure variation (Figure 73).
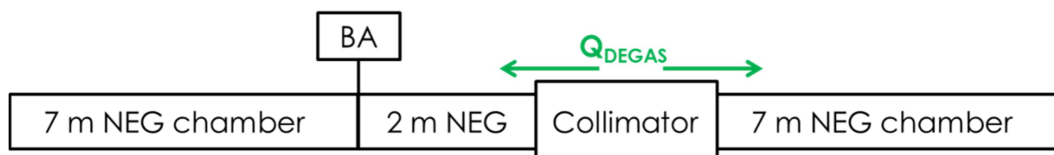
Figure 73 – Schematic view of A5R5.B vacuum sector.

Due to their analogous geometries, the estimation of the NEG saturation level in this *2 m* long chamber can be compared with the calculations made for the *2 m* long NEG coated vacuum chamber and presented in the previous chapter.

The collimator's degassing flow $Q_{DEGAS}=5.8 \cdot 10^{-9}$ *mbar·l/s* seen by the gauge can be found according to the following equation:

$$Q_{DEGAS} = S_{NEG,2009} \cdot P_{2009}$$

where P_{2009} is the pressure measured by the gauge in February 2009 and $S_{NEG,2009}=250$ *l/s* is the initial NEG pumping speed, corresponding to the one measured in the *2 m* long vacuum chamber when the NEG coating was completely activated.

By assuming that the thermal degassing Q_{DEGAS} is constant in static vacuum conditions, it is possible to determine the actual NEG pumping speed $S_{NEG,2012}=30$ *l/s* seen by the BA gauge:

$$S_{NEG,2012} = \frac{Q_{DEGAS}}{P_{2012}}$$
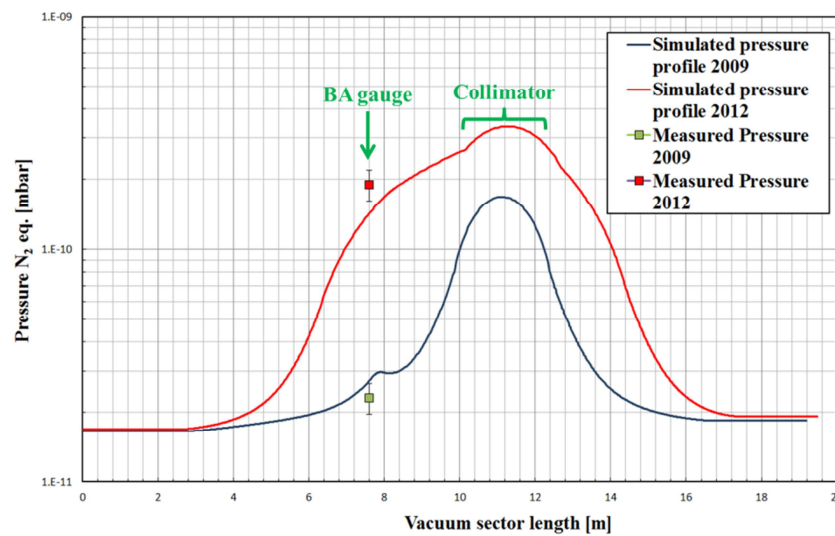
Figure 74 – VASCO simulation of the pressure profile in the A5R5.B sector, calculated for the entire NEG coated length activated (February 2009) and for *7 m* of NEG coated bema pipes saturated (March 2012).

Finally, by comparing the resulting percentage of lost pumping speed with the experimental data for the *2 m* long vacuum chamber (Figure 48), it is possible to estimate the NEG saturated length in the A5R5.B vacuum sector, which is equal to about *3.5 m* on both sides of the collimator.

VASCO simulations of the residual gas density profile in the same vacuum sector confirm this result. The so-obtained pressure profiles, which were simulated taking into account the estimated variation of the NEG activated length, are in good agreement with the pressure values measured by the BA gauge installed in the vacuum sector (Figure 74).

9.2 NEG QUALIFICATION OF CMS BEAM PIPES

NEG coatings are extensively used in the LSS of the LHC, which serve as experimental and utility insertions, in order to maintain the design pressure during beam operation.
In particular, LSS5 is located in correspondence of the cavern where the CMS detector is housed (Figure 75).
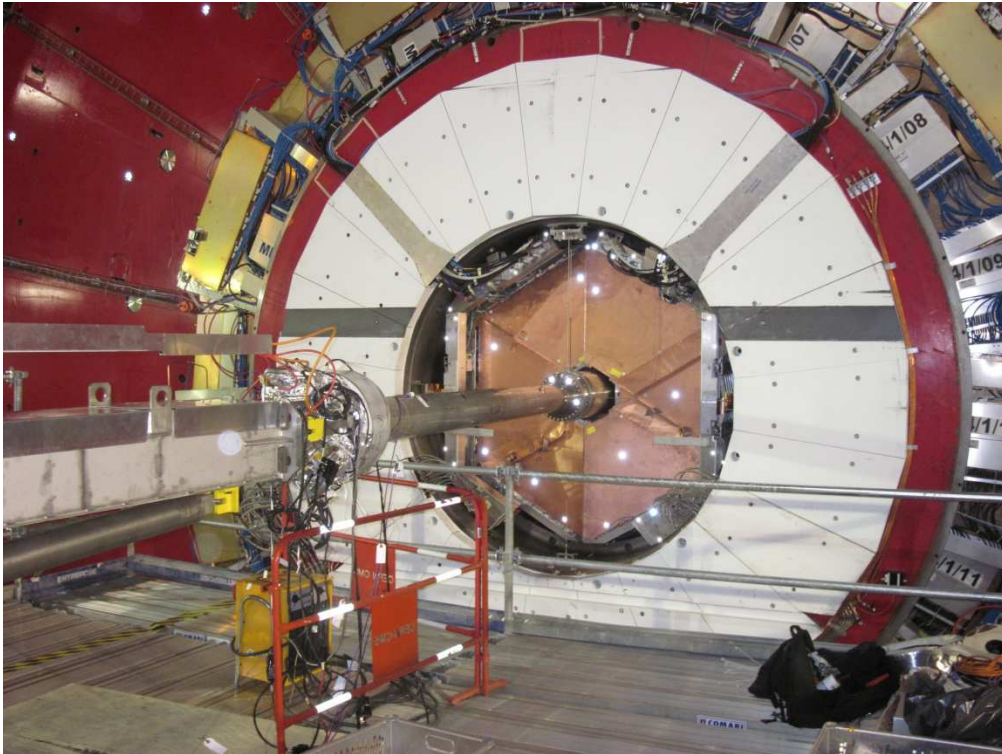

Figure 75 – View of the right side of CMS interaction point, with the NEG coated beam pipe entering the detector.

During the LHC physics run in 2011, unexpected pressure spikes appeared from time to time at *18.3 m* on the right side of CMS interaction point (IP). In some cases, the high background due to the pressure increase (up to 10^{-6} *mbar*) did not allow CMS to take data.
During the winter technical stop 2011-2012, X-ray imaging of the forward module located at *18.3 m* from the IP showed a non-conforming RF insert (Figure 76). The RF inserts are

employed along the LHC vacuum beam pipes in order to ensure electrical continuity to the beam in correspondence of bellows or cross-section area variations.

The origin of this non-conformity, overrunning the maximum allowed installed length of the module, is supposed to be due to the Target Absorber Secondaries (TAS) module movement by *17 mm* forward the tunnel [32].

<div align="center">a)   b)</div>
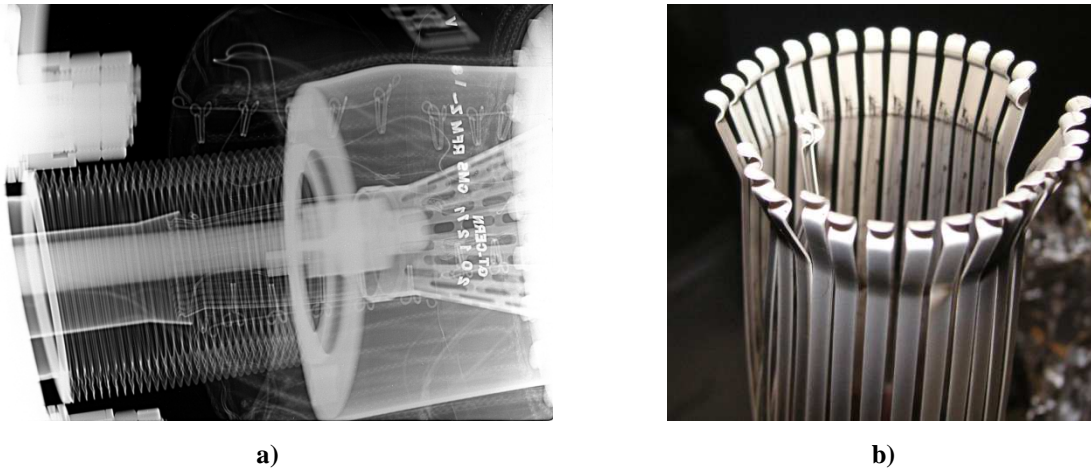
Figure 76 – a) Imaging of the non-conforming module with RF insert inside. b) Demounted RF insert.

Following the imaging, the exchange of the RF insert inside the module was scheduled. This operation normally implies an air venting of the NEG coating in the IP, thus consequently requiring a full bakeout and vacuum activation of the vacuum chambers located in the CMS vacuum sector. This approach would have required the complete opening of the detector and therefore it has been discarded due to time constraints.

In order to avoid this inconvenience, it was decided to exchange the RF insert under a constant flow of pure neon [33]. This method allows mechanical interventions while preventing the saturation of the vacuum activated NEG coating: the vacuum beam pipes are over-pressurized with a noble gas that is not pumped by NEG, thus avoiding air back streaming through the beam pipe aperture and saturation of the coating.

The exchange intervention was performed on the 18th of January 2012 following this working sequence:

- fill the beam pipe with ultra-pure neon with an initial overpressure of *200 mbar* above atmospheric pressure;
- open the module with the non-conforming RF insert while flushing ultra-pure neon through the beam pipes;
- exchange the RF contact and reinstall the module;
- pump down the vacuum sector and perform a partial bakeout and NEG reactivation.

After pumping down for *48 h*, pressure in the IP was in the *10^{-9} mbar* range, confirming that the NEG vacuum chambers were still activated.

A partial bakeout was afterwards performed because, during the RF insert exchange, the forward and TAS NEG coated chambers were completely saturated, the first due to its complete exposal to air and the latter due to the direction of pump down. Moreover, a bakeout was needed for the newly installed RF insert.

After having performed this partial bakeout, the final pressure at room temperature all along the beam pipes in the CMS interaction point was in the low *10^{-10} mbar*.

Finally, in order to test the NEG performances and to confirm the restored pumping properties of the coating, especially in the CT2 NEG chamber and in the beryllium central beam pipe, H_2 transmission measurements along the CMS vacuum sector were conducted after the RF insert exchange and after the subsequent partial bakeout, respectively. The results of these measurements were analysed and compared with VASCO simulations.

The source of H_2 for this purpose was a NEG cartridge installed in the forward module at *18 m* on the right of the IP (Figure 77).


Figure 77 – NEG cartridge used as H$_2$ source for transmission tests along the CMS vacuum sector.

The NEG cartridge was heated at about *450 °C*, thus establishing an increased equilibrium pressure for H_2 according to Sievert's law. During this process, H_2 was the gas mainly desorbed by the already activated NEG cartridge, while the release of CO, CO_2 and CH_4 was four orders of magnitude lower and could come from the degassing of the stainless steel housing of the NEG disks. CH_4 instead, which is not pumped by NEG and therefore could false the transmission tests, could also result from the cracking of H_2 molecules in the vacuum gauges.

9.2.1 CMS vacuum beam pipes

Figure 78 shows in details the CMS vacuum beam pipes on the right of the IP, with highlighted the area subjected to the RF insert exchange and to the subsequent partial bakeout. The beam pipe's structure is symmetrically the same on the left side of the IP.
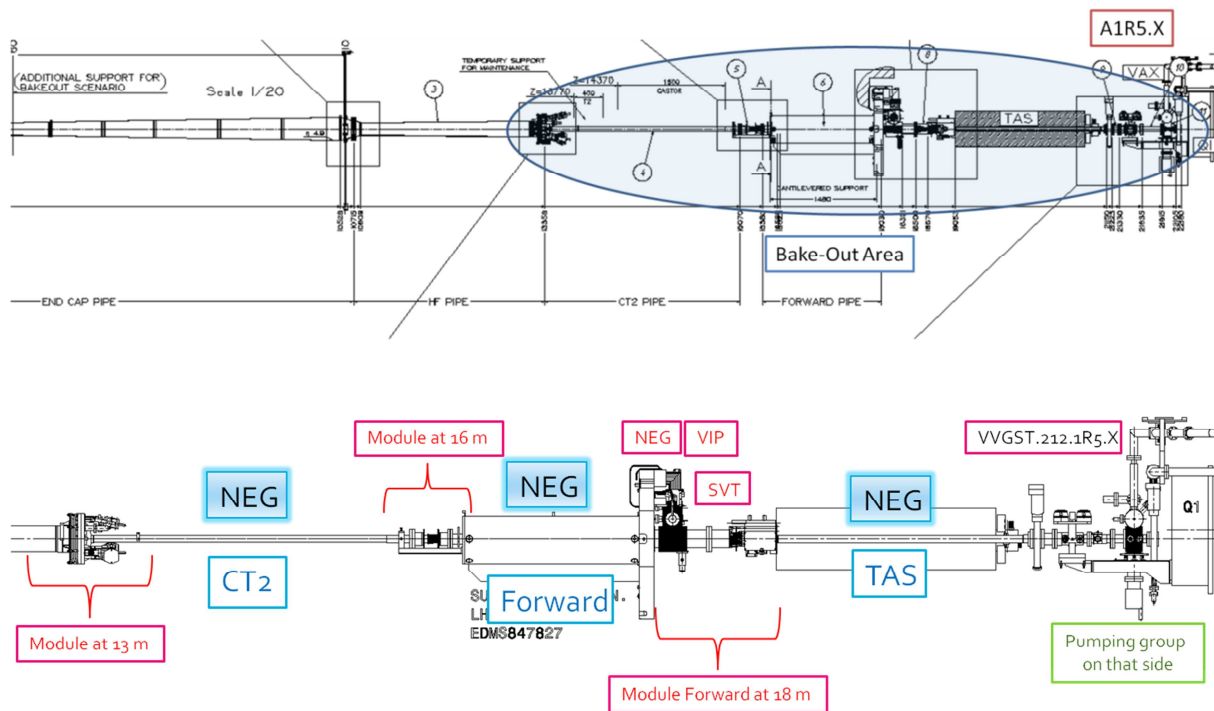
Figure 78 – Detailed view of CMS vacuum beam pipes and of the area subjected to bakeout (right side of CMS interaction point).

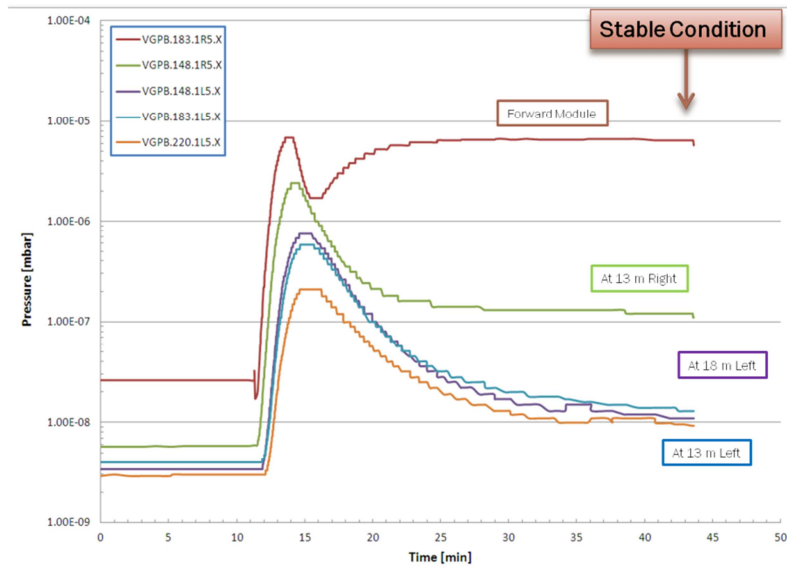### 9.2.2 Transmission test after the RF insert exchange

The first transmission test was performed *48 h* after the RF exchange.

The tests were conducted with the TMP in the vacuum sector A1R5.X connected to the vacuum beam pipe and with just the sputter-ion pump at *18 m* on the left side of the IP switched on, in order to decrease pressure (still dominated by neon used during the exchange of the RF insert) and to gain a better sensibility.

Pressure measurements during the test were taken by the following gauges, uniformly distributed along the beam pipes:

- VGPB.183.1R5.X, located in the same vacuum dome of the NEG cartridge, at *18 m* on the right side of the IP;
- VGPB.148.1R5.X, at *13 m* from IP on the right side;
- VGPB.183.1L5.X at *18 m* from IP on the left side;
- VGPB.148.1L5.X at *13 m* from IP on the left side.

Figure 79 shows the pressure evolution in the CMS beam pipe during transmission test. The first pressure increase in the forward module is due to the degassing of H_2, CH_4, CO and CO_2 from the NEG cartridge when the activation process is started; the pressure the recovers quickly and stabilizes to a fix value when the bulk material of the NEG cartridge is heated and the pressure increase is mostly due to H_2, according to Sievert's law.

**Figure 79 – Pressure increase during the H_2 transmission test after the RF insert exchange.**

Table 31 reports the pressure values recorded by the gauges all along the CMS beam pipes and the transmission ratios between the gauge located in the same vacuum dome as the NEG cartridge and each one of the other gauges. It is worth to notice that the farer is the position of the vacuum gauge with respect to the H_2 source, the lower is the recorded pressure increase: this clearly confirms the presence of a distributed pumping all along the NEG coated vacuum beam pipes.

Table 31 – Pressure and transmission ratio during the H_2 transmission test after the RF insert exchange.

Gauge position	Pressure [mbar]	Transmission ratio
18 m right side	$6.4 \cdot 10^{-6}$	1
13 m right side	$1.2 \cdot 10^{-7}$	53
13 m left side	$1.4 \cdot 10^{-8}$	457
18 m left side	$1.1 \cdot 10^{-8}$	582

117

In order to determine the real length of the still activated NEG vacuum beam pipes, VASCO simulations were also performed. These simulations were conducted by varying the saturated length of the CT2 chamber: the best fit between the experimental data and the distribution for N_2 equivalent is found for *1.5 m* saturated over *2.3 m* of its total length (Figure 80).

The pressure increase registered on the other side of the beam pipe is due to CH_4, which is not pumped by NEG.
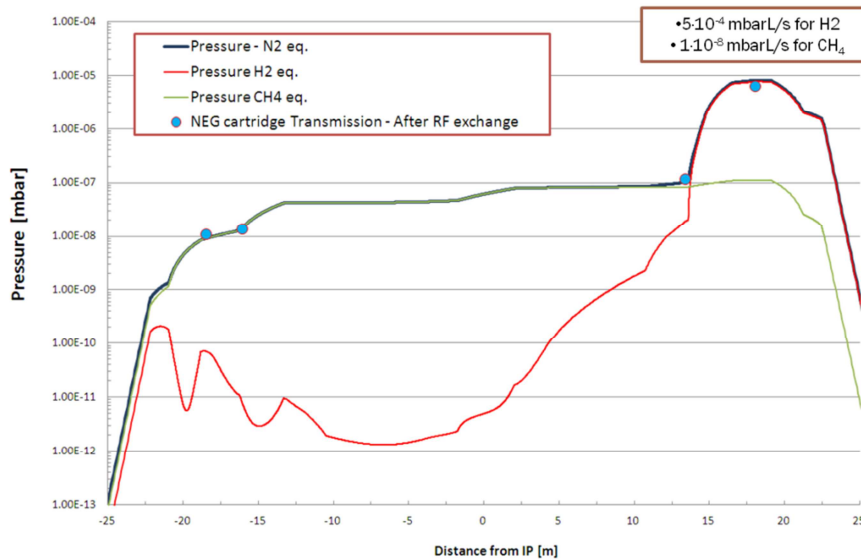
Figure 80 – VASCO simulation of the pressure profile along the CMS beam pipes during the H_2 transmission test after the RF insert exchange (*1.5 m* saturated).
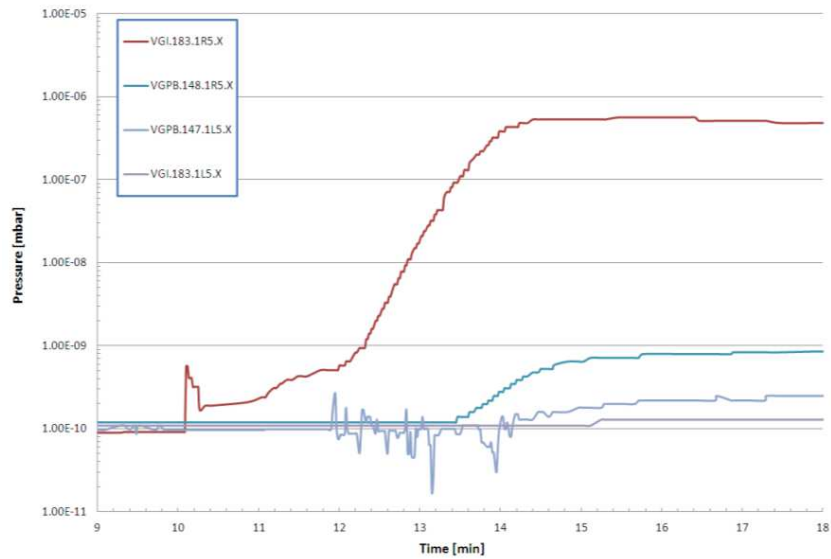
9.2.3   Transmission test after partial bakeout

As already mentioned, a partial bakeout was performed in order to reactivate the forward, TAS and CT2 NEG chambers and to bake the newly installed RF insert.

**Table 32 – Pressure and transmission ratio during the H_2 transmission test after the partial bakeout.**

Gauge position	Pressure [mbar]	Transmission ratio
18 m right side	$5.6 \cdot 10^{-7}$	1
13 m right side	$8.4 \cdot 10^{-10}$	667
13 m left side	$2.5 \cdot 10^{-10}$	2240
18 m left side	$1.3 \cdot 10^{-10}$	4308

After the bakeout, when all the vacuum chambers were again at room temperature, another H_2 transmission test was done. During this injection the TMP was turned off, while all the sputter-ion pumps were switched on.

Figure 81 – Pressure increase during the H_2 transmission test after the partial bakeout.

Figure 81 shows the pressure variation during the test: compared to the previous measurements conducted before the bakeout, the degassing of the heater inside the NEG cartridge is much lower and it can be detected only by the gauge located in the same vacuum dome.
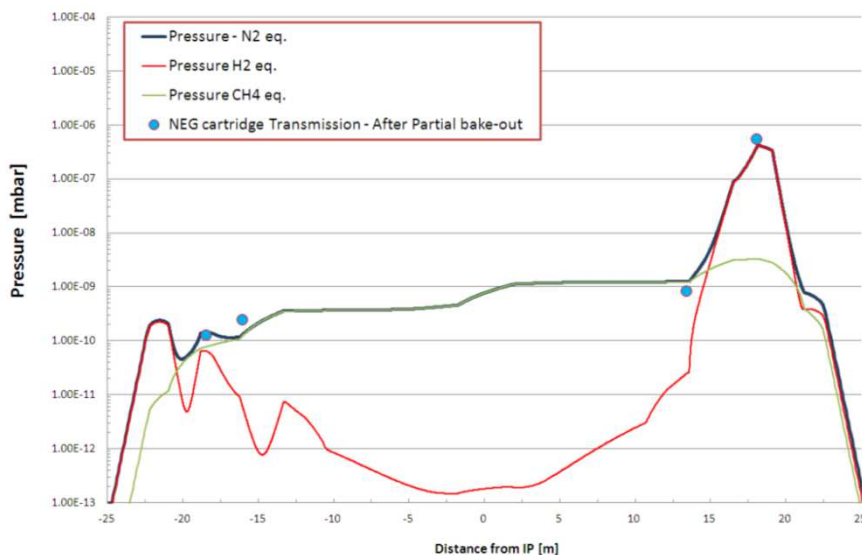
Figure 82 – VASCO simulation of the pressure profile along the CMS beam pipes during the H_2 transmission test after the partial bakeout.

119

Moreover, the transmission ratios are much higher than they were in the previous case, thus indicating that the bakeout fully reactivated the NEG vacuum chambers (Table 32).

VASCO simulations confirm the full activation of the NEG coating all along the CMS beam pipes and indicate that the recorded pressure increase is again due to CH_4 (Figure 82).

In summary, the use of H_2 transmission method allowed to estimate the full activation of the NEG coated beam pipes after the partial bakeout and to assess the quality of the entire procedure followed for the exchange of the non-conforming RF insert.

10. CONCLUSIONS

The extensive employment of NEG coated beam pipes in the room-temperature vacuum sectors of the LHC allows to keep and maintain the required UHV conditions during beam operation, providing a distributed pumping capacity for the residual gases along the length of these sectors.

However, this pumping capacity could be compromised by the progressive partial saturation of the NEG coated vacuum chambers, which is enhanced by dynamic effects of beam-stimulated desorption.

The saturation behaviour of two NEG coated vacuum systems has been studied at CERN in the framework of this thesis work, in order to identify and assess the best methods for the evaluation of the NEG saturation level in the LHC's sectors where this material is employed.

The first measurements were conducted in a *2 m* long NEG coated vacuum chamber and allowed to describe the variations of transmission, pumping and capture probabilities for H_2, N_2 and CO as functions of the progressively increasing NEG saturated length.

Other measurements were performed in a *28 m* long NEG coated pilot sector, reproducing the structure of a typical LHC's room-temperature vacuum sector.

These measurements confirmed the previously obtained results, highlighting however the strong influence that CH_4 degassing can have, especially on transmission, due to the fact that this gas is not pumped by NEG. All the future studies will have to take into account this phenomenon, which cannot be eliminated because all the inner walls of a vacuum system and all the devices for pressure measurements are potentially CH_4 sources.

The tests conducted pointed out that, among the possible methods for the estimation of NEG saturation in the LHC (degassing measurements, CO transmission, pumping speed evaluation), H_2 transmission must be preferred due to the sufficient precision of its results and to its feasibility in the LHC tunnel.

The H_2 transmission method was therefore applied to evaluate the NEG pumping properties in the LSS and in CMS interaction point, confirming the effectiveness of this solution and its reliability.

Moreover, the performed computer simulations identified MOLFLOW+, which is a Monte-Carlo based code, as an important tool for the prediction of pressure distribution and transmission variation in NEG coated vacuum systems as functions of the NEG saturated area. On the other hand, these simulations showed that, for very long NEG coated vacuum sectors, MOLFLOW+ simulations a long time to be completed, especially if the NEG coating is largely activated.

Finally, H_2 transmission results for long NEG coated vacuum sectors can be easily verified by simulations made with VASCO, a code based on multi-gas method which allows to estimate residual gas density profiles and to confirm the required vacuum stability conditions. In summary, the work performed will permit to evaluate the evolution of pressure inside the LSS NEG coated vacuum chambers and to estimate their saturated length, allowing to foreseen future interventions in the LHC.

ACKNOWLEDGEMENTS

BIBLIOGRAPHY

[1] «LHC Design Report - Vol. I: The LHC Main Ring,» CERN, 2004.

[2] G. Bregliozzi, V. Baglin, S. Blanchard, J. Hansen, J.M. Jimenez, K. Weiss, «Achievement and evaluation of the beam vacuum performance of the LHC Long Straight Sections,» in *proceedings of EPAC 2008*, Genoa (Italy).

[3] R. Calder, «Ion induced gas desorption problems in the ISR,» *Vacuum,* vol. 24, n. 10, pp. 437-443, 1974.

[4] "Vacuum Technology Know How", Pfeiffer Vacuum.

[5] D.J. Hucknall, A. Morris, "Vacuum technology - calculations in chemistry", Royal Society of Chemistry, 2003.

[6] J. Lafferty, "Foundations of vacuum science and technology", John Wiley & Sons, Inc., 1998.

[7] D. V. Ragone, "Termodinamica dei materiali", Casa Editrice Ambrosiana, 2003.

[8] P. Chiggiato, «Dégazage des solides en ultravide: quelques notions de base pour les techniciens du CERN,» 2012.

[9] K. Kanazawa, «Analysis of pumping down process,» *J. Vac. Sci. Technol. A,* n. 7 (6), 1989.

[10] G. Bregliozzi, G. Lanza, V. Baglin, J.M. Jimenez, «Vacuum stability and residual gas density estimation for the vacuum chamber upgrade of the ATLAS interaction region of the Large Hadron Collider,» *Vacuum,* vol. Article in press, 2012.

[11] V. Baglin, G. Bregliozzi, J.M. Jimenez, G. Lanza, «Synchrotron radiation in the LHC vacuum system,» in *Proceedings of IPAC 2011*, San Sebastian (Spain).

[12] G. Bregliozzi, V. Baglin, P. Chiggiato, P. Cruikshank, J.M. Jimenez, G. Lanza, «Observations of electron cloud effects with the LHC vacuum system,» in *Proceedings of IPAC 2011*, San Sebastian (Spain).

[13] C. Benvenuti, J.M. Cazeneuve, P. Chiggiato, F. Cicoira, A. Escudeiro Santana, V. Johanek, V. Ruzinov, J. Fraxedas, «A novel route to extreme vacua: the non-evaporable getter thin film coatings,» *Vacuum,* n. 53, pp. 219-225, 1999.

[14] C. Benvenuti, «Non-evaporable getters: from pumping strips to thin film coatings,» CERN.

[15] A. Rossi, «H2 equilibrium pressure with a NEG-coated vacuum chamber as a function of temperature and H2 concentration,» CERN.

[16] C. Benvenuti, F. Francia, «Room-temperature pumping characteristics of a Zr-Al nonevaporable getter for individual gases,» *J. Vac. Sci. Technol. A,* n. 6 (4), Jul/Aug 1988.

[17] C. Benvenuti, J-C. Decroux, «A linear pump for conductance limited vacuum systems,» in *Proceedings 7th Intern. Vac. Congr. & 3rd Intern. Conf. Solid Surfaces*, Vienna (Austria), 1977.

[18] A. Prodromides, "Non-Evaporable Getter Thin Film Coatings for Vacuum Applications", Lausanne: PhD thèse No. 2652, Faculté Sciences de Base, Section de Physique, EPFL, 2002.

[19] C.G. Smith, G. Lewin, «Free Molecular Conductance of a Cylindrical Tube with Wall Sorption,» *J. Vac. Sci. Technol. ,* vol. 3, n. 3, pp. 92-95, 1966.

[20] O.B. Malyshev, K.J. Middleman, «Test Particle Monte-Carlo modelling of installations for NEG film pumping properties evaluation,» *Vacuum,* n. 83, pp. 976-979, 2009.

[21] C. Benvenuti, A. Escudeiro Santana, V. Ruzinov, «Ultimate pressures achieved in TiZrV sputter-coated vacuum chambers,» *Vacuum,* n. 60, pp. 279-284, 2001.

[22] P. Chiggiato, P. Costa Pinto, «Ti-Zr-V non-evaporable getter films: From development to large scale production for the Large Hadron Collider,» *Thin Solids Films ,* n. 515, pp. 382-388, 2006.

[23] C. Benvenuti, P. Chiggiato, P. Costa Pinto, A. Escudeiro Santana, T. Hedley, A. Mongelluzzo, V. Ruzinov, I. Wevers, «Vacuum properties of TiZrV non-evaporable getter films,» *Vacuum,* n. 60, pp. 57-65, 2001.

[24] C. Benvenuti, P. Chiggiato, P. Costa Pinto, A. Prodromides, V. Ruzinov, «Influence of the substrate coating temperature on the vacuum properties of Ti-Zr-V non-evaporable getter films,» *Vacuum,* n. 71, pp. 307-315, 2003.

[25] Y. Yamamura, H. Tawara, «Energy dependence of io-induced sputtering yields from monoatomic solids at normal incidence,» *Atomic Data and Nuclear Data Tables,* n. 62, pp. 149-253, 1996.

[26] S. Amorosi, M. Anderle, C. Benvenuti, S. Calatroni, J. Carver, P. Chiggiato, H. Neupert, W. Vollenberg, «Study of the discharge gas trapping during thin-film growth,» *Vacuum,* n. 60, pp. 89-94, 2001.

[27] C. Benvenuti, P. Chiggiato, F. Cicoira, Y. L'Aminot, «Nonevaporable getter films for ultrahigh vacuum applications,» *J. Vac. Sci. Technol. A,* n. 16 (1), Jan/Feb 1998.

[28] C. Benvenuti, P. Chiggiato, F. Cicoira, Y. L'Aminot, V. Ruzinov, «Vacuum properties of palladium thin film coatings,» *Vacuum,* n. 73, pp. 139-144, 2004.

[29] R. Kersevan, J.-L. Pons, «Introduction to MOLFLOW+: New graphical processing unit-based Monte Carlo code for simulating molecular flows and for calculating angular coefficients in the compute unified device architecture environment,» *J. Vac. Sci. Technol. A,* n. 27 (4), Jul/Aug 2009.

[30] X. Tingwei, J.-M. Laurent, O. Groebner, «Monte Carlo simulation of the pressure and of the effective pumping speed in the Large Electron-Positron collider (LEP),» CERN, 1986.

[31] A. Rossi, «VASCO (VAcuum Stability COde): multi-gas code to calculate gas density profile in a UHV system,» CERN, 2004.

[32] G. Bregliozzi, «NEG qualification of CMS beam pipes after RF fingers insert exchange during winter technical stop 2011-2012 - EDMS document 1183364,» CERN, 2012.

[33] G. Bregliozzi, «Neon venting system for the LSS NEG vacuum beam pipes - EDMS document 1094561,» CERN, 2010.